CONFINEMENT-INDUCED DYNAMICS IN ULTRACOLD 2D FERMI GASES: EXPLORING POLARONS AND SPIN IMBALANCES

Dissertation
zur Erlangung des Doktorgrades
an der Fakultät für Mathematik, Informatik und Naturwissenschaften
Fachbereich Physik
der Universität Hamburg

vorgelegt von
René Henke

Hamburg, im Juni
2026

Gutachter der Dissertation	Prof. Dr. Henning Moritz
	Prof. Dr. Peter Schauß
Zusammensetzung der Prüfungskommission	Prof. Dr. Henning Moritz
	Prof. Dr. Peter Schauß
	Prof. Dr. Michael Potthoff
	Prof. Dr. Ludwig Mathey
	Prof. Dr. Roman Schnabel
Vorsitzender der Prüfungskommission	Prof. Dr. Michael Potthoff
Datum der Disputation	14.07.2026
Vorsitzender des Fach-Promotionsausschusses Physik	Prof. Dr. Johannes Haller
Leiter des Fachbereichs Physik	Prof. Dr. Markus Drescher
Dekan der Fakultät MIN	Prof. Dr.-Ing. Norbert Ritter

ABSTRACT

This thesis focuses on confinement-induced dynamics in 2D Fermi gases, how they modify the dynamics of the superfluid, and how they can be harnessed to probe many-body systems, namely Bose polarons and imbalanced Fermi gases. In the first part, I will show how the dynamics of the superfluid order parameter are altered by strong confinement. Using trap-modulation spectroscopy, we excite the amplitude mode of the superfluid order parameter, which hybridizes with a confinement-induced oscillation. This hybridization can be explored by tuning the energies of the involved modes via interactions and is described by a supporting effective field theory. Furthermore, I show that the confinement-induced mode disappears near the superfluid critical temperature, providing a probe of superfluidity.

In the second part, we create a repulsive Bose polaron in the strongly interacting regime by eliminating the dominating decay process usually present in polaronic quantum gas experiments. This is achieved by using bosonic dimers that are stable towards decay via Pauli blocking, since they are composed of fermions. The discrete energy levels of the confinement are then exploited as a synthetic spin, with the bath residing in the ground state. Transferring particles from the bath into higher levels then creates impurities. Using trap modulation and Bragg spectroscopy, we extract the energies, quasiparticle residue, and, for the first time, the effective mass of the Bose polaron. Our results are supported by a T-matrix theory and quantum Monte Carlo simulations.

In the last part, we will explore 2D spin-imbalanced Fermi gases. We achieve temperatures more than a factor of two lower than in previous experiments, up to polarizations of $P = 0.2$, and observe a homogeneous local polarization in the entire box trap for all probed polarizations and interactions. We find that the confinement-induced mode of the superfluid, as well as vortices, persist well into the strongly interacting regime, a strong indicator of superfluidity. Lastly, to connect our results to previous experiments conducted under harmonic confinement, we place an attractive potential at the center of the box trap and find the same ordering: a balanced core and an imbalanced region farther from the center. No jump in polarization is observed, allowing us to exclude the existence of a first-order phase transition for any system above $0.04\,T_{\mathrm{F}}$.

ZUSAMMENFASSUNG

Diese Arbeit konzentriert sich auf die Dynamiken, die aus starker Komprimierung von 2D-Fermigasen hervorgehen. Dabei wird untersucht, wie diese die Dynamik des Suprafluids beeinflussen und wie diese Anregungsmoden genutzt werden können, um Vielteilchensysteme zu untersuchen, allen voran Bose-Polaronen und imbalancierte Fermigase. Im ersten Teil werde ich zeigen, wie sich die Anregungsmoden des suprafluiden Ordnungsparameters durch Komprimierung verändern. Über Fallenmodulationsspektroskopie können wir die Amplitudenmode des Ordnungsparameters anregen, welche mit einer Schwingungsmode der Falle hybridisiert. Diese Hybridisierung kann durchgestimmt werden, indem die Energien der zwei Anregungsmoden über die Wechselwirkung verändert werden. Darüber hinaus zeige ich, dass die Schwingungsmode nahe der kritischen Temperatur des Superfluids verschwindet, was einen Indikator für Superfluidität liefert.

Im zweiten Teil erzeugen wir ein repulsives Bose-Polaron bei starker Wechselwirkung und eliminieren den dominanten Zerfallsprozess, der die Lebensdauer von Polaronen in Quantengasen normalerweise einschränkt. Wir erreichen dies, indem wir bosonische Feshbachmoleküle nutzen, die aus Fermionen bestehen und daher durch die Pauli-Blockade vor weiterem Zerfall geschützt sind. Die diskreten Energieniveaus aus der 2D-Falle werden dann als synthetischer Spin genutzt, indem das Bad im Grundzustand ist und Störstellen durch Anregen in höhere Zustände erzeugt werden. Über Fallenmodulations- und Braggspektroskopie charakterisieren wir das Polaron vollständig, indem wir Energie, Lebensdauer und effektive Masse messen. Unsere Beobachtungen werden von T-Matrix und quanten Monte Carlo Simulationen gestützt.

Im letzten Teil untersuchen wir spinimbalancierte 2D-Fermigase. Dabei erreichen wir Temperaturen, die mindestens einen Faktor zwei kälter sind als in vorherigen Experimenten, bei Polarisationen von bis zu $P = 0.2$. Wir beobachten eine homogene Polarisation im ganzen System bei allen untersuchten Polarisationen und Wechselwirkungen. Wir stellen fest, dass sowohl die durch die 2D-Falle hervorgerufene Schwingungsmode des Kondensats als auch Wirbel bis weit in den Bereich starker Wechselwirkungen hinein bestehen bleiben, was ein deutlicher Hinweis auf Suprafluidität ist. Um unsere Beobachtungen mit vorherigen Experimenten in harmonischen Fallen zu verbinden, platzieren wir ein attraktives Potenzial im Zentrum der Boxfalle. Wie in vorherigen Experimenten bilden sich ein balancierter Kern und eine imbalancierte Region weiter außen. Ein Sprung in der Polarisation bleibt aus, was uns einen Phasenübergang erster Ordnung für alle Systeme mit Temperaturen über $0.04\,T_\mathrm{F}$ ausschließen lässt.

CONTENTS

1 Introduction 7
2 Summary of the main results in this thesis 11
2.1 Hybridization of the amplitude mode in a confined fermionic superfluid 11
2.2 Stabilization of a repulsive Bose polaron 11
2.3 Imbalanced fermionic superfluids 12

I Background 15
3 Fermionic superfluids in reduced dimensions 17
3.1 Fundamental properties of Fermi gases 17
3.2 The BEC-BCS crossover 19
3.3 The superfluid order parameter: A top-down approach 23
3.4 Fermi gases in 2D 32
3.5 Experimental observation of collective modes 36
4 Experimental Apparatus 39
4.1 Overview of the experimental apparatus 39
4.2 Preparing an ultracold 2D Fermi gas 40
4.3 Probing 2D Fermi gases 44
4.4 Upgrades over the course of this work 49

II Dynamics under strong confinement 53
5 Hybridization of the amplitude mode in a confined fermionic superfluid 55
5.1 Engineering the hybridization in the BEC-BCS crossover 56
5.2 Theoretical model 58
5.3 Lifetime and free oscillations of the condensate 59
5.4 Breakdown of superfluidity at T_c 60

III Repulsive Bose polarons 63
6 Polarons 65
6.1 Bose polarons 66
6.2 Fermi polarons 68
7 The synthetic spin polaron 71
7.1 Polaron mapping 71
7.2 Extraction of the quasiparticle properties 73
7.3 Conclusion 79

IV Imbalanced Fermi gases 81
8 Imbalanced Fermi superfluids 83

8.1 Imbalanced Fermi gases in a nutshell 83
8.2 Exploring imbalanced Fermi mixtures with quantum gases 84
8.3 Phase diagram of 2D imbalanced Fermi gases 87
9 Realization of an imbalanced Fermi superfluid in a homogeneous 2D geometry 95
9.1 Creation of a cold imbalanced 2D Fermi gas 95
10 Probing 2D imbalanced superfluids 101
10.1 In situ density profiles 101
10.2 Observing superfluidity via order parameter dynamics 105
10.3 Observing persistent vortices 105
10.4 Interpretation of the results 107
10.5 Outlook 108

V Conclusion 111
11 Conclusion and outlook 113
A Double-shot imaging 117
B Meniscus cooling 119

BIBLIOGRAPHY 121

ACKNOWLEDGEMENTS 136

1 INTRODUCTION

Superconductivity is one of the most striking phenomena of quantum many-body physics. It was unintentionally observed for the first time in 1911, after cooling Mercury below 4.2 K, where the resistance dropped to zero. The phenomenon was only understood much later, in 1957, when Bardeen, Cooper, and Schrieffer published their celebrated BCS theory, explaining how the Cooper pairing mechanism leads to superconductivity at the microscopic level [1]. Before that, only phenomenological descriptions were possible within the framework of the Ginzburg-Landau theory, which treated the superfluid in terms of an order parameter ψ that becomes non-zero in the superconducting phase [2]. It correctly predicted the existence of two collective modes, in which the phase and amplitude of ψ oscillate, called the Goldstone and Higgs modes, respectively.

To this day, many surprising and novel phenomena continue to be discovered, extending beyond the initial description of conventional superconductivity. This includes the family of high-T_c superconductors, which are still not fully understood. Most of these are cuprates, where the electrons are confined to quasi-2D layers, which is surprising because here quantum fluctuations destroy true long-range order and one would naively expect superconductivity to be suppressed.

On the theoretical side, these quantum fluctuations make 2D systems hard to compute, a difficulty that worsens in the strongly interacting regime, since the fermions become highly correlated. Therefore, quantum simulations are urgently needed to address many of the outstanding questions. Ultracold atoms provide the perfect platform due to their high degree of control over interactions, temperatures, particle densities, and system geometry. Highlights in recent years have included the exploration of the BEC-BCS crossover [3], the observation of the Mott insulator [4], and the direct observation of Cooper pairs [5], just to name a few. Notable milestones in our group were the observation of superfluidity in 2D [6], the induction of Josephson oscillations between two reservoirs [7], and the measurement of the momentum-resolved spectrum via Bragg spectroscopy [8, 9], including the extraction of the superfluid gap in 2D and 3D. In the following, I will introduce the three main questions that are addressed in this thesis.

We start with a question relevant to any strongly confined system: What happens when the energy scales of the system become comparable to those of the confinement? Specifically, in Part II, we look at how the confinement modifies the dynamics of the superfluid by probing the interplay between two collective excitation modes: One, the amplitude mode, which is a coherent oscillation of the superfluid order parameter, manifesting as an oscillation of the condensate density; and

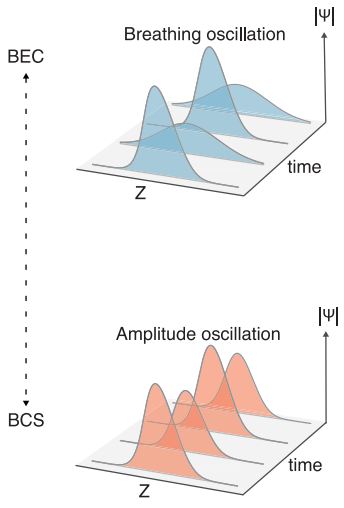


Figure 1.1: Dynamics of the superfluid order parameter in the BEC vs. the BCS limit of a strongly confined system. In the BEC limit, the superfluid oscillates spatially but the superfluid fraction stays constant, while in the BCS limit, the amplitude of ψ itself oscillates. Adapted from [10].

second, a confinement-induced mode where the condensate spatially oscillates in the trapping potential. We are able to tune the energies of both modes via interactions, which allowed us to observe hybridization in the region where the energies cross. More precisely, in the BCS limit, the amplitude of the order parameter oscillates, while far on the BEC side the condensate oscillates spatially (see Fig. 1.1). The connection between these two regimes is smooth, featuring a mixing between the modes. Additionally, since the confinement-induced mode is directly connected to the superfluid, we find that it disappears above T_c, making it an ideal probe for superfluidity.

With this tool in our hands, we can now tackle spin-imbalanced Fermi gases: Since fermionic superfluidity arises from pairing between particles, a central question is how it evolves in the presence of spin imbalance, where not all particles can pair. Early studies of superconductors have shown that, by creating a spin imbalance in the electrons via large magnetic fields, superconductivity breaks down as soon as the magnetic field is large enough to create a spin imbalance; the famous Chandrasekhar-Clogston limit [11, 12]. However, this is not the full picture, since electron superconductivity is suppressed by orbital motion induced by the strong magnetic fields. When this motion is eliminated, e.g., by using neutral atoms, a broad range of phenomena and exotic phases can occur. Previous studies in 3D systems have shown that these imbalanced systems tend to phase-separate into a superfluid, balanced domain and an imbalanced normal region [13]. Further experiments in 2D have made similar observations of the system ordering into balanced and imbalanced regions [14, 15]; however, contrary to theoretical predictions, no first-order phase transition was observed, and no clear signature of superfluidity has been detected. Additionally, although exotic phases are predicted to be more stable in lower dimensions, direct observation remains elusive to this day.

Therefore, in Part IV, we will explore the phase diagram of 2D imbalanced Fermi gases, far below the predicted critical temperature for superfluidity, which constitutes one of the two main results presented in this thesis. I will show how, for any probed polarizations up to $P = 0.2$, and any interactions, instead of domain formation, we observe a homogeneous local polarization. Additionally, we find strong indications of superfluidity, as we observe confinement-induced condensate oscillations via trap-modulation spectroscopy far into the strongly interacting regime, further supported by the presence of stable vortices. Since we did not observe any mode softening related to exotic phases in previous experiments on spin imbalances, our system is likely in a superfluid phase, where the excess majority lives as thermal excitations on top of the superfluid.

Lastly, we investigate the fundamental concept of an impurity immersed in a bath. Here, the impurity is dressed by the interactions with the bath, leading to a quasi-particle with its own energy and renormalized mass, called the *polaron*. Initially formulated to describe electrons moving in an ion lattice [16], polarons have been discovered

in a broad range of systems, including optically excited excitons in semiconductors or color centers in perovskites [17]. In recent years, ultracold-atom experiments have enabled the characterization of these systems, especially the Fermi polaron, in which the impurity is immersed in a degenerate Fermi gas. Bose polarons, however, are theoretically and experimentally much more challenging to explore due to the absence of Pauli blocking, which leads to larger coupling, richer physics (e.g., Efimov bound states), but also more severe decay processes in the strongly repulsive regime [18]. The latter is a fundamental issue arising from how repulsive interactions are engineered: They typically require an underlying bound state into which the impurity can decay, especially at strong interactions.

Therefore, in Part III, I will present the second main result of this thesis, in which we eliminated this loss channel by using a bath of repulsively interacting dimers. These dimers are composed of fermions and are thus protected via Pauli blocking from decay into larger bound states with more than two particles. By exploiting the discrete energy levels of strong confinement as a synthetic spin, we create impurities and extract key quantities well into the strongly interacting regime. Most notably, in addition to the polaron energy and quasiparticle residue, we extract the effective mass via Bragg spectroscopy for the first time in Bose polarons.

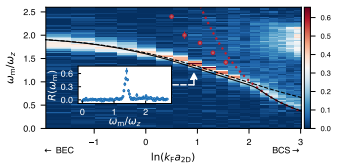
2 SUMMARY OF THE MAIN RESULTS IN THIS THESIS

2.1 Hybridization of the amplitude mode in a confined fermionic superfluid

Published in C. R. Cabrera, R. Henke, L. Broers, J. Skulte, H. P. Ojeda Collado, H. Biss, L. Mathey and H. Moritz, Physical Review Research **7** (3), L032018 (2025) [10]

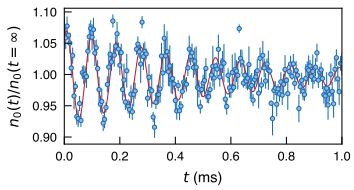
Observation of hybridization in the BEC-BCS crossover

The dominant experimental technique used in this thesis is trap-modulation spectroscopy, where the depth of a strongly confining potential is periodically modulated. For this publication, we used it to excite the amplitude mode of a fermionic superfluid and to observe how it hybridizes with a spatial oscillation of the condensate arising from strong confinement.



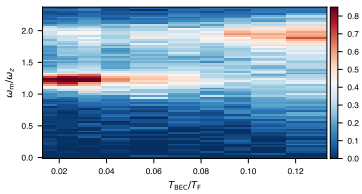
Free oscillations of the order parameter

We verify the oscillations of the superfluid via a second method: observing free oscillations in momentum space. After short driving and a variable evolution time, the oscillation becomes visible in the low-momentum peak of the condensate after a short time of flight. The energies and large lifetimes are compatible with those extracted from the trap modulation spectrum.



Vanishing of the mode at the critical temperature

Finally, since the observed dynamics are directly related to the superfluid order parameter, we measure its behavior for different temperatures. As expected, increasing the temperature broadens the mode and reduces its spectral weight, until it vanishes at a critical temperature consistent with previous experiments on 2D Fermi gases.

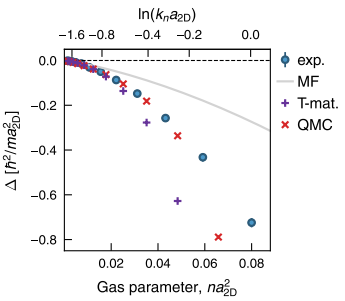


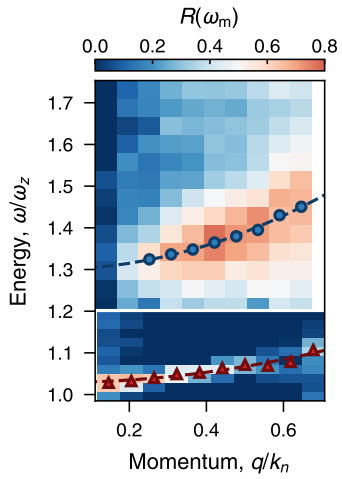
2.2 Stabilization of a repulsive Bose polaron

Preprint in R. Henke, C. R. Cabrera, J. Levinsen, M. M. Parish, G. E. Astrakharchik, J. Boronat and H. Moritz, arXiv:2511.03569v1 (2025) [19]

Engineering a Bose polaron from strong confinement

We implement a repulsive Bose polaron by using a condensate of bosonic dimers forming a bath in the ground state of a strongly confining potential. A polaron can be created by populating higher harmonic oscillator states. Since the underlying atoms are fermionic, the typical decay path into energetically favorable bound states is





effectively eliminated, while the repulsive interactions between the dimers are retained. The mapping to the polaron picture is further supported by T-matrix and diffusion Monte Carlo calculations.

Quasi-particle properties from zero momentum spectra

We extract three quasi-particle properties via trap modulation spectroscopy, namely the polaron energy, lifetime, and quasiparticle residue. We are able to, for the first time, access the strongly repulsive regime because the typical decay channel for repulsive Bose polarons is eliminated in our system.

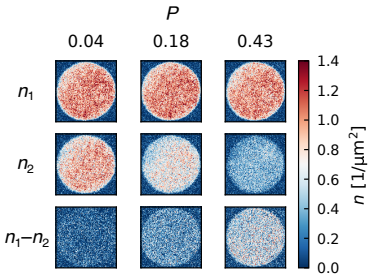
Measuring the effective mass

Another main achievement in this work is the measurement of the effective mass. Bragg spectroscopy provides access to the momentum-resolved spectrum and, therefore, to the effective mass m^*. We show that the extracted m^* increases as it enters the strongly repulsive regime, exceeding twice the dimer mass.

2.3 Imbalanced fermionic superfluids

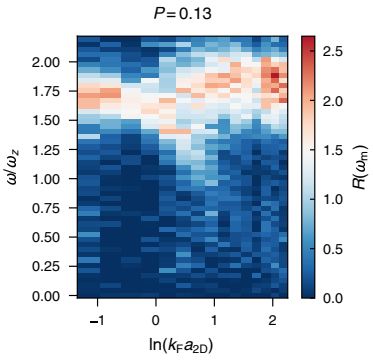
Creating an imbalanced 2D superfluid

We create an imbalanced 2D Fermi gas, for the first time, at temperatures far below the superfluid critical temperature T_c. We achieve this by starting with a cold, balanced system of ^{6}Li in the lowest two hyperfine states $|1\rangle$ and $|2\rangle$, transferring a desired fraction from $|2\rangle$ to $|3\rangle$, and performing a blowout of $|3\rangle$. After reevaporation we reliably reach imbalances up to $P = 0.2$ colder than 6 % of the Fermi temperature.



Absence of phase separation in homogeneous geometries

In a homogeneous system, we do not observe any phase separation, even below the superfluid critical temperature and imbalances of up to $P = 20$ %. When a harmonic potential is introduced at the center, the system gradually separates into a balanced core and an imbalanced region on the outside, replicating previous experimental observations.



Probing order parameter dynamics

We verify superfluidity in our system by probing the order-parameter dynamics via trap-modulation spectroscopy. For an imbalance of $P = 13$ %, we observe a condensate mode well into the strongly interacting regime. Further on the BCS side, it vanishes, signaling the breakdown of superfluidity. This is further supported by the observation of stable vortices in the same interaction range. For comparison, we probe a balanced system at the same temperature and find a mode that

persists throughout the entire BEC-BCS crossover, confirming that the breakdown in the $P = 13\,\%$ system stems solely from the imbalance.

Part I

Background

3 FERMIONIC SUPERFLUIDS IN REDUCED DIMENSIONS

3.1 Fundamental properties of Fermi gases

One of the biggest breakthroughs in physics in the past century was the discovery and subsequent theoretical description of superconductivity and superfluidity. The normal-to-superfluid phase transition was first described using the phenomenological London and Ginzburg-Landau equations and manifests as a breaking of the $U(1)$ symmetry. The resulting nonzero superfluid order parameter gives rise to the well-known sound (Goldstone) and amplitude (Higgs) modes. Subsequently, Cooper recognized that fermions can pair up in order to enter a superfluid state, leading to the microscopic description of superfluidity in the celebrated BCS theory [1], formulated by Bardeen, Cooper, and Schrieffer.

This chapter provides a short introduction to these fundamental concepts. After introducing the general concept of Bose-Einstein condensation (BEC) and fermionic superfluidity in Ch. 3.1.1, we will take a closer look at BCS theory and how it smoothly connects the BEC regime (pairing in real space) with the BCS regime (pairing in momentum space).

I then focus on two fundamental collective modes: the phase (Goldstone) and amplitude (Higgs) modes by first approaching them in the framework of Ginzburg-Landau theory in Ch. 3.3. This phenomenological theory is very useful for intuitively describing the superfluid-to-normal phase transition by introducing a superfluid order parameter that is directly connected to the condensate density. Extending this theory to time-dependent solutions allows us to extract typical excitation spectra that contain both collective modes. Depending on the time-dependent terms, these modes are either separate or coupled.

In Ch. 3.3.4, we will finally connect Ginzburg-Landau to BCS theory. After extending the latter to the Bogoliubov-de Gennes equations to include gradients and temporal dynamics, we will see that for attractive interactions (BCS regime), the phase and amplitude modes decouple due to particle-hole symmetry. In contrast, for repulsive interactions (BEC regime), this symmetry is suppressed and the modes couple, leading to the famous Bogoliubov dispersion.

Last, in Ch. 3.4, we will consider superfluidity in a 2D geometry by first looking at how the defining quantities (e.g. the scattering length, binding energy, gap, etc.) change in comparison to 3D and then introduce a new, confinement-induced collective mode of the order parameter that will be important for the three main results presented within this thesis.

3.1.1 Fermionic condensation in a nutshell

It is well known that when bosons are cooled to low temperatures, they begin to occupy the same state, leading to the formation of a macroscopic wave function. This phenomenon is called Bose-Einstein condensation (BEC) and was predicted by Bose and Einstein in 1924 and first observed in Rubidium by Cornell and Wieman [20], as well as in Sodium by Ketterle in 1995 [21]. For condensation to occur, the number of energetically accessible states of a system needs to be smaller than the number of particles. This happens when the thermal de Broglie wavelength $\lambda_T = \sqrt{\frac{2\pi\hbar^2}{mk_BT}}$ is comparable to the interparticle spacing. Here m is the mass of a Boson, T the temperature, and k_B the Boltzmann constant. This criterion is captured well by the phase-space density $\mathcal{D} = n\lambda_T^3$, where n is the boson density. For a weakly interacting Bose gas in 3D, the critical phase-space density above which condensation occurs is $\mathcal{D}_c = \zeta(3/2) \approx 2.612$ (derivation in standard textbooks, e.g. [22]), with the Riemann-Zeta function ζ. To illustrate its validity, plugging in typical values for ^{4}He ($m_{^4\mathrm{He}} = 6.65 \times 10^{-27}$ kg, $n \approx 2.2 \times 10^{28}$ atoms/m^3) leads to a critical temperature $T_c \approx 3.1$ K below which condensation occurs[1], which is close to the experimentally observed critical temperature $T_c = 2.2$ K.

Of course, the examples from above are all bosonic systems. Fundamentally, condensation is only possible for bosons, since they are allowed to occupy the same state, which, due to Pauli blocking, is not possible for fermions. However, this limitation can be circumvented by adding a second fermion species (e.g., in different spin or hyperfine states). Interactions then allow the formation of pairs with integer spin, causing them to behave like bosons. Naturally, pairing requires a bound state, which is governed by the interactions. For attractive interactions, the existence of such a bound state actually depends on the dimensionality. While a two-body bound state always exists for arbitrarily weak attractive interactions in 1D and 2D, the 3D case requires a critical potential depth [23]. However, in a many-body system, this criterion for 3D systems is overcome due to the change in geometry when a Fermi sea is present: Scattering can only occur on the Fermi surface, which is two-dimensional. This effectively reduces the problem back to 2D, and pairs can form again for arbitrarily weak interactions.

These pairs always form at opposite momenta, which happens due to Pauli blocking, as illustrated in Fig. 3.1: Because of energy conservation, only fermions close to the Fermi surface are allowed to scatter, since the states below k_F are fully occupied, while they are empty above. Additionally, under momentum conservation, the number of states into which two fermions can scatter is maximal when the pair has total momentum $q_\mathrm{tot} = 0$. The reason for this is that the conserved quantity q_tot remains zero, no matter where the fermions are located on the Fermi surface, as long as they carry opposite momenta. In contrast, at $q \neq 0$, only two points on the Fermi surface are accessible, suppressing interactions.

[1] Technically, liquid ^{4}He is not in the weakly interacting limit, but in this case the criterion still works surprisingly well and is therefore included for illustration purposes.

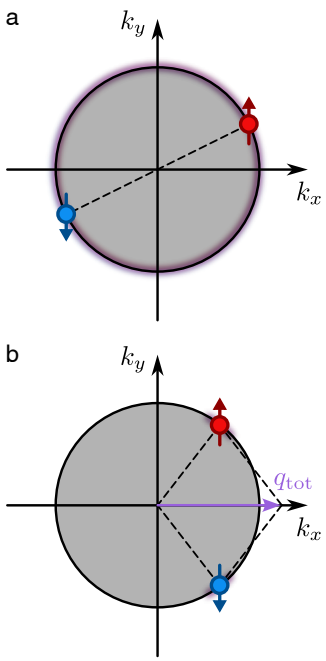


Figure 3.1: Visualization of Cooper pairing. a) Particles at opposite momenta and spins can scatter freely anywhere on the Fermi surface as long as the total pair momentum q_tot remains zero (purple shaded region). No energy transfer can occur in this process because all states below the Fermi surface are fully occupied (gray area). b) Pairing is heavily suppressed when the pair momentum is non-zero. Because q_tot needs to be preserved, the particles only have a small region on the Fermi surface that they are allowed to scatter into.

In the scenario of repulsive interactions, on the other hand, the picture is very different. When interactions are purely repulsive, no bound state exists, and the particles will be pushed apart. A good example of this is two free electrons repelling each other via the Coulomb interaction. In practice, however, repulsive interactions can be engineered from an underlying bound state. Most prominently, neutral-atom experiments use Feshbach resonances to achieve tunable interactions, where a molecular bound state is tuned close to the energy of the unpaired atoms. At repulsive interactions, this molecular state is energetically favorable, resulting in the famous BEC-BCS crossover that smoothly connects pairing in momentum space (BCS state) at attractive interactions to deeply bound molecules (BEC) at repulsive interactions. Of special interest is the *universal* regime, where the scattering length diverges, resulting in a system that is defined only by the Fermi energy E_F.

3.2 The BEC-BCS crossover

As we just discussed, fermions can pair, which allows for condensation. The microscopic theory describing this phenomenon was formulated by Bardeen, Cooper, and Schrieffer in 1957 [1], and will be briefly discussed in the following. Our goal is to find two things: the ground state of this interacting system and its excitation spectrum. In the following, we will follow the derivation given in [23].

We start from the Hamiltonian describing an interacting Fermi gas with two spin states $\sigma = \{\uparrow, \downarrow\}$ in second quantization

$$H = \sum_{\mathbf{k},\sigma} \epsilon_\mathbf{k} c^\dagger_{\mathbf{k}\sigma} c_{\mathbf{k}\sigma} + \frac{g}{V} \sum_{\mathbf{k},\mathbf{k}',\mathbf{q}} c^\dagger_{\mathbf{k}+\mathbf{q},\uparrow} c^\dagger_{\mathbf{k}'-\mathbf{q},\downarrow} c_{\mathbf{k}'\downarrow} c_{\mathbf{k}\uparrow} , \tag{3.1}$$

with the creation and annihilation operators $c^\dagger_{\mathbf{k}\sigma}$ and $c_{\mathbf{k}\sigma}$ at a momentum $\mathbf{k}$. Here, $\epsilon_\mathbf{k} = \hbar^2 k^2/2m$ is the kinetic energy, V the volume and g the (s-wave) contact coupling constant. Since we know that the fermions in our system pair at opposite momenta, we only consider scattering from $|k' \uparrow, -k' \downarrow\rangle$ to $|k \uparrow, -k \downarrow\rangle$ (restricting $\mathbf{q} = \mathbf{k} - \mathbf{k}'$), which simplifies the Hamiltonian to

$$H = \sum_{\mathbf{k},\sigma} \epsilon_\mathbf{k} c^\dagger_{\mathbf{k}\sigma} c_{\mathbf{k}\sigma} + \frac{g}{V} \sum_{\mathbf{k},\mathbf{k}'} c^\dagger_{\mathbf{k},\uparrow} c^\dagger_{-\mathbf{k},\downarrow} c_{-\mathbf{k}'\downarrow} c_{\mathbf{k}'\uparrow} . \tag{3.2}$$

The interaction term here still remains complicated, so it is useful to perform a mean-field approximation by using the relation

$$\hat{A}\hat{B} \approx \langle \hat{A} \rangle \hat{B} + \hat{A} \langle \hat{B} \rangle - \langle \hat{A} \rangle \langle \hat{B} \rangle , \tag{3.3}$$

with $\hat{A} = c^\dagger_{\mathbf{k},\uparrow} c^\dagger_{-\mathbf{k},\downarrow}$ and $\hat{B} = c_{-\mathbf{k}'\downarrow} c_{\mathbf{k}'\uparrow}$. By introducing

$$\Delta = -\frac{g}{V} \sum_k \left\langle c_{\mathbf{k},\uparrow} c_{-\mathbf{k},\downarrow} \right\rangle , \tag{3.4}$$

we get the mean-field Hamiltonian

$$H_\mathrm{MF} = \sum_{\mathbf{k},\sigma} \epsilon_\mathbf{k} c^\dagger_{\mathbf{k}\sigma} c_{\mathbf{k}\sigma} + \sum_\mathbf{k} \left(\Delta c^\dagger_{\mathbf{k},\uparrow} c^\dagger_{-\mathbf{k},\downarrow} + \Delta^* c_{-\mathbf{k}\downarrow} c_{\mathbf{k}\uparrow} \right) + \frac{V}{g} |\Delta|^2 . \tag{3.5}$$

The last term is constant and is therefore disregarded from here on out.

Next, we introduce the BCS ansatz, which is best suited to the problem, since it expresses the ground state as a superposition between holes and pairs of opposite momenta

$$|\text{BCS}\rangle = \prod_k \left(u_k + v_k c^\dagger_{k\uparrow} c^\dagger_{-k\downarrow}\right)|0\rangle \ . \tag{3.6}$$

Here, u_k and v_k determine the occupation of holes and pairs, respectively, and are normalized to

$$|u_k|^2 + |v_k|^2 = 1 \, . \tag{3.7}$$

We chose u_k and v_k to be real, leading to

$$\Delta = -\frac{g}{V}\sum_k u_k v_k \tag{3.8}$$

also being real. The ground state is then found by minimizing the free energy

$$\mathcal{F} = \langle H - \mu N\rangle = \sum_k 2\xi_k v_k^2 + 2\Delta \sum_k u_k v_k \tag{3.9}$$

with the chemical potential μ and $\xi_k = \epsilon_k - \mu$. We additionally need to take into account the constraint 3.7 from the normalization of u_k and v_k. It is therefore convenient to describe the problem in the Lagrangian formalism and introduce the constraint as the Lagrange multiplier E_k, leading to the Lagrangian

$$\mathcal{L} = \mathcal{F} - E_k(u_k^2 + v_k^2 - 1) \, . \tag{3.10}$$

We can then minimize $\mathcal{L}$ by expressing the system as

$$\begin{pmatrix} \frac{\partial \mathcal{L}}{\partial u_k} \\ \frac{\partial \mathcal{L}}{\partial v_k} \end{pmatrix} = 2 \begin{pmatrix} \xi_k - E_k & \Delta \\ \Delta & -\xi_k - E_k \end{pmatrix} \begin{pmatrix} u_k \\ v_k \end{pmatrix} \stackrel{!}{=} 0 \, . \tag{3.11}$$

We can disregard the prefactor and solve the eigenvalue problem to arrive at

$$v_k = \sqrt{\frac{1}{2}\left(1 - \frac{\xi_k}{E_k}\right)} \tag{3.12}$$

$$u_k = \sqrt{\frac{1}{2}\left(1 + \frac{\xi_k}{E_k}\right)} \tag{3.13}$$

$$E_k = \sqrt{\xi_k^2 + \Delta^2} \, . \tag{3.14}$$

At this point, Δ and μ are still unknown, but we can find two equations that allow us to fix them for arbitrary interactions. The first is the *gap equation* and is obtained by inserting the solutions for u_k and v_k back into 3.8

$$\Delta = -\frac{g}{V}\sum_k \sqrt{\frac{1}{4}\left(1 - \frac{\xi_k^2}{E_k^2}\right)} = -\frac{g}{V}\sum_k \sqrt{\frac{\Delta^2}{4E_k^2}} \tag{3.15}$$

$$\Rightarrow -\frac{V}{g} = \sum_k \frac{1}{2E_k} \, . \tag{3.16}$$

The second is the *number equation* and is obtained using the fact that v_k is related to the number of pairs, and therefore the density, leading to

$$n = \sum_{k,\sigma} v_k^2 = \sum_k 2v_k^2 = \sum_k \left(1 - \frac{\xi_k}{E_k}\right) . \tag{3.17}$$

Solving these two equations simultaneously gives us μ and Δ, and therefore a ground state $|\mathrm{BCS}\rangle$. An analytical solution was found by Marini et al. [24] using elliptic integrals, which is plotted in 3.2. We can see a smooth transition between the BEC and BCS regimes. In the former, the chemical potential is negative and dominated by the binding energy $E_B = \hbar^2/(ma^2)$, since the fermions are tightly bound in composite bosons. In the BCS regime, on the other hand, we see that the positive chemical potential approaches E_F and Δ vanishes. This makes sense, since for $1/k_\mathrm{F}a \to -\infty$, the system becomes a non-interacting Fermi gas.

With μ and Δ defined, we can now go back and calculate the momentum distributions u_k^2 and v_k^2, which are plotted in Fig. 3.3 for a broad range of interactions $1/k_\mathrm{F}a$. As noted before, deep in the BCS regime, we recover the ideal Fermi gas: The chemical potential takes the value of E_F while Δ vanishes. This leads to a sharp Fermi distribution, where all states below k_F are fully occupied.

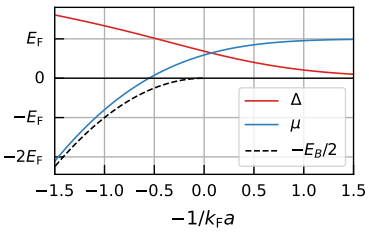


Figure 3.2: The gap Δ and chemical potential μ in the BEC-BCS crossover. On the BEC side, the chemical potential takes the value of half the binding energy E_B, while it goes towards E_F on the BCS side. At the same time, Δ vanishes on the BCS side, signaling the transition to an ideal Fermi gas.

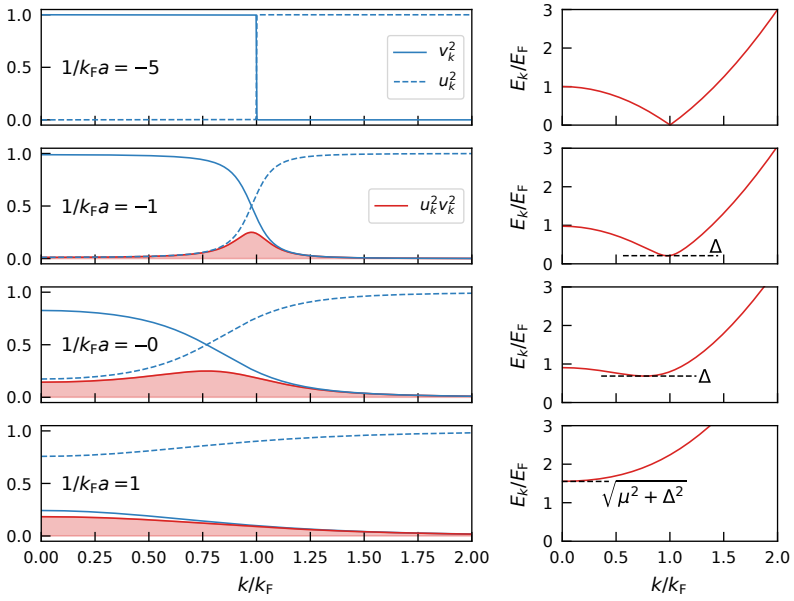


Figure 3.3: Left: Occupation of particles v_k^2 and holes u_k^2 for different interaction parameters $1/k_\mathrm{F}a$. On the BCS side ($1/k_\mathrm{F}a \ll 0$), v_k^2 approaches the distribution of a degenerate Fermi gas, with a sharp drop in population at k_F and no condensed pairs $u_k^2 v_k^2$. For increasing interactions, the Fermi surface washes out and pairing happens around k_F, while on the BEC side ($1/k_\mathrm{F}a \gg 0$) the distribution of the condensed pairs approaches v_k^2. Right: Single-particle excitation energies for the same interactions. Far in the BCS regime, there is no excitation gap, and the dispersion is that of a non-interacting Fermi gas. For finite attractive interactions, the spectrum becomes gapped with an energy of Δ at finite momenta, while on the BEC side, this energy minimum becomes $\sqrt{\mu^2 + \Delta^2}$ at $k = 0$.

Switching on attractive interactions, the sharp edge at k_F softens, since the energy gained by forming pairs becomes larger than the extra kinetic energy required to populate higher momentum states. The momentum distribution of pairs is given by $u_k^2 v_k^2$, which is largest at k_F. As we move towards positive $1/k_\mathrm{F}a$, the Fermi surface softens further until $u_k^2 v_k^2$ approaches the Boltzmann distribution, signaling the BEC regime. Here, pairing does not take place in momentum but

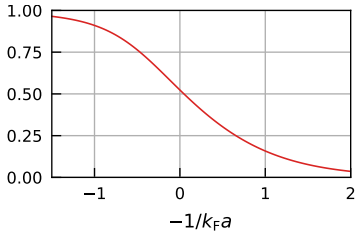


Figure 3.4: Condensate fraction in the BEC-BCS crossover. Towards the non-interacting BEC regime the fraction tends towards 1, while in the BCS regime, it approaches 0.

in real space, since all fermions are tightly bound, with pair sizes much smaller than the inter-particle distance.

If we integrate the distribution of pairs $u_k^2 v_k^2$ and all particles v_k^2, we can determine the condensate fraction, which is shown in Fig. 3.4 for the full crossover. We can see how the fraction approaches zero in the BCS regime, again signaling the transition to an ideal Fermi gas. On the BEC side, the entire system condenses, as the fermions are tightly bound in composite bosons.

Additionally, we can determine the single-particle excitation by considering the change in free energy upon adding or removing a particle at a specific momentum k. Since a single particle does not have the ability to pair, its energy is only given by ξ_k. Additionally, the momentum state the particle is added to or removed from becomes unavailable for the rest of the condensate, costing an extra energy of $\mathcal{F}_k$. Together, the excitation energy is

$$\Delta\mathcal{F}_k = \xi_k - \mathcal{F}_k\,, \tag{3.18}$$

with

$$\mathcal{F}_k = 2\xi_k v_k^2 + 2u_k v_k \overbrace{\frac{g}{V}\sum_{k'} u_{k'} v_{k'}}^{-\Delta} \tag{3.19}$$

$$= \xi_k \left(1 - \frac{\xi_k}{E_k}\right) - \Delta\frac{\sqrt{E_k^2 - \xi_k^2}}{E_k} \tag{3.20}$$

$$= \xi_k - \frac{\xi_k^2}{E_k} - \frac{E_k^2 - \xi_k^2}{E_k} \tag{3.21}$$

$$= \xi_k - E_k\,. \tag{3.22}$$

Therefore, the single-particle excitation energy is

$$\Delta\mathcal{F}_k = \xi_k - \xi_k + E_k = E_k\,. \tag{3.23}$$

which, in the BCS regime ($\mu > 0$) has a minimum at $\xi_k = 0$ ($\epsilon_k = \mu$), taking the value of Δ. This is why Δ is also called the gap. For $\mu < 0$, the minimum is instead at $k = 0$, with a value of $\sqrt{\mu^2 + \Delta^2}$ (see Fig. 3.3).

In many experiments, including those presented in this thesis, the particle number is conserved. To account for this, we can instead take a particle at k and place it at k' with an energy cost of $E_k + E_{k'}$. The energy gap in this scenario is calculated by exciting the particle into the orthogonal state, resulting in an energy cost of $2E_k$, which is 2Δ and $2\sqrt{\mu^2 + \Delta^2}$ in the BCS and BEC regimes, respectively.

Apart from single-particle excitations, collective excitations also exist in superfluids. In the following chapters, we will focus on the two relevant collective modes for this thesis: the Bogoliubov (sound) mode and the amplitude mode, in which the condensate fraction itself oscillates. These modes appear as a result of the broken $U(1)$ symmetry in a superfluid. To describe these excitations, BCS theory must be

extended to include spatial dependence, leading to the Bogoliubov-de Gennes equations. However, to gain an intuitive understanding of these modes, we will first examine the phenomenological Ginzburg-Landau theory in the following chapter, which introduces the concept of an order parameter and explains how the collective modes arise from the spontaneous symmetry breaking at the phase transition. Afterward, we learn how Ginzburg-Landau theory connects to Bogoliubov-de Gennes equations.

3.3 The superfluid order parameter: A top-down approach

In the previous chapter, we discussed BCS theory, which uses a "bottom-up" approach: Starting from individual particles, we move up to arrive at many-body phenomena. By contrast, one can instead start from the top and examine condensation within the framework of Ginzburg-Landau theory, a phenomenological approach that is particularly well suited to intuitively describe the physics of phase transitions and is valid near T_c. Historically, this theory was used to describe the superfluid-to-normal phase transition, before BCS theory was formulated.

The central concepts are introduced in the framework of the non-local and therefore simpler Landau theory in Ch. 3.3.1, before moving on to the full Ginzburg-Landau picture with a local order parameter that can change spatially in Ch. 3.3.2. In Ch. 3.3.3, we will then see how the amplitude and Goldstone modes naturally emerge from this theory, and justify the picture by connecting it to BCS theory in Ch. 3.3.4.

3.3.1 Spatially uniform scenarios: Landau theory

The central concept in (Ginzburg-)Landau theory is the order parameter ψ, which characterizes the state of a system and changes from zero to a finite value at a phase transition. The ground state for ψ is determined by minimizing the free energy[2] $F(\psi, T)$.

Often, an exact expression of F is not known, and it is useful to write it as an expansion for ψ, only including terms that are allowed by the symmetries of the system. In the case of a superfluid, it is natural to define ψ as the complex amplitude of the single-particle wave function $\Psi(\mathbf{r})$, which is normalized to the total number of particles in the condensate

$$\int |\Psi(\mathbf{r})| d^3r = N\,. \tag{3.24}$$

So, $|\psi|$ directly corresponds to the superfluid density, which in BCS theory is given by the integral over $u_k^2 v_k^2$.

To describe our system, we choose a free energy featuring terms up to the fourth order

$$F = \alpha|\psi|^2 + \frac{\beta}{2}|\psi|^4\,, \tag{3.25}$$

[2] Here we consider the free energy because it is the relevant quantity for the systems discussed in this thesis. Though, depending on the context, other quantities can be minimized to find ψ, e.g., the enthalpy.

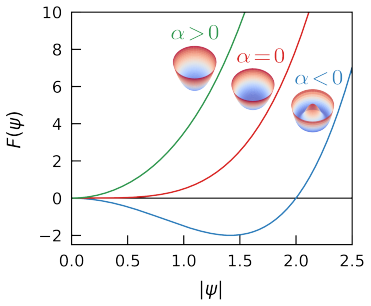


Figure 3.5: Free energy vs. $|\psi|$ for different values of α and positive β. As long as $\alpha > 0$, the minimum of $F(\psi)$ is at $|\psi| = 0$, while at $\alpha < 0$ it is located at $|\psi| = \sqrt{-\alpha/\beta}$, entering the new phase. The phase transition happens at $\alpha = 0$. 3D plots show the full landscape of $F(\psi)$ for the complex valued ψ at each plotted value α.

introducing the coefficients α and β, that, in general depend on T. We do not include any odd-order terms, because the physics are not allowed to change under phase rotations $\psi \to e^{i\phi}\psi$. For physical solutions, we can see that $\beta > 0$, since otherwise $|\psi|$ would diverge. Additionally, we can see that a phase transition takes place at $\alpha = 0$, when considering the minima of F (see Fig. 3.5): For $\alpha > 0$, the minimum is at $|\psi| = 0$, which marks the normal state, as no particles are present in the condensate wavefunction. In contrast, at $\alpha < 0$, there is a minimum located at $|\psi| = \sqrt{-\alpha/\beta}$. It follows that the temperature at which $\alpha = 0$ must be $T = T_c$. Additionally, we can see that the phase transition constitutes a break in the $U(1)$ symmetry of the normal state, since $\psi = |\psi|e^{i\phi}$ is complex-valued. In the normal phase where $|\psi| = 0$, the system is invariant under phase rotations ($U(1)$ symmetry), but once $|\psi| > 0$, it spontaneously settles on a fixed phase since the minimum of F now corresponds to a ring in the complex plane.

Let us now examine the behavior of the condensate near T_c. Expanding α to first order around $T = T_c$ and considering that it has to vanish at T_c gives $\alpha \approx \alpha'(T - T_c)$, with $\alpha' > 0$. For simplicity, we set $\beta = \text{const.}$, since the crucial feature of the phase transition is the sign change of α at T_c, yielding[3]:

$$|\psi| = \begin{cases} \sqrt{\frac{\alpha'}{\beta}}\sqrt{T_c - T}, & T \leq T_c \\ 0, & T > T_c \end{cases} \tag{3.26}$$

[3] Here, we only use our knowledge that at $T > T_c$ the order parameter is $|\psi| = 0$, while below T_c we plug the linear expansion of α into $|\psi| = \sqrt{-\alpha/\beta}$.

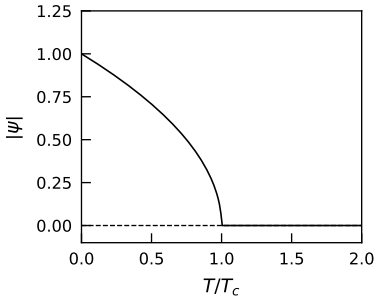


Figure 3.6: Behavior of the order parameter four our first-order expansion of α around the critical temperature T_c, given by Eq. (3.26).

which is plotted in Fig. 3.6. Additionally, we can show that the phase transition is of second order. Under Ehrenfest's classification, the order of a phase transition equals the lowest derivative of the relevant thermodynamic potential that is discontinuous at the critical point. In our case, this potential is the free energy F. For $T > T_c$, all derivatives are zero (since $F(|\psi| = 0) = 0$), while for $T < T_c$ we get

$$\frac{\partial}{\partial T} F\left(\sqrt{-\frac{\alpha(T)}{\beta}}\right) = -S = \frac{(\alpha')^2}{\beta}(T_c - T) \tag{3.27}$$

$$\frac{\partial^2}{\partial T^2} F\left(\sqrt{-\frac{\alpha(T)}{\beta}}\right) = -\frac{C}{T} = -\frac{(\alpha')^2}{\beta}\,. \tag{3.28}$$

The first derivative, which is related to the entropy S, vanishes at $T = T_c$ and therefore continuously connects to $F = 0$ at $T > T_c$, meaning it is not a first-order transition. The second derivative, which is related to the heat capacity C, instead exhibits a jump at $T = T_c$ from $-(\alpha')^2/\beta$ to 0, making it a second-order phase transition[4].

[4] If we want to describe a first-order phase transition instead, we need to include a $|\psi|^6$ term.

3.3.2 Spatially non-uniform scenarios: Ginzburg-Landau theory

Now we extend our model to feature a local order parameter, turning it into a field:

$$\psi \to \psi(\mathbf{r})\,, \tag{3.29}$$

This allows us to describe spatially inhomogeneous scenarios. The free energy from Eq.(3.25) now becomes an integral over the volume of the system and gains a term for the kinetic energy ($\gamma|\nabla\psi|$), leading to the famous Ginzburg-Landau functional:

$$F[\psi] = \int d^3r \left[\alpha|\psi|^2 + \frac{\beta}{2}|\psi|^4 + \gamma\,|\nabla\psi|^2\right] \tag{3.30}$$

Following the extremal principle, to find the differential equations describing ψ, we are looking for a solution where the functional derivative

$$\frac{\delta F}{\delta\psi} = 0\,. \tag{3.31}$$

The functional derivative is defined as the function that fulfills

$$\begin{aligned}\int \frac{\delta F}{\delta\psi}(\mathbf{r})\,\eta(\mathbf{r})\,d^3r &= \lim_{\varepsilon\to 0}\frac{F(\psi+\varepsilon\eta)-F(\psi)}{\varepsilon}\\ &= \left.\frac{dF(\psi+\varepsilon\eta)}{d\varepsilon}\right|_{\varepsilon=0},\end{aligned} \tag{3.32}$$

where η is an arbitrary test function. This expression can be intuitively understood as finding the change of F in the direction of η. The analogy becomes apparent when comparing the expression to the directional derivative of a scalar field $f(\mathbf{x})$ in the direction of a vector $\mathbf{v}$:

$$D_{\mathbf{v}}f(\mathbf{x}) := \sum_{i=1}^{n}\frac{\partial f(x)}{\partial x_i}\,v_i = \nabla f\cdot\mathbf{v} \tag{3.33}$$

$$D_{\eta}F[\psi] := \int d^3r\,\frac{\delta F}{\delta\psi}(\mathbf{r})\,\eta(\mathbf{r})\,. \tag{3.34}$$

Plugging 3.30 into Eq. (3.32), we find

$$\begin{aligned}\int \frac{\delta F}{\delta\psi}(\mathbf{r})\,\eta(\mathbf{r})\,d^3r &= \frac{d}{d\varepsilon}\int d^3r\Bigg[\alpha|\psi+\varepsilon\eta| + \frac{\beta}{2}|\psi+\varepsilon\eta|^4\\ &\qquad +\gamma\,|\nabla(\psi+\varepsilon\eta)|^2\Bigg]\Bigg|_{\varepsilon=0}\\ &= \int d^3r\Big[\alpha(\psi^*\eta+\psi\eta^*) + \beta(\overbrace{\psi\psi^*}^{|\psi|^2}\psi^*\eta + \psi\overbrace{\psi\psi^*}^{|\psi|^2}\eta^*)\\ &\qquad +\gamma\left((\nabla\psi)^*(\nabla\eta)+(\nabla\psi)(\nabla\eta)^*\right)\Big]\,.\end{aligned}$$

Assuming that η vanishes at the boundaries, we can perform integration by parts for the kinetic energy terms and arrive at

$$\int \frac{\delta F}{\delta\psi}(\mathbf{r})\,\eta(\mathbf{r})\,d^3r = \int d^3r\left[\alpha\psi+\beta|\psi|^2\psi+\gamma\nabla^2\psi\right]\eta^* + \text{c.c.}$$

Finally, we can see that the prefactors of η and η^* have to vanish in order to fulfill 3.31. Since η and η^* are linearly independent, the differential equation for ψ is

$$\gamma\nabla^2\psi + \alpha\psi + \beta|\psi|^2\psi = 0\,. \tag{3.35}$$

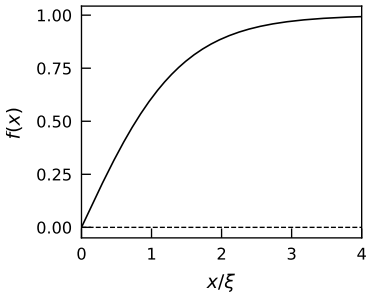


Figure 3.7: Recovery of $f(x)$ over the coherence length ξ, given by Eq. (3.39).

As an example of an inhomogeneity, we will now extract the length scale ξ at which the system recovers from a defect, also called the *Ginzburg-Landau coherence length*. For simplicity, we consider a 1D system with a defect at $x = 0$, giving the boundary condition $\psi(x = 0) = 0$.

Taking the knowledge from the Landau equation, for $x \to \infty$, we should obtain the homogeneous solution

$$\lim_{x\to\infty} \psi(x) = \sqrt{-\frac{\alpha}{\beta}}\,, \tag{3.36}$$

so we can define

$$\psi = \sqrt{-\frac{\alpha}{\beta}} f(x) \tag{3.37}$$

to rewrite 3.35 as

$$-\frac{\gamma}{\alpha} f''(x) + f(x) - f(x)^3 = 0\,. \tag{3.38}$$

With the boundary condition $f(0) = 0$, the solution for this differential equation is

$$f(x) = \tanh \frac{x}{\sqrt{2}\xi}\,, \tag{3.39}$$

with the coherence length

$$\xi = \sqrt{-\frac{\gamma}{\alpha}}\,. \tag{3.40}$$

A spatial profile of $f(x)$ is shown in Fig. 3.7.

3.3.3 Excitations related to the order parameter

So far, we have only considered time-independent solutions; however, in our experiment, we want to probe the dynamics of a superfluid. To include these dynamics in our model, it is convenient to use the Lagrange formalism and formulate an action which has to be minimized to derive the excitation spectrum:

$$S = \int dt \int d^3r \left[\mathcal{L}_{\text{dyn}} - \mathcal{F}\right]\,. \tag{3.41}$$

Here, $\mathcal{F}$ is just the integrand of the free energy functional $F[\psi]$ in Eq. (3.30), and $\mathcal{L}_{\text{dyn}}$ contains the dynamical terms. For this, we choose the two lowest-order time-reversal and time-invariant terms [25]

$$\mathcal{L}_{\text{dyn}} = -iK_1\psi^*\partial_t\psi + K_2|\partial_t\psi|^2\,, \tag{3.42}$$

where K_1 and K_2 are constants used to tune in and out the two different terms. Therefore, our full Lagrangian is

$$\mathcal{L} = \mathcal{L}_{\text{dyn}} - \mathcal{F} = -iK_1\psi^*\partial_t\psi + K_2|\partial_t\psi|^2 - \alpha|\psi|^2 - \frac{\beta}{2}|\psi|^4 - \gamma\left|\nabla\psi\right|^2\,. \tag{3.43}$$

If only the K_2 term is present, the system is Lorentz invariant[5] and therefore relativistic, while the K_1 term is not. As we will see in the following, the relativistic case ($K_1 = 0$) leads to two distinct

[5] This is due to the fact that the system features the terms $K_2|\partial_t\psi|^2 - \gamma\left|\nabla\psi\right|^2$, which together lead to Lorentz invariance.

modes: an ungapped Goldstone mode with linear k-dependence, and a massive *Higgs* mode, which is gapped and quadratic in k. These two modes correspond to oscillations of the phase and amplitude of the order parameter, respectively.

Now, we know that, at $T < T_c$, the equilibrium is at $\psi_0 = \sqrt{-\alpha/\beta}$, after arbitrarily choosing our phase $\phi_0 = 0$. Therefore, we can look at small perturbations around the uniform condensate

$$\psi(\mathbf{r}, t) = (\psi_0 + h(\mathbf{r}, t))\, e^{i\phi(\mathbf{r},t)} \tag{3.44}$$

to find the modes in the relativistic ($K_1 = 0$ and $K_2 = 1$) and non-relativistic ($K_1 = 1$ and $K_2 = 0$) case.

To quickly summarize the steps of the derivations below, for both cases, we first find the Lagrangian for the small perturbations by plugging the ansatz into Eq. (3.43). We then get the corresponding equations of motion by invoking the Euler-Lagrange equations. Finally, choosing a planar wave solution for the perturbations allows us to extract the energy spectrum.

Relativistic case

For the relativistic case, we start with the Lagrangian

$$\mathcal{L} = |\partial_t \psi|^2 - \gamma\, |\nabla\psi|^2 - \alpha|\psi|^2 - \frac{\beta}{2}|\psi|^4\,. \tag{3.45}$$

To get an expression for the first two terms, we compute the gradient and time derivative of the perturbation ansatz 3.44

$$\partial_t \phi = (\partial_t h + i(\psi_0 + h)\partial_t\phi)\, e^{i\phi} \tag{3.46}$$

$$\nabla\phi = (\nabla h + i(\psi_0 + h)\nabla\phi)\, e^{i\phi}\,. \tag{3.47}$$

By squaring and dropping terms beyond the second order, the first two terms of $\mathcal{L}$ equate to

$$|\partial_t\psi|^2 \approx (\partial_t h)^2 + \psi_0^2(\partial_t\phi)^2 \tag{3.48}$$

$$\gamma|\nabla\psi|^2 \approx \gamma(\nabla h)^2 + \gamma\psi_0^2(\nabla\phi)^2 \tag{3.49}$$

The last two terms in $\mathcal{L}$ govern the solution for the equilibrium and only depend on the amplitude $|\psi| = \psi_0 + h$. We therefore group them into the potential $V(|\psi|)$ and expand it to second order around ψ_0.

$$V(|\psi|) \approx V(\psi_0) + \frac{1}{2}\left.\frac{\partial^2 V}{\partial|\psi|^2}\right|_{\psi_0} h^2 \tag{3.50}$$

$$= V(\psi_0) + \frac{1}{2}\left(2\alpha + 6\beta\psi_0^2\right) h^2 \tag{3.51}$$

$$= V(\psi_0) - 2\alpha h^2 \tag{3.52}$$

The first-order term vanishes, since V is minimal at ψ_0. Additionally, since the constant term $V(\psi_0)$ does not contribute to the dynamics,

we omit it from the Lagrangian. Combining all terms, we arrive at the Lagrangian up to second order

$$\mathcal{L}_{\text{quad}} = (\partial_t h)^2 - \gamma(\nabla h)^2 + 2\alpha h^2 + \psi_0^2 \left[(\partial_t \phi)^2 - \gamma(\nabla\phi)^2\right] , \quad (3.53)$$

which can be simplified further by rescaling the phase to $\theta = \psi_0\phi$, leading to

$$\mathcal{L}_{\text{quad}} = (\partial_t h)^2 - \gamma(\nabla h)^2 + 2\alpha h^2 + (\partial_t \theta)^2 - \gamma(\nabla\theta)^2 . \quad (3.54)$$

We arrive at the equations of motion by invoking the Euler-Lagrange equations

$$\partial_t \left(\frac{\partial \mathcal{L}}{\partial(\partial_t f_i)}\right) + \nabla \cdot \left(\frac{\partial \mathcal{L}}{\partial(\nabla f_i)}\right) - \frac{\partial \mathcal{L}}{\partial f_i} = 0 \quad (3.55)$$

for each independent field f_i, which is the amplitude h and phase θ. Plugging in the Lagrangian 3.54, for the phase we get

$$\overbrace{\partial_t(2\partial_t\theta)}^{\partial_t\left(\frac{\partial\mathcal{L}}{\partial(\partial_t\theta)}\right)} \overbrace{-2v^2\nabla^2\theta}^{\nabla\cdot\left(\frac{\partial\mathcal{L}}{\partial(\nabla\theta)}\right)} - \overbrace{\vec{0}}^{\frac{\partial\mathcal{L}}{\partial f_i}} = 0 \quad (3.56)$$

which simplifies to

$$\partial_t^2\theta - \gamma\nabla^2\theta = 0 . \quad (3.57)$$

Analogously, for the amplitude h, we get

$$\partial_t^2 h - \gamma\nabla^2 h - 2\alpha h = 0 . \quad (3.58)$$

Choosing a plane wave solution for both fields

$$\theta(\mathbf{r}, t) \propto e^{i(\mathbf{k}\cdot\mathbf{r}-\omega t)},\ h(\mathbf{r}, t) \propto e^{i(\mathbf{k}\cdot\mathbf{r}-\omega t)} \quad (3.59)$$

allows us to directly compute the dispersion for the Goldstone (phase)

$$-\omega^2 + \gamma k^2 = 0 \Rightarrow \boxed{\omega_G(k) = \sqrt{\gamma}k} \quad (3.60)$$

and the Higgs (amplitude) mode

$$-\omega^2 + \gamma k^2 - 4\alpha = 0 \Rightarrow \boxed{\omega_H(k) = \sqrt{\gamma k^2 - 4\alpha}} \quad (3.61)$$

As we can see, the Goldstone mode is an ungapped sound mode with linear dispersion, while the amplitude mode has a gap of $\Delta_h = 2\sqrt{-\alpha} = 2\sqrt{|\alpha|}$ and behaves quadratically for $k \ll 1$ (see Fig. 3.8).

Non-relativistic case

For the non-relativistic case, we start with the Lagrangian

$$\mathcal{L} = -i\psi^*\partial_t\psi - \gamma\left|\nabla\psi\right|^2 - \alpha|\psi|^2 - \frac{\beta}{2}|\psi|^4 . \quad (3.62)$$

For the derivation of the excitation spectrum here, it is more convenient to express ψ in Cartesian coordinates, again assuming small perturbations of the amplitude $h \ll 1$ and phase $\phi \ll 1$, leading to

$$\psi = (\psi_0 + h)e^{i\phi} \approx \psi_0 + h + i\psi_0\phi = \psi_0 + u + iv . \quad (3.63)$$

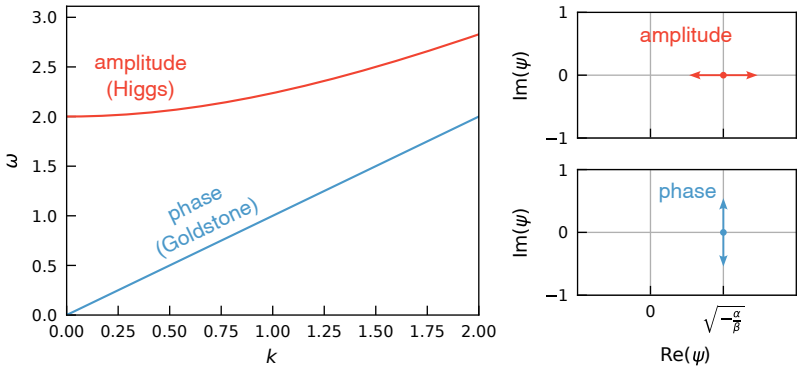


Figure 3.8: Dispersion for the Lorentz invariant system (left). Two distinct modes are visible, corresponding to a massive amplitude and a massless phase oscillation of the order parameter, as illustrated in the top and bottom-right panels, respectively.

To get the Lagrangian, we again start with the time-dependent term

$$i\psi^*\partial_t\psi = i(\psi_0 + u - iv)\partial_t(\psi_0 + u + iv)\,. \tag{3.64}$$

Since constants do not change the dynamic, and the equilibrium causes first-order terms to vanish, the term becomes

$$i\psi^*\partial_t\psi \to v\partial_t u - u\partial_t v\,. \tag{3.65}$$

At this point, we can already see that, unlike in the relativistic case, the phase and amplitude are coupled. The remaining terms in the Lagrangian we treat analogously to the relativistic case and arrive at

$$\mathcal{L}_{\text{quad}} = v\partial_t u - u\partial_t v - \gamma\left[(\nabla u)^2 + (\nabla v)^2\right] + 2\alpha u^2\,. \tag{3.66}$$

Invoking the Euler-Lagrange equations again, for both u and v, we get the equations of motion

$$\partial_t v = 2\gamma\nabla^2 u + 4\alpha u \tag{3.67}$$

$$\partial_t u = -2\gamma\nabla^2 v \tag{3.68}$$

Plugging in a planar solution for u and v

$$u(\mathbf{r},t) = u_k e^{i(\mathbf{k}\cdot\mathbf{r}-\omega t)},\ v(\mathbf{r},t) = v_k e^{i(\mathbf{k}\cdot\mathbf{r}-\omega t)} \tag{3.69}$$

then leads to

$$-i\omega v_k = -2\gamma k^2 u_k + 4\alpha u_k \tag{3.70}$$

$$-i\omega u_k = 2\gamma k^2 v_k\,. \tag{3.71}$$

From the second equation, we get

$$v_k = -i\frac{\omega}{2\gamma k^2}u_k\,, \tag{3.72}$$

which we plug into the first equation and get

$$-\frac{\omega^2}{2\gamma k^2}u_k = -(2\gamma k^2 - 4\alpha)u_k\,. \tag{3.73}$$

After rearranging, we get the well-known Bogoliubov dispersion

$$\boxed{\omega_B(k) = \sqrt{2\gamma k^2(2\gamma k^2 - 4\alpha)} = \sqrt{c^2k^2 + (2\gamma k^2)^2}} \tag{3.74}$$

With $c^2 = -8\alpha\gamma$ being the sound velocity. In Fig. 3.9, we can see that, at low k, the mode has linear dispersion, which becomes quadratic at higher k. Additionally, by plotting the evolution of ψ, we can see that in the linear regime, only the phase (the imaginary part of ψ) fluctuates, while amplitude fluctuations mix in at higher k.

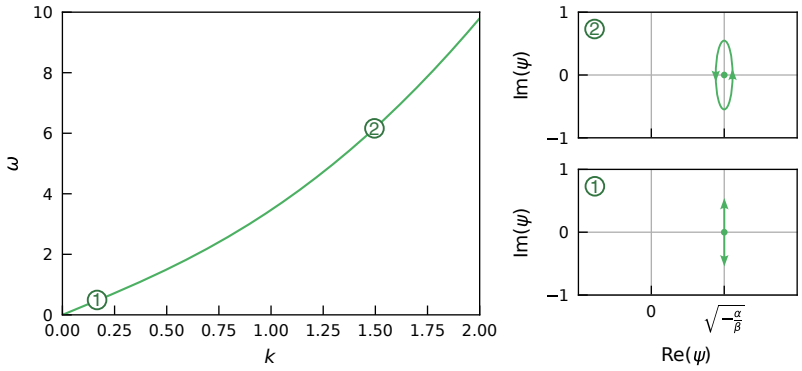


Figure 3.9: Dispersion for the non-relativistic system (left). The spectrum takes the shape of the well-known Bogoliubov dispersion. At low momenta, the excitation is purely an oscillation of the phase of the order parameter (top right), while both the phase and amplitude oscillate for larger momenta (bottom right).

3.3.4 Connecting Ginzburg-Landau with microscopic theories

We now have a good idea of how an order parameter and corresponding collective modes arise from a spontaneous breaking of the $U(1)$ symmetry. To justify the applicability, we now connect the microscopic BCS to Ginzburg-Landau theory, and show that the Lorentz invariant case holds in the BCS regime due to particle-hole symmetry, while it breaks down for a BEC.

Let us first consider the time-independent solutions. Shortly after the BCS theory was developed, Gor'kov found that, by using Green's functions, the microscopic BCS Hamiltonian maps onto the static Ginzburg-Landau theory [26]. However, since the precise steps of the mapping go beyond the scope of this thesis, the reader is referred to the original paper or a more detailed derivation in [27]. The same result can be obtained by instead applying a Hubbard-Stratonovich transformation to the partition function using the BCS Hamiltonian [28] and expanding around the critical temperature T_c.

These solutions are static and therefore do not include information about collective modes; the microscopic theory needs to be extended to incorporate dynamics. We therefore look at the time-dependent Bogoliubov-de Gennes (BdG) equations, which are obtained when extending the mean-field BCS Hamiltonian 3.5 to include gradients and plugging it into the Schrödinger equation

$$i\partial_t \begin{pmatrix} u(\mathbf{r},t) \\ v(\mathbf{r},t) \end{pmatrix} = \begin{pmatrix} \hat{h}_0 & \Delta(\mathbf{r},t) \\ \Delta^*(\mathbf{r},t) & -\hat{h}_0 \end{pmatrix} \begin{pmatrix} u(\mathbf{r},t) \\ v(\mathbf{r},t) \end{pmatrix}, \tag{3.75}$$

where $\hat{h}_0 = -\frac{\nabla^2}{2m} - \mu$. The most important property of these equations is that they are particle-hole symmetric, meaning that the 2×2 matrix elements fulfill $H_{11} = -H_{22}^*$ and $H_{12} = H_{21}^*$. This makes them Lorentz

invariant[6] [30], again introducing the squared time derivative that leads to the phase and amplitude modes being decoupled. In the BCS regime, the dispersions of these modes are [30]

$$\omega_G(k) = ck \tag{3.76}$$

$$\omega_H(k) = \sqrt{(2\Delta)^2 + c^2k^2}\,, \tag{3.77}$$

with the sound velocity $c \approx v_\mathrm{F}/\sqrt{3}$ and Fermi velocity $v_\mathrm{F} = k_\mathrm{F}/m$. Comparing this with Eq. (3.60) and (3.61), we can relate γ and α from the phenomenological theory to the parameters in our relativistic microscopic theory:

$$\gamma = c^2 = \frac{k_\mathrm{F}^2}{3m^2}\,,\ \alpha = -\Delta^2\,. \tag{3.78}$$

Things change drastically when going to the BEC regime. Formally, the BdG equations are particle-hole symmetric in the entire crossover, but this symmetry becomes suppressed as Δ becomes much larger than E_F and the pairs become tightly bound, thereby losing the fermionic character. As a result, the BdG equations reduce to the Gross-Pitaevskii equations [31], which are used to model BEC dynamics

$$i\hbar\partial_t\psi(\mathbf{r},t) = \left(-\frac{\hbar^2}{2m}\nabla^2 + g|\psi(\mathbf{r},t)|^2\right)\psi(\mathbf{r},t)\,. \tag{3.79}$$

As we can see, this equation features only a first-order time derivative and is very similar to the non-Lorentz-invariant Ginzburg-Landau theory. As a result, we again arrive at the well-known Bogoliubov dispersion

$$\hbar\omega(k) = \sqrt{\epsilon_k(\epsilon_k + 2gn)}\,. \tag{3.80}$$

We can relate γ and α to the microscopic theory by comparing with the non-relativistic Ginzburg-Landau theory 3.74:

$$\gamma = \frac{\hbar^2}{4m}\,,\ \alpha = -\frac{gn}{2}\,. \tag{3.81}$$

It should be noted, however, that the interpretation of the high-momentum limit, where the Bogoliubov mode becomes quadratic, differs between the microscopic and Ginzburg-Landau theories. In Ginzburg-Landau theory, the quadratic behavior results from mixing between the amplitude and phase modes, whereas in the microscopic theory, the excitation gains single-particle character, which is also quadratic. These two interpretations are fundamentally different, since the amplitude mode is collective, whereas single-particle excitations clearly are not. Since Ginzburg-Landau theory is a phenomenological theory valid in the long-wavelength (low-k) regime, the correct interpretation of the quadratic behavior lies in the single-particle excitations of the microscopic theory.

Additionally, the predictions for the BEC and BCS regimes smoothly connect in the crossover. When going from the BCS to the BEC regime, the amplitude mode vanishes, while the sound mode becomes quadratic at large k. Since, in microscopic theory, this mode is called "(Anderson-)Bogoliubov" or "sound" mode in the crossover, we will do the same in the following and use these labels interchangeably.

[6] Not only are they Lorentz invariant, but they are also formally equivalent to the Dirac equation [29].

3.4 Fermi gases in 2D

3.4.1 Scattering and the BEC-BCS crossover

We now turn towards 2D Fermi gases, which are the central topic of this thesis. Generally, when compressing a superfluid into a 2D regime, many of the concepts introduced, such as Cooper pairing, the superfluid order parameter, and the collective modes derived from the Ginzburg-Landau theory, remain valid, as these arguments are independent of the dimensionality. However, a few things change drastically, starting from the interactions. The change of numerous key quantities is summarized in Tab. 3.1.

Table 3.1: Different fundamental quantities of a Fermi gas in 2D and 3D.

	3D	2D
Fermi wave number k_F	$(6\pi^2 n)^{1/3}$	$\sqrt{4\pi n}$
Fermi energy E_F	$\frac{(6\pi^2 n)^{2/3}\hbar^2}{2m}$	$\frac{2\pi n\hbar^2}{m}$
binding energy E_F	$\frac{\hbar^2}{m a_{3\mathrm{D}}^2}$	$\frac{\hbar^2}{m a_{2\mathrm{D}}^2}$
density of states ρ_DOS	$\frac{m^{3/2}V}{\sqrt{2}\pi^2\hbar^3}\sqrt{E}$	$\frac{mV}{2\pi\hbar^2}$
scattering amplitude $f(k)$	$-\frac{a_{3\mathrm{D}}}{1+ika_{3\mathrm{D}}}$	$\frac{4\pi}{-2\ln(ka_{2\mathrm{D}})+i\pi}$
scattering crossection σ	$\frac{4\pi a_{3\mathrm{D}}^2}{1+k^2 a_{3\mathrm{D}}^2}$	$\frac{32\pi^3}{4\ln(ka_{2\mathrm{D}})^2+\pi^2}$

First of all, scattering itself changes, leading to a logarithmic dependency on the scattering length $\ln(k_\mathrm{F}a_{2\mathrm{D}})$, instead of $1/k_\mathrm{F}a_{3\mathrm{D}}$ in the three-dimensional case. This becomes apparent when considering the scattering amplitude $f(k)$, which quantifies how much of an incoming wave is scattered in a given direction of a spherical wave

$$\psi(\mathbf{r}) = e^{ikz} + f(\mathbf{k})\frac{e^{ikr}}{r}\,. \tag{3.82}$$

For s-wave scattering in 3D at low energies, it can be approximated to [3]

$$f^{(3\mathrm{D})}(k) = -\frac{a_{3\mathrm{D}}}{1+ika_{3\mathrm{D}}}\,. \tag{3.83}$$

In the 2D case, however, the scattering amplitude has a logarithmic dependency on $a_{2\mathrm{D}}$ [32]:

$$f^{(2\mathrm{D})}(k) = \frac{4\pi}{-2\ln(ka_{2\mathrm{D}})+i\pi}\,. \tag{3.84}$$

This also has the consequence that 3D has a unitary point, where the system is strongly interacting but independent of $a_{3\mathrm{D}}$, whereas in 2D this point does not exist. In 3D, for $a_{3\mathrm{D}} \to \infty$ the scattering amplitude tends towards $f \to -1/ik$, leading to a scattering crossection $\sigma_{3\mathrm{D}} = 4\pi/k^2$, which is independent of $a_{3\mathrm{D}}$. We can see from Eq. 3.84 that this point does not exist in 2D due to the logarithmic dependence. At both, $a_{2\mathrm{D}} \to 0$ and $a_{2\mathrm{D}} \to \infty$, $a_{2\mathrm{D}}$ does not cancel out. Instead, both regimes actually become weakly interacting, and the strongly interacting regime is located around $\ln(k_\mathrm{F}a_{2\mathrm{D}}) \approx 0$.

Another major change is the behavior of the bound state. As explained in Ch. 3.1.1 in a 2D geometry, a two-particle bound state

exists for arbitrarily weak interactions, with the binding energy given by the same form as in 3D:

$$E_{\mathrm{B}} = \frac{\hbar^2}{m a_{\mathrm{2D}}^2} \,. \tag{3.85}$$

As a result, the gap and number equations drastically simplify to [33]

$$\Delta = \sqrt{E_{\mathrm{B}} E_{\mathrm{F}}} \tag{3.86}$$

$$\mu = E_{\mathrm{F}} - E_{\mathrm{B}}/2 \,, \tag{3.87}$$

instead of the complicated Eq. (3.16) and (3.17) that have to be solved using elliptical integrals. As in the 3D case, the chemical potential in the BEC regime is dominated by the binding energy, while on the BCS side it approaches E_{F}.

3.4.2 The Berezinskii-Kosterlitz-Thouless phase transition

There is another major change in the physics when going to 2D. The famous Mermin-Wagner-Hohenberg theorem [34, 35] states that condensation at finite temperatures is generally not possible in 2D systems. This breakdown of superfluidity comes from quantum fluctuations that become relevant in reduced dimensions. However, in finite-size systems, this limit can be overcome by vortices pairing up, stabilizing coherence. The microscopic theory describing this phenomenon was developed by Berezinskii, Kosterlitz, and Thouless [36, 37], hence the name *BKT phase*.

To quantify this stabilization, we look at the first-order correlation function

$$g^{(1)}(r) = \langle \psi^\dagger(r)\psi(0) \rangle \,, \tag{3.88}$$

with the bosonic creation operator $\psi(r)$. In the case of a 3D superfluid, $g^{(1)}$ takes a constant value, meaning that coherence holds for arbitrarily large distances. A thermal gas ($T > T_c$), on the other hand, is not coherent, since $g^{(1)}$ decreases exponentially. For a 2D superfluid, however, $g^{(1)}$ only decreases algebraically

$$g^{(1)} \propto \left(\frac{1}{r}\right)^{\frac{1}{n_s \lambda_T^2}} \,, \tag{3.89}$$

which restores coherence in finite-size systems, specifically when the system size is smaller than the coherence length.

In these systems, the previously introduced theories for superfluidity and their interconnections still hold.

3.4.3 The quasi-2D regime

Of course, it is impossible to fully eliminate one dimension in reality, meaning that the atoms cannot be confined to a true 2D geometry: In cold atom experiments, the atoms are typically confined by using dipole traps with large trap frequencies, and the wave function will

always have some finite extent along this confined direction. On first sight, the task of creating a 2D system seems hopeless. However, if our chemical potential μ and temperatures T are low enough, we can reach the point at which the atoms occupy only the lowest energy level of the confining potential. Therefore, even though the wavefunction has an extent given by the harmonic oscillator length $l_z = \sqrt{\hbar/(m\omega_z)}$, with the trap frequency ω_z, dynamics along this direction are effectively frozen out. We call this regime, where $\mu, k_\mathrm{B}T < \hbar\omega_z$, the "quasi-2D" regime[7].

[7] Some publications also use the term "quasi-2D" for systems, where $\mu > \hbar\omega_z$, which can be misleading. We prefer calling this the "intermediate-2D-regime" to clearly distinguish between systems where the discretization of the confined dimension becomes relevant while $\mu > \hbar\omega_z$, and systems where dynamics along the confined direction are actually frozen out $\mu < \hbar\omega_z$.

Of course, since we still tune interactions using Feshbach resonances, we need to connect $a_{3\mathrm{D}}$ to $a_{2\mathrm{D}}$, which is possible by considering the scattering amplitude that has been derived by Petrov and Shlyapnikov [38]

$$f^{(\mathrm{quasi2D})}(k) = \frac{4\pi}{\sqrt{2\pi}l_z/a_{3\mathrm{D}} + w(k^2 l_z^2/2)} \,. \tag{3.90}$$

Here, $w(x)$ is a rather complicated function, but in our low-momentum limit ($x \ll 1$) it simplifies to [38]

$$w(k^2 l_z^2/2) \approx -\ln\left(\frac{2\pi}{A}\frac{k^2 l_z^2}{2}\right) + i\pi \,, \tag{3.91}$$

[8] The original manuscript [38] states $A \approx 0.915$, which is incorrect. The actual value is $A \approx 0.905$, see e.g. [39–41].

with $A \approx 0.905$[8], leading to

$$f^{(\mathrm{quasi2D})}(k) \approx \frac{4\pi}{\sqrt{2\pi}l_z/a_{3\mathrm{D}} - \ln\left(\frac{2\pi}{A}\frac{k^2 l_z^2}{2}\right) + i\pi} \,. \tag{3.92}$$

By comparing this scattering amplitude with the true-2D one in Eq. 3.84, we can directly see that the scattering lengths are related via

$$a_{2\mathrm{D}} = l_z\sqrt{\frac{\pi}{A}}e^{-\sqrt{\frac{\pi}{2}}l_z/a_{3\mathrm{D}}} \,. \tag{3.93}$$

This definition is used to parametrize the 2D interactions for all results presented in this thesis. Note that there are two distinct definitions of the scattering length, which are identical in the 1D and 3D cases but yield different results in 2D. In our case, we defined $a_{2\mathrm{D}}$ via the 2D binding energy $E_\mathrm{B} = \hbar^2/ma_{2\mathrm{D}}^2$, which is also the definition used, e.g., by Petrov et al. [38]. The other definition uses the analytic continuation of the scattering wavefunction to small distances to calculate a_2 and is used, e.g., in [42, 43]. Fortunately, these definitions are related by a simple factor $a_{2\mathrm{D}} = (a_2/2)e^{-\gamma_\mathrm{E}} \approx 1.123a_2$, slightly shifting the interaction parameter $\ln(k_\mathrm{F}a_{2\mathrm{D}}) = \ln(k_\mathrm{F}a_2) - 0.113$.

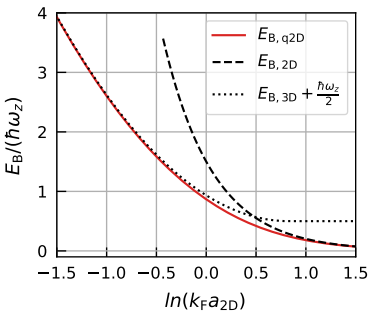


Figure 3.10: Binding energies for varying interactions in the quasi-2D system. On the BEC side, the pair size is small compared to l_z, and it approaches the 3D binding energy, offset by the energy from the confinement. In the BCS limit, the opposite is the case, and the energy approaches the 2D binding energy.

Another quantity that is modified is the binding energy, which is a direct result of the varying pair size in the BEC-BCS crossover. On the BCS side, the pair size is much larger than the harmonic oscillator length l_z, and the binding energy follows the 2D description in Eq. (3.85). In the BEC regime, on the other hand, the pairs are bound in Feshbach molecules of comparable or smaller size than l_z and therefore follow $E_{\mathrm{B,3D}} + \hbar\omega_z$. An interpolation between these regimes can be obtained by solving [39]

$$\frac{l_z}{a_{3\mathrm{D}}} = \int_0^\infty \frac{du}{\sqrt{4\pi u^3}}\left(1 - \frac{e^{\frac{-E_{\mathrm{B,quasi\,2D}}}{\hbar\omega_z}}}{\sqrt{\frac{1}{2u}\left(1 - e^{-2u}\right)}}\right) \,. \tag{3.94}$$

In Fig. 3.10, we can see how the solution smoothly transitions between the two regimes.

3.4.4 Confinement induced modes

In quasi-2D systems, we find the same modes as in the 3D and 2D case: In the BEC regime, there is a Bogoliubov mode that turns from a linear sound mode at low momenta k to a quadratic dispersion at large k, while on the BCS side, both a distinct Goldstone and amplitude mode exist. However, there is an additional family of modes that appears when strongly confining quantum gases, stemming from the discrete energy levels of the trapping potential: The multibranch Bogoliubov spectrum.

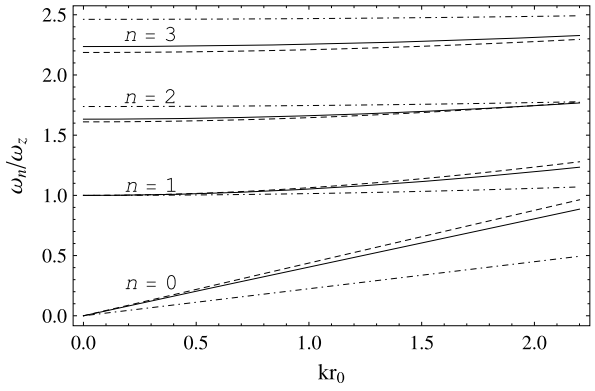


Figure 3.11: Multibranch Bogoliubov spectrum obtained from hydrodynamic theory in a flat trapping geometry. The BEC ($1/k_\mathrm{F}a = 6$), BCS ($1/k_\mathrm{F}a = -0.5$), and unitary regime ($1/k_\mathrm{F}a = 0$) are depicted by the dash-dotted, dashed, and solid lines, respectively. Adapted from [44].

The original discussion by Zaremba [45] considers a cylindrically confined Bose gas and finds a family of gapped modes induced by the discrete level spacing of the confining potential. This model has been extended by Ghosh et al. [46] to describe these modes in the BEC-BCS crossover, and Qin et al. [44] subsequently solved the problem in a flat geometry similar to our experiment. A momentum-resolved energy spectrum $E_{n_\mathrm{MBS}}(k)$ of these modes is shown in Fig. 3.11, where n_MBS is the axial quantum number, corresponding to n in the figure. We can see that the $n_\mathrm{MBS} = 0$ excitation is an in-plane mode, corresponding to the previously introduced sound mode. The additional modes at higher energies stem from the multibranch Bogoliubov spectrum and can be understood as monopole (breathing) and dipole (center-of-mass) modes for even and uneven n_MBS, respectively. The resulting density deformations $\delta n(z, \omega t - kx)$ visualizing the center-of-mass and breathing character are shown in Fig. 3.12.

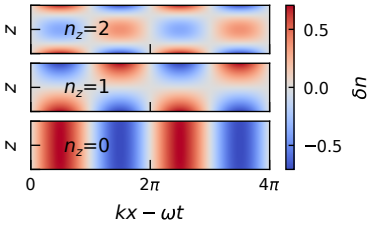


Figure 3.12: Density deformation δn of the stationary solution caused by the different modes from the multibranch spectrum. The x-axis can be understood both as a temporal and spatial axis, since the system oscillates spatially with the wave number k when moving along r, and with the frequency ω over a time t. The in-plane mode ($n_z = 0$) is a regular sound mode, while the higher-lying modes also exhibit vertical motion.

While this description is great for an intuitive understanding of confinement-induced modes, our systems differ from the limits used in these publications, and the quantitative predictions are not suited for a comparison. The main difference is that [44–46] consider the Thomas-Fermi limit. Most notably, in their calculations, they have a system that occupies not only the ground state of the confining potential but also many higher-lying levels, meaning that they are

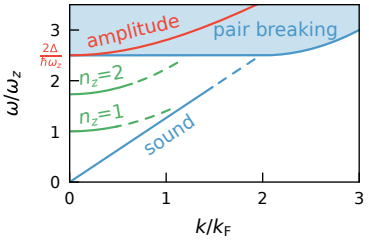


Figure 3.13: Spectrum including all modes discussed in this chapter. The amplitude mode, starting at 2Δ, the sound mode, and the pair-breaking continuum are all in-plane ($n_z = 0$) while the multibranch Bogoliubov spectrum (green) results from the trapping geometry.

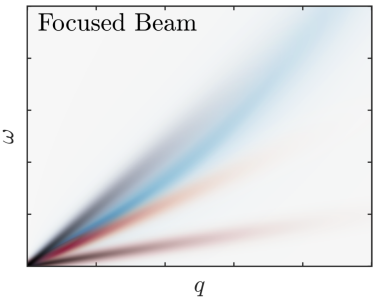


Figure 3.14: Excitations addressed by dragging a stirrer through the gas at three different velocities. The area probed by the stirrer is colored red and black, while the sound mode is colored blue. Adapted from [47].

actually in the 3D limit. Additionally, they consider the hydrodynamic regime, which is not valid for weak interactions. Since we focus on the quasi-2D regime, only the ground state of the confining potential is occupied. As we will see, the modes correspond directly to excitations from the ground state to individual levels. This becomes apparent when considering the non-interacting BEC case where the energy of zero-momentum excitations approaches the harmonic-oscillator level spacing, $\hbar\omega_z$, whereas the hydrodynamic theory predicts different energies, namely

$$E_{n_{\mathrm{MBS}}}(k=0) = \hbar\omega_z \sqrt{\frac{\gamma}{2} n_{\mathrm{MBS}} \left(n_{\mathrm{MBS}} + \frac{2}{\gamma} - 1 \right)} \,. \tag{3.95}$$

Here, γ is determined by the density dependence of the chemical potential $\mu \propto n^\gamma$, which is 1 in the BEC regime and $2/3$ for a unitary and a non-interacting Fermi gas. This leads to e.g. $E_2(k=0) = \sqrt{3}\hbar\omega_z$ instead of $2\hbar\omega_z$ for a non-interacting BEC.

However, the general features of the spectra shown in Fig. 3.11 are preserved, namely an in-plane sound mode ($n_z = 0$) that is linear for low momenta and a family of higher-lying transverse modes that feature a quadratic dispersion.

All modes combined then result in the spectrum sketched in Fig. 3.13.

3.5 Experimental observation of collective modes

3.5.1 Bogoliubov mode

We now look at previous studies that have examined the modes discussed above, starting with the Bogoliubov mode. Since this is a sound mode, it is directly linked to density fluctuations and is therefore very easy to excite. This mode actually sets the critical velocity, as was done in early experiments probing the Landau criterion, in which a stirrer is dragged through a superfluid [48–52]. As long as the stirrer moves slower than the critical velocity v_c, no excitations occur. In the momentum-resolved spectrum discussed in the previous chapters, this corresponds to addressing all excitations that lie on a straight line that starts at the origin ($\omega = 0, k = 0$), with the slope determined by the velocity of the stirrer (see Fig. 3.14). Since the sound mode has a finite width, v_c is lower than the sound velocity, and at $T > T_c$ excitations for arbitrarily small velocities exist. Additionally, one can introduce sound waves into the system to directly measure the speed of sound [53]. A more involved approach is Bragg spectroscopy, as performed in [6, 8, 9, 54–58], which allows excitations of the system at combinations of well-defined momenta and energies. With this probing scheme, it was possible to extract textbook-quality spectra of the sound mode (Fig. 3.15), as well as v_c from the onset of the sound mode, and T_c from the temperature at which the extracted v_c vanishes. Bragg spectroscopy is also able to detect pair-breaking excitations, as shown in Fig. 3.16. Since the onset of the continuum is

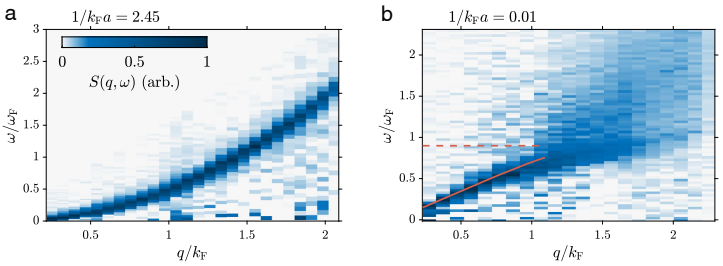


Figure 3.15: Bragg spectroscopy measurements on a 3D homogeneous Fermi gas. a) Excitation spectrum in the BEC regime, showing the typical Bogoliubov dispersion. b) Towards strong interactions, the sound velocity increases and the pair-breaking continuum becomes visible at larger q. The dashed line marks the onset of the pair-breaking continuum. Adapted from [8].

located at an energy of 2Δ for a BCS-type superfluid, as explained in Ch. 3.2, it provides a way to measure the superfluid gap. Therefore, previous studies have quantified Δ in 3D [8] and 2D [9] Fermi gases, enabling comparison between the two.

A short explanation of Bragg spectroscopy in our experiment will be presented in Ch. 4.3.3, while a more detailed description can be found in [47, 59].

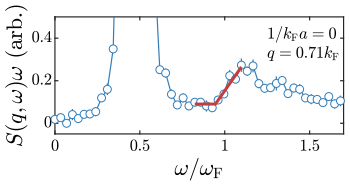


Figure 3.16: Extraction of the superfluid gap Δ by taking a slice at a finite momentum. The onset of the pair-breaking continuum at 2Δ is clearly visible (red line). Adapted from [8].

3.5.2 Amplitude mode

Observing the amplitude mode, on the other hand, is significantly more challenging for two reasons: First, it does not couple to density fluctuations, but to modulations of the interaction; and second, it decays very quickly because it lies in the pair-breaking continuum.

In charge density wave (CDW) superconductors, the amplitude mode has been observed as early as 1980 [62, 63] but was only later identified as such [64, 65]. This was possible because the CDW couples to the superfluid order, which also pushes the amplitude mode below the pair-breaking continuum [66]. However, in s-wave superconductors without CDW, the detection is significantly more challenging and only became possible after the development of high-power THz sources [60]. The first observation was reported by Matsunaga et al. in 2013 [61], more than three decades later, where a strong THz pump pulse quenched the system. This led to amplitude oscillations of the order parameter (see Fig. 3.17), as evidenced by changes in the probe pulse's electric field. In a follow-up study, the order parameter was periodically modulated, again with a THz pump pulse [67].

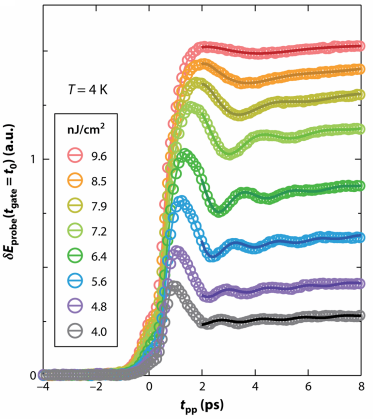


Figure 3.17: Higgs oscillations after quenching the system with a THz pump pulse. The difference in the electric field of the probe pulse shows oscillations that fit well with theory predictions for the amplitude mode. Adapted from [60, 61].

In cold-atom experiments, the amplitude mode has so far been observed in two ways. The first experiment, performed by the Köhl group, used an off-resonant RF field to modulate the occupation of the second and the initially unoccupied third lowest hyperfine state $|2\rangle$ and $|3\rangle$, respectively. This modulates the superfluid order parameter of the $|1\rangle$–$|2\rangle$ mixture at the Rabi frequency Ω_R. As a result, they observed heating at the frequencies consistent with the amplitude mode ($2\Delta/h$) for various interactions.

Alternatively, one can directly modulate the interactions by varying the magnetic field, which was done in the Köhl group [68] and the Vale group [58]. While the former observed heating at 2Δ via periodic modulation, the latter quenched the interactions and observed free

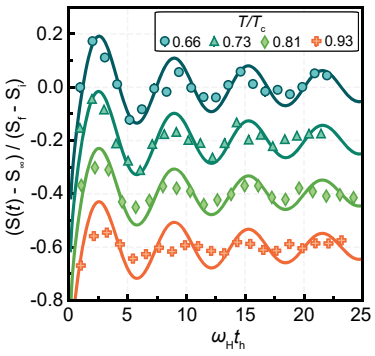


Figure 3.18: Higgs oscillations after quenching the interactions of the system via a magnetic field jump. The y-axis shows the response measured by Bragg spectroscopy of the pair-breaking continuum, which is modulated by the order-parameter oscillations. Adapted from [58].

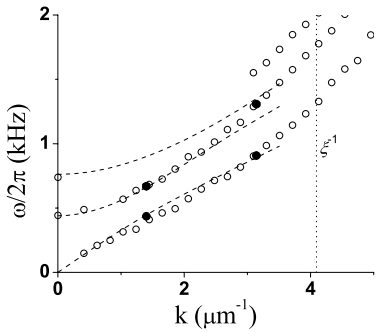


Figure 3.19: Observation of the multibranch Bogoliubov spectrum via Bragg spectroscopy. The experimental points (circles) show good agreement with the theory in [45] (dashed lines). Adapted from [69].

oscillations of the order parameter (see Fig. 3.18), very similar to those shown in Fig. 3.17.

In Part II, we will see that the amplitude mode can also be excited via trap-modulation spectroscopy, since it modulates l_z and therefore the interactions a_{2D}.

3.5.3 Confinement induced modes

The multibranch Bogoliubov spectrum has been probed via Bragg spectroscopy by Steinhauer et al. [69] for a cylindrical BEC, where they found good agreement with the predictions in [45] (see Fig. 3.19). However, studies of Fermi gases in the BEC-BCS crossover and in flat-trapping geometries are still lacking. Additionally, there are currently no experiments on these modes in the quasi-2D limit, which is not covered by the hydrodynamic theory of [44–46].

The dynamics of strongly confined systems are also of great interest in thin-film superconductors, or superconducting nanowires. Here, Blatt and Thompson have predicted the existence of shape resonances that occur whenever the energy of a transverse energy level crosses the Fermi energy [70]. This can lead to an enhancement of the superconducting gap Δ, which has been observed, e.g., in [71, 72].

In this thesis, we aim to determine how these strongly confined modes modify the dynamics of superfluids, especially in the limit where their energies are comparable to the energy scales of the 2D system, and to use them as a tool to probe superfluidity and quantum many-body phenomena. To achieve this, we will primarily focus on the second excited ($n_z = 2$) mode, as it is readily accessible with the spectroscopic techniques at our disposal.

More precisely, in Part II, we show that this mode persists in the entire BEC-BCS crossover and shifts in energy. Eventually, in the BCS regime, the energy crosses that of the amplitude mode, leading to a hybridization. Additionally, since this mode is a Goldstone mode associated with the superfluid order parameter, we observe that it vanishes near T_c, making it a useful probe of superfluidity. We extend our understanding of this mode in Part III, where we will see that it can be mapped to the polaron problem. This theory is also able to consider excitations at finite momenta, so besides the polaron energy and quasi-particle residue, we are able to extract the effective mass m^*. Finally, in Part IV, we use this mode as an indicator for the existence of a superfluid in a locally imbalanced system in order to shed light on the superfluid phase diagram of 2D imbalanced Fermi gases.

4 EXPERIMENTAL APPARATUS

In this chapter, I will explain the experimental apparatus and sequence that allow us to create and probe ultracold 2D Fermi gases with a high degree of control. A special emphasis will be placed on the upgrades that were implemented during the course of this work and, most notably, were imperative for the creation of the first 2D imbalanced Fermi gases below the superfluid critical temperature, presented in Ch. 8.

4.1 Overview of the experimental apparatus

Our experiment is able to create a 2D Fermi gas at temperatures lower than $T = 0.02T_{\mathrm{F}}$, which is well below the superfluid critical temperature $T_{\mathrm{BKT}} \approx 0.1\,T_{\mathrm{F}}$ in 2D [6, 73]. It allows us to cleanly control a broad range of parameters, including interactions, the density of each hyperfine state[9] (spin imbalance), and temperature. Additionally, we have a versatile set of tools at our disposal to probe various properties. These include a microscope to acquire in situ density images; Bragg spectroscopy, which enables us to measure momentum-resolved spectra; and trap-modulation spectroscopy, which allows us to readily access confinement-induced excitations.

[9] Introducing a spin imbalance, however, limits the minimum temperatures we can reach (see Ch. 9.1).

We use ^{6}Li in the lowest two hyperfine states, namely $|1\rangle = |F = 1/2, m_F = 1/2\rangle$ and $|2\rangle = |F = 1/2, m_F = -1/2\rangle$, which have a broad Feshbach resonance at 832 G, allowing us to freely tune the interactions from attractive to repulsive. Due to its light mass and strong interactions, evaporative cooling is very effective and reliably reaches temperatures well below T_{BKT}.

Throughout the experimental sequence, the atoms are suspended in ultra-high vacuum at $\sim 1 \times 10^{-11}$ mbar to prevent losses and heating due to collisions with particles from the air. This vacuum is provided by a multi-chamber setup, which will be discussed in more detail in Ch. 4.2 as we go through the preparation steps.

The final trap is a purely repulsive, homogeneous box potential that squeezes the atoms to the 2D regime, with $E_{\mathrm{F}}, \mu < \hbar\omega_z$. A high NA (NA$= 0.62$) microscope above the final vacuum cell allows us to project either a sharp ring potential or arbitrary potential landscapes from two independent digital mirror devices (DMDs) into the 2D plane. In this thesis, only the ring is used for the vast majority of the results presented in Parts II to IV.

To image the atoms, a second, identical microscope below the sample is used, allowing us to image density and momentum distributions with a resolution of $\sim 1.5\,\mu$m via spin-resolved absorption imaging. The momentum distribution is accessed via time-of-flight expansion

(more details in Ch. 4.3.2), which fulfills two major goals: First, the temperature can be extracted from the thermal wings of the bimodal momentum distribution, and secondly, the low momentum peak is directly connected to the superfluid density, acting as a probe for the response in spectroscopic measurements.

4.2 Preparing an ultracold 2D Fermi gas

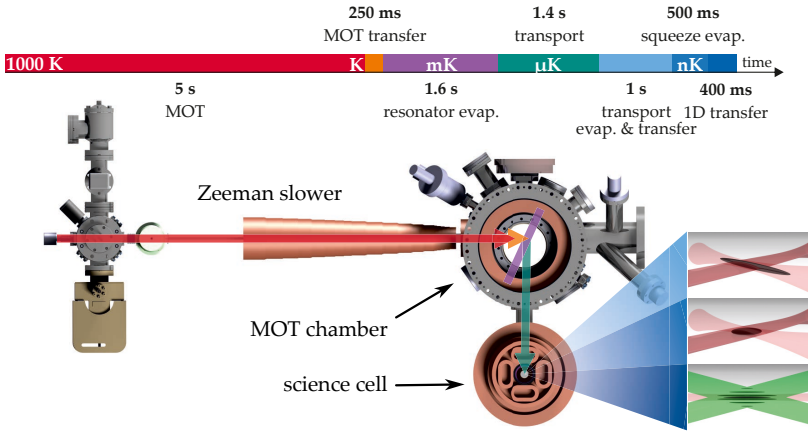


Figure 4.1: Overview of the experimental cycle and vacuum system. The oven provides an influx of ^{6}Li atoms, which are then cooled in the Zeeman slower (red) before being trapped in the MOT. Here, they are loaded into an optical resonator (purple) and prepared for the transport to the science cell by evaporatively cooling the gas. The transport trap (green) then moves the atoms to the science cell, where they are first loaded into an oblate trap and further evaporatively cooled (bright blue). From here, they are loaded into the purely repulsive homogeneous box, where a final evaporation occurs, leaving an ultracold 2D Fermi gas well below T_{BKT} (dark blue). Adapted from [74].

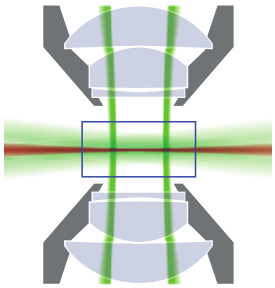


Figure 4.2: Front view of the dipole traps in the science cell. The repulsive box trap (green) is created by the ring, which is projected through the microscope, while the accordion trap is created by overlapping two beams at a variable angle from the side. An attractive oblate dipole trap (red) precompresses the atoms, ensuring that only a single layer is loaded in the accordion trap. Adapted from [75].

We will now focus on the different experimental steps required to create an ultracold 2D Fermi gas. An overview of the full experimental cycle and the vacuum system is shown in Fig. 4.1. In short, hot ^{6}Li atoms are released from an oven and cooled in a Zeeman slower (ZS, red), so they can be caught in a magneto-optical trap (MOT). Afterward, the atoms are loaded into a dipole trap provided by an optical resonator (purple), where they are further evaporatively cooled. From here, the atoms are loaded into the transport trap (green), which moves them from the MOT chamber to the science cell. There, they are first transferred into an oblate attractive dipole trap where they are evaporatively cooled to degeneracy, and then transferred to the homogeneous box potential. This box trap consists of two repulsive potentials (see Fig. 4.2): A radially confining ring and an accordion lattice that compresses the atoms into a 2D geometry. The atoms can be further cooled by lowering the ring power, leaving a clean 2D Fermi gas at $T < 0.02T_{\mathrm{F}}$. Optionally, before this evaporation, we can induce a spin imbalance, allowing us to probe imbalanced 2D Fermi gases below T_{BKT} (more details in Part IV). Alternatively to the ring, arbitrary potentials can be projected into the 2D plane by using a digital micromirror device (DMD).

After preparation, the ultracold 2D Fermi gas can be probed using various spectroscopic methods, which will be introduced in Ch. 4.3. Using absorption imaging, we can acquire in situ density images or extract the momentum distribution after a short time-of-flight (ToF). Since this procedure is destructive, we have to prepare a new sample for each shot. It is therefore beneficial to keep the cycle times as short

as possible, as it limits the amount of data we can take in a given amount of time.

We will now go into detail through the different preparation steps.

4.2.1 Oven and lasercooling: From 750 K to 140 µK

We start by evaporating Li in an oven at 480 °C, providing a constant stream of atoms to the experiment. In the first step, these atoms are slowed in a Zeeman slower (ZS) and then captured by a 3D magneto-optical trap (MOT) in the MOT chamber. The magnetic field of the ZS decreases along the path of the atoms to keep the light on resonance while the atoms slow down from velocities of roughly 1500 m/s to 1 m/s. In the MOT, we are able to reach temperatures close to the Doppler limit of 140 µK.

Both the ZS and MOT are fed by the same laser and address the D2 line of ^{6}Li (see Fig. 4.3) at a wavelength of $\lambda = 671$ nm to achieve cooling and trapping. A set of coils in an anti-Helmholtz configuration provides the magnetic field required to operate the MOT. To keep the laser at the required wavelengths, we use an offset lock to a reference laser, which in turn is locked to a ^{6}Li vapor cell via modulation transfer spectroscopy.

During this thesis, the laser system supplying light to the ZS and MOT was upgraded to eliminate redundant setups, replace degrading components, and deliver higher power to achieve faster MOT loading rates, since this step alone accounts for about one-third of the entire experimental cycle. We reduced the loading time from 5.5 to 3 s, while achieving three times as many atoms in the MOT. A summary of the upgrade is provided in Ch. 4.4.3 with more information in [76].

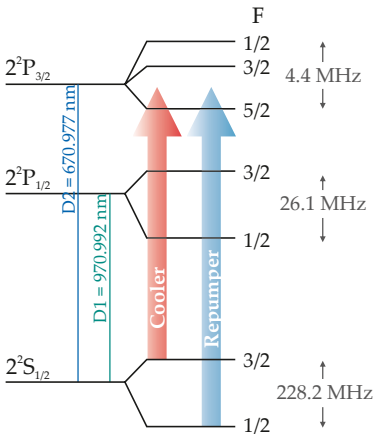


Figure 4.3: Level scheme of ^{6}Li including the transitions that are used for the MOT. The cooler and repumper are displayed as red and cyan arrows, respectively. Since the splitting between the hyperfine levels of $2^2P_{3/2}$ is very small, the cooler and repumper address all. Adapted from [74].

4.2.2 The cooling resonator: From 140 µK to 100 nK

In the next step, we transfer the atoms from the MOT to the first dipole trap that is far detuned at $\lambda = 1064$ nm. The main benefit of using a far-detuned potential is that scattering events with the light are negligible, with the downside that higher powers are required to trap the atoms. Since the atoms are still relatively hot ~ 140 µK, and spread over a large volume compared to the dipole trap, high intensities are required for loading.

Instead of using a high-power laser at e.g. 200 W, we use an optical resonator in vacuum that amplifies the intensities by a factor of ~ 1000. This allows us to achieve sufficient trapping using only 2 W of incoming light. We load the atoms about 3 cm off-center between two curved mirrors to ensure a larger overlap with the MOT[10] (see Fig. 4.4a). Since the resonator is a bowtie cavity, we inject two independent counterpropagating beams that create a standing-wave lattice for trapping. By slightly detuning one arm with respect to the other, the lattice moves, transporting the atoms to the center of the cavity (Fig. 4.4b), where one arm is switched off, and the atoms are

[10] When loading the MOT, it is actually not overlapped with the resonator. Only at the end of loading do we shift the center of the magnetic field using two additional sets of coils to align the MOT with the resonator. This increases the final atom numbers as the resonator initially does not disturb the MOT.

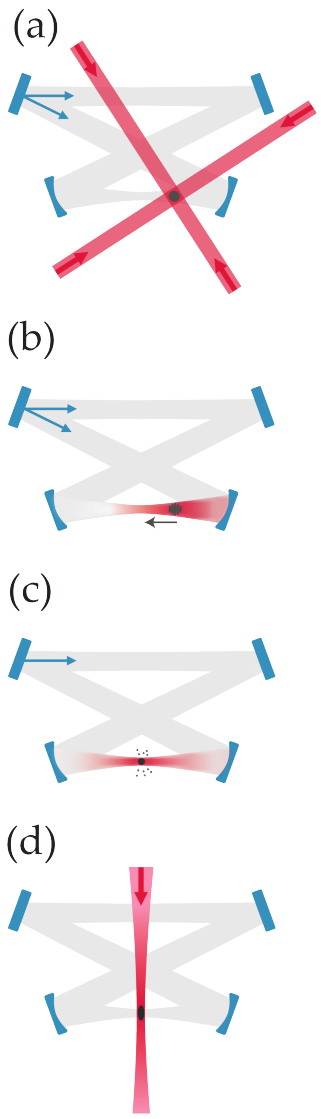


Figure 4.4: Resonator trapping and cooling scheme. a) Atoms are loaded from the MOT into the standing wave lattice of the bowtie cavity off-center. b) One of the resonator arms is detuned, transporting the atoms to the center of the cavity inside the moving lattice. c) After switching the coils to a Helmholtz configuration to increase interactions and turning off one of the arms, evaporative cooling is performed by lowering the power. d) After evaporation, the atoms are loaded into the transport trap. Adapted from [77].

evaporatively cooled (Fig. 4.4c). For efficient evaporation, we enhance interactions by exploiting the Feshbach resonance by switching the MOT coils to a Helmholtz configuration, thereby generating a homogeneous magnetic field. After cooling, the atoms are ready to be transported to the science cell.

4.2.3 Transport: From MOT chamber to science cell

As soon as the atoms become cold enough during resonator evaporation, they automatically move into the transport trap, which is overlaid on the resonator center (Fig. 4.4d). Like the resonator, this far-off-resonance trap (FORT) has an attractive wavelength of $\lambda = 1064\,\mathrm{nm}$ and is initially operated at 8 W. A movable lens on an air-bearing stage then transfers the atoms to the science cell within 1.4 s. After transport, the atoms arrive with an imbalance in the two lowest hyperfine states, with 80 % in the $|1\rangle$ state. We therefore use a series of about 100 Landau-Zener sweeps between $|1\rangle$ and $|2\rangle$ to balance the system before continuing. Finally, the atoms are further cooled so they are ready to be loaded into the 2D box potential. Similar to the MOT chamber, we have coils in place to control the interactions, which we set slightly above the pole of the Feshbach resonance at 870 G for efficient evaporation.

During this thesis, the laser system of the FORT was upgraded to enable higher power and therefore load more atoms more robustly from the resonator, as discussed in Ch. 4.4.2. Additionally, the photodiode used for the position stabilization was exchanged during the upgrade of the 2D breadboard, which is explained in Ch. 4.4.1. In particular, the stable atom numbers gained from the laser upgrade allowed us to reach the 2D regime for imbalanced Fermi gases, as presented in Part IV.

4.2.4 Loading the 2D homogeneous box: From 3D to 2D

Before loading the atoms into the final box potential, an attractive dipole trap (squeeze trap), again at $\lambda = 1064\,\mathrm{nm}$, is used to precompress the atoms vertically. This happens as the power of the FORT is ramped to 0 mW, while the squeeze trap stays at 1 W.

Subsequently, the atoms are further evaporatively cooled in the squeeze trap while the magnetic field is ramped to 750 G, well below the Feshbach resonance. This transfers the atoms into tightly bound bosonic molecules and later improves loading into the box potential due to the low chemical potential in the BEC regime. Before that, however, a magnetic field gradient deterministically spills the gas to a desired number of atoms, with the final atom numbers fluctuating less than 5 % in between experimental cycles.

Now, the atoms are transferred to the repulsive box potential used for the main experiment. The repulsive dipole traps for the 2D homogeneous box are switched on, consisting of the ring and accordion,

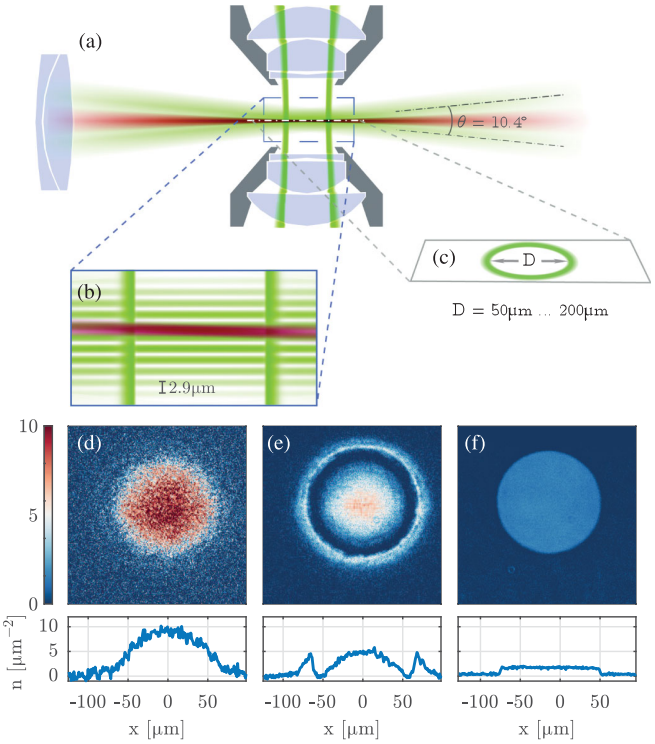


Figure 4.5: 2D box trap in the experiment. a) General overview. Atoms are loaded from the attractive squeeze trap (red) into the repulsive box trap (green). b) The squeeze trap precompresses the atoms for reliable loading of a single layer of the accordion lattice. By changing the angle θ, the lattice spacing can be adjusted. c) The ring, which is projected through the upper microscope, provides radial confinement in a homogeneous box with a diameter of typically 80 μm. d)-f) Density profiles for atoms in the squeeze trap (a), squeeze + ring (b), and ring + accordion (c). Adapted from [75].

both at $\lambda = 532\,\mathrm{nm}$. The ring[11] is projected through a high-NA microscope above the glass cell and radially confines the atoms to a diameter of $\sim 90\,\mu\mathrm{m}$. For the 2D confinement, we employ a vertical accordion lattice, which is created by overlapping two beams from the side at an angle which can be continuously tuned between 1.5° and 13°, leading to trapping frequencies ranging from $\omega_z = 2\pi \cdot 0.8\,\mathrm{kHz}$ up to $2\pi \cdot 11.5\,\mathrm{kHz}$, respectively. After loading atoms into the open accordion, it is compressed to $\omega_z \approx 2\pi \cdot 12\,\mathrm{kHz}$, leaving a superfluid in the 2D regime.

To achieve our final temperatures, a final evaporation is performed by lowering the ring power. The cooling is aided by using a slight anticonfinement that pushes the evaporated atoms away from the ring. This anticonfinement is generated by the accordion trap and is usually canceled out by the confinement of the magnetic field that is used to tune the interactions. However, a second pair of coils in a Helmholtz configuration can create a much more homogeneous magnetic field, leaving the anticonfinement of the accordion trap in place. Therefore, during evaporation, the hot atoms outside the ring are actively pushed away, leaving a clean superfluid at temperatures[12] $\widetilde{T}/T_F \leq 0.02$ for balanced systems. After this evaporation, we switch back to the first set of coils and ramp the magnetic field to reach the desired interactions for the main experiments. The system can then be imaged via absorption imaging.

During the course of this thesis, the 2D breadboard, which, among other things, features the squeeze trap and accordion lattice, was completely renewed. Previously, the vertical lattice for 2D confinement

[11] The ring beam itself is created by an optical setup making use of multiple axicons, allowing a sharp ring at high powers to be projected into the gas. A detailed description of the axicon setup can be found in [78].

[12] More details on the temperature measurements are provided in Ch. 4.3.2.

was static, whereas now we are able to tune the lattice spacing from 20 to 2.3 µm, leading to trap frequencies between 0.8 and 11.5 kHz, respectively, at maximum power (0.5 W). The upgrade of the 2D breadboard is summarized in Ch. 4.4.1 while a more detailed description can be found in [79]. As an alternative to the ring, there are two separate digital mirror devices (DMDs) that allow arbitrary potentials to be projected onto the 2D plane.

4.3 Probing 2D Fermi gases

Parts of this section were adapted from the supplementary material of [19], submitted during the course of this work. Notably, Ch. 4.3.2 was taken from the experimental documentation with minor modifications, and Ch. 4.3.3 and 4.3.4 closely follow the discussion of the theoretical description of the spectroscopic techniques.

4.3.1 Density imaging

To take in situ density images, we use high-power absorption imaging. The light that is used is resonant with the D2 line of ^{6}Li, and since we take the images at fields between 700 and 1000 G, the splitting between the hyperfine levels is large enough that we can address them individually. Since ^{6}Li is very light, we use high powers for imaging so that a single shot only illuminates the atoms for 5 µs, eliminating movement-related blur. Because of these high powers, we have to consider saturation-related effects, which are calibrated using a technique similar to that presented in [80], and are described in detail in [77]. Furthermore, during imaging, the atoms are already accelerating, so we sweep the imaging light frequency to stay on resonance.

A microscope below the vacuum cell with an additional lens setup then projects the image of the 2D plane onto an EMCCD (electron-multiplying charge-coupled device) camera with a resolution[13] of around 1.5 µm. This camera features a "fast kinetics" mode that can also be used to take multiple pictures of smaller vertical size in quick succession, which allowed us to implement a double-shot technique where both spin states used in the experiment are imaged in a single experimental cycle (see Appendix A). However, since this technique was only reliably implemented towards the end of this work, it was not used for any of the results presented in this thesis.

[13] The best resolution theoretically achievable in the experiment is 0.7 µm, since the microscope has a numerical aperture of 0.62 and we use a wavelength of 671 nm for imaging. However, due to slight misalignments, we currently do not reach that value.

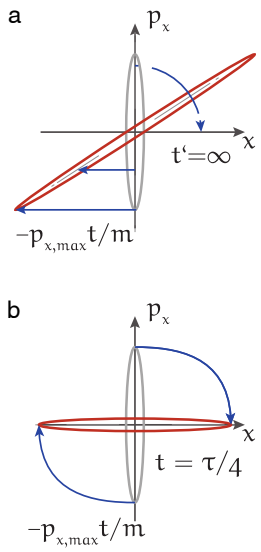


Figure 4.6: Free-space vs. T/4 ToF. a) In free space, the cloud gets sheared in phase space as time progresses. b) In a weak harmonic confinement, the phase space instead rotates along 90° after a quarter of a period, mapping momentum to real space. Adapted from [78].

4.3.2 Measuring temperature and response from the momentum distribution

Accessing the momentum distribution is vital for all experiments conducted in this thesis, as it allows us to extract a response from spectroscopic measurements and measure the temperature. We achieve this by using $T/4$ time-of-flight (ToF), where we switch off all optical trapping potentials and exploit the residual radial confinement of

28 Hz from the magnetic field. A detailed explanation of this technique can be found in [75], but in short, after a quarter of a period $T/4 = 9\,\text{ms}$, the momentum space maps to real space (see Fig. 4.6) and can be imaged via standard absorption imaging as explained in the previous section.

However, because the superfluid is strongly confined along the imaging axis prior to switch-off, the cloud rapidly expands beyond the microscope's depth of field, distorting the momentum distribution. We resolve this issue by slightly tilting the imaging beam (see Fig. 4.7a) such that the z-axis is partially mapped to the y-axis of the density images, resulting in the elongated shape shown in Fig. 4.7b. The center, as indicated by the dashed lines, corresponds to the atoms in focus, showing the actual momentum distribution, while the atoms further above and below are out of focus.

Since we are interested in measuring the temperature and condensate density, we ramp the magnetic field to low interactions in the bosonic regime at $B = 750\,\text{G}$ for all measurements involving $T/4$ ToF, where $\ln(k_F a_{2D}) \approx -2.5$. This reduces collision events that may distort the momentum distribution and freeze out the dynamics. Additionally, the atoms are tightly bound in bosonic molecules, which, for low enough temperatures, leads to a clear bimodal structure (see Fig. 4.7c), where the condensed atoms are in the parabolic low-momentum peak, and the thermal fraction is visible in the much broader wings.

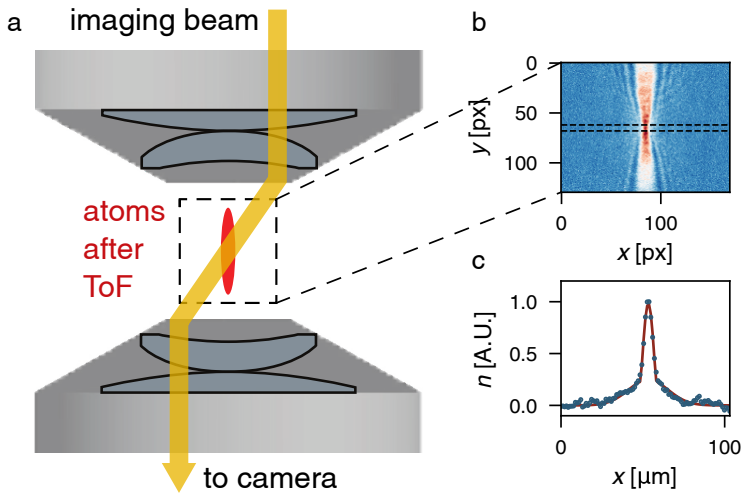


Figure 4.7: Tilted imaging. a) Sketch of tilted imaging. After ToF expansion, the atoms expand vertically due to prior confinement. We perform absorption imaging with a tilted beam to avoid artifacts from out-of-focus atoms. We can therefore extract the response and temperature from a small in-focus region in the images. b) An average of 50 absorption images taken with a tilted imaging beam. The central region indicated by the dashed lines shows no diffraction fringes. The atoms above and below this region are out of focus. c) Momentum distribution obtained from the vertical sum of the region between the dashed lines in b. The red line is a bimodal fit used to extract the temperature.

To extract the temperature, we typically average over 50 density images, take a vertical sum, and fit a bimodal function to the measured distribution (see Fig. 4.7c). The bimodal fit combines a parabolic term for the condensate and a Boltzmann distribution, with the temperature given by the thermal wings.

If we want to extract a response from our different spectroscopic techniques, we instead use the condensate peak as it provides a much better signal-to-noise ratio. Again, we take a horizontal slice through

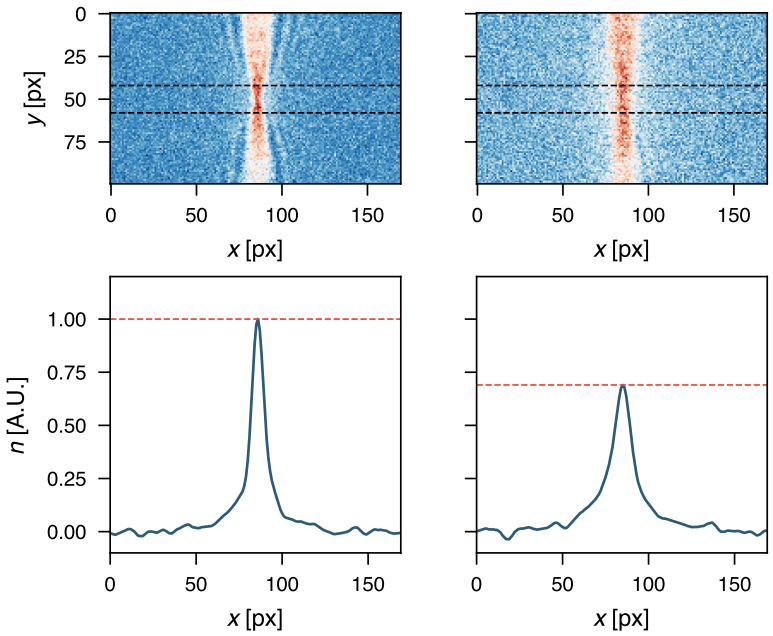


Figure 4.8: Density images after a 9 ms T/4-ToF expansion for a system before (left) and after (right) resonant modulation. The imaging is slightly tilted to avoid fringes caused by atoms that have expanded out of focus as they enter the central region. The smoothed horizontal slices from the sum between the black dashed lines are shown in the lower panels. A clear condensate peak is visible for both slices, but with different maximum values (red dashed lines). Adapted from [19].

the center of the time-of-flight images, but this time we smooth the distributions for better stability. Comparing the peak densities of the low momentum peaks of the unperturbed system $C(0)$ with the driven system $C(\omega_\mathrm{m})$ then allows us to extract the response [6]:

$$R(\omega_\mathrm{m}) = 1 - \frac{C(\omega_\mathrm{m})}{C(0)}. \tag{4.1}$$

4.3.3 Bragg spectroscopy

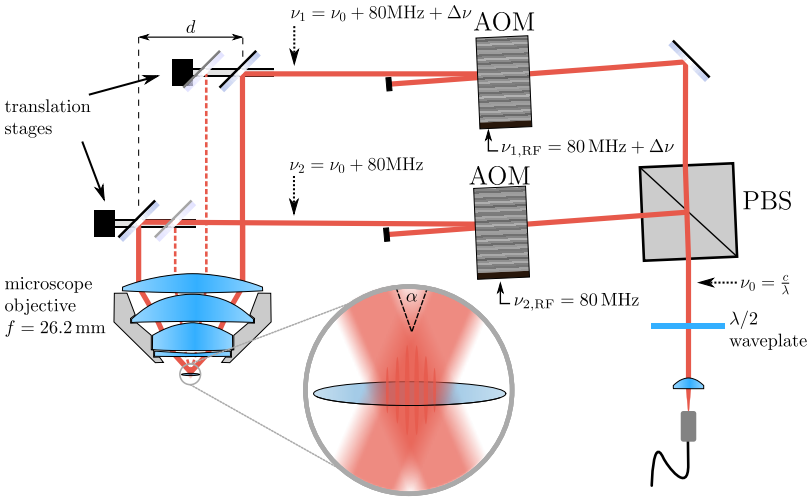


Figure 4.9: Sketch of the Bragg spectroscopy setup. The beams are split in two via a PBS to ensure equal powers in both arms. Each arm then has its own AOM and translation change to independently adjust the wavelength and angle, respectively. The moving lattice is then created by focusing both beams into the sample via the upper microscope objective. Adapted from [59].

We probe the momentum-resolved spectrum experimentally using Bragg spectroscopy. The implementation is discussed in detail in [59],

and I will provide a short summary here while also showing how this technique is connected to the spectral function, as explained in the supplementary material of [19].

The basic idea is to probe the system at a specific energy $\hbar\omega_m$ and momentum q by using a two-photon process. Experimentally, this is achieved by splitting a far-off-resonant beam at a wavelength of 780 nm into two independent arms, each of which passes through an acousto-optic modulator (AOM) and is overlapped onto the atoms at a controllable angle (see Fig. 4.9). This angle can be changed by moving two linear translation stages and focusing the translated arms into the 2D plane through the upper microscope. By coherently absorbing a photon of one beam and reemitting it into the other, the system gains an energy $\hbar\omega = \hbar(\omega_1 - \omega_2)$, set by the detuning between the two AOMs, and an in-plane momentum $q = k_1 - k_2$. An alternative perspective to understand Bragg spectroscopy is that the overlapping beams create a running optical lattice in the 2D plane, where the lattice spacing determines the momentum and the speed sets the energy at which the gas is probed.

We can see that Bragg spectroscopy only couples to the density-density correlation function, since it introduces a dynamic potential

$$\hat{V}_\Omega(t) = \Omega \int d^3r\, 2\cos(\mathbf{q}\cdot\mathbf{r}_\perp - \omega t)\, \underbrace{\hat{\psi}^\dagger(\mathbf{r})\hat{\psi}(\mathbf{r})}_{\hat{n}(\mathbf{r})}\,, \tag{4.2}$$

where Ω denotes the intensity of the applied field and $\hat{\psi}^\dagger(\mathbf{r})$ creates a particle at $\mathbf{r}$. For a more intuitive understanding, we switch to second quantization, also including the harmonic oscillator wavefunctions[14] of the strong confinement $\varphi_n(z)$, via the transformations

[14] For convenience, we drop the subscript z of n_z for the indices n.

$$\hat{c}_{\mathbf{k}n} = \int d^3r\, e^{-i\mathbf{k}.\mathbf{r}_\perp}\varphi_n^*(z)\hat{\psi}(\mathbf{r}) \tag{4.3}$$

$$\hat{\psi}(\mathbf{r}) = \sum_{\mathbf{k},n} e^{i\mathbf{k}.\mathbf{r}_\perp}\varphi_n(z)\hat{c}_{\mathbf{k}n}\,. \tag{4.4}$$

In the scenario where all atoms are in the ground state $n_z = 0$ of the confinement, we get the driving term

$$\hat{V}_\Omega(t) = \Omega\sum_{\mathbf{k}}\left(e^{-i\omega t}\hat{c}^\dagger_{\mathbf{k}+\mathbf{q},0}\hat{c}_{\mathbf{k}0} + e^{i\omega t}\hat{c}^\dagger_{\mathbf{k}0}\hat{c}_{\mathbf{k}+\mathbf{q},0}\right)\,. \tag{4.5}$$

Therefore, Bragg spectroscopy addresses excitations at a specific momentum $\mathbf{q}$.

We can then calculate the rate at which momentum is transferred to the system

$$i\frac{d\,\langle\hat{P}\rangle}{dt} = \langle\psi|\,U^\dagger(t)[\hat{P},\hat{V}_\Omega(t)]U(t)\,|\psi\rangle\,, \tag{4.6}$$

with the time evolution operators $U^\dagger(t)$, giving [19]

$$\frac{d\mathbf{P}}{dt} \propto n\mathbf{q}A_0(\mathbf{q},\omega)\,, \tag{4.7}$$

where $A_0(\mathbf{q},\omega)$ is the spectral function for in-plane excitations, including the Goldstone mode and the pair-breaking continuum. $A_0(\mathbf{q},\omega)$ is also called the dynamic structure factor [47, 59].

Additionally, we can also access confinement-induced excitations discussed in Ch. 3.4.4 by slightly tilting the Bragg beams (e.g., by offsetting the linear translation stages in the experiment). In this case, the dynamic potential changes to

$$\hat{V}_\Omega(t) = \Omega \int d^3r\, 2\cos(\mathbf{q}\cdot\mathbf{r}_\perp + q_z z - \omega t)\, \hat{\psi}^\dagger(\mathbf{r})\hat{\psi}(\mathbf{r})\,, \tag{4.8}$$

with the transverse momentum component q_z. In second quantization, Eq. (4.8) becomes

$$\hat{V}_\Omega(t) = \Omega \sum_{\mathbf{k},n,m} \left(e^{-i\omega t} Q_{nm}\, \hat{c}^\dagger_{\mathbf{k}+\mathbf{q},m}\hat{c}_{\mathbf{k}n} + e^{i\omega t} Q^*_{nm}\, \hat{c}^\dagger_{\mathbf{k}n}\hat{c}_{\mathbf{k}+\mathbf{q},m} \right). \tag{4.9}$$

Here, Q_{nm} quantifies the coupling strength to the higher levels. Since we always start from the ground state, the relation

$$\sum_n |Q_{n0}|^2 = 1 \tag{4.10}$$

holds. Considering only the lowest three levels, we get

$$\begin{aligned} |Q_{00}|^2 &= \left(1 - \frac{q_z^2 l_z^2}{4}\right)^2 \\ |Q_{10}|^2 &= \frac{q_z^2 l_z^2}{2} \\ |Q_{20}|^2 &= \frac{q_z^4 l_z^4}{8}\,. \end{aligned} \tag{4.11}$$

We can see that, as long as the Bragg lattice has no transverse momentum component q_z, it does not couple to higher levels.

Again, we calculate the rate at which momentum is transferred to the system, arriving at

$$\frac{d\mathbf{P}}{dt} \propto n_0 \mathbf{q} |Q_{n0}|^2 A_n(\mathbf{q},\omega)\,. \tag{4.12}$$

Therefore, we can access the spectral functions $A_n(\mathbf{q},\omega)$ of each individual harmonic oscillator level n_z.

4.3.4 Trap-modulation spectroscopy

The second important spectroscopic method in our experiment is trap-modulation spectroscopy. Here, we periodically modulate the power of the strongly confining lattice, as illustrated in Fig. 4.10, allowing us to probe excitations exactly at a momentum transfer of $q = 0$. Since the lower limit for q in our Bragg spectroscopy setup is restricted due to the finite size of the Beams, it is perfectly suited to probe $A_2(0,\omega)$, as we will see in the following.

We modulate the power of the lattice sinusoidally, leading to the dynamic potential

$$\hat{V}_\Omega(t) = 2\Omega \sin(\omega t) \int d^3r\, z^2\, \hat{\psi}^\dagger(\mathbf{r})\hat{\psi}(\mathbf{r})\,. \tag{4.13}$$

Again, switching to second quantization, we get

$$\hat{V}_\Omega(t) = 2\Omega \sin(\omega t) \sum_{\substack{n, \\ m \geq n}} W_{nm} \left(\hat{c}^\dagger_{\mathbf{k}m} \hat{c}_{\mathbf{k}n} + h.c. \right) , \tag{4.14}$$

with the coefficients

$$\begin{aligned} W_{nm} &\equiv \int_{-\infty}^{\infty} dz\, \varphi_n^*(z) z^2 \varphi_m(z) \\ &= \begin{cases} \frac{2n+1}{2} l_z^2 , & m = n \\ \frac{\sqrt{(n+1)(n+2)}}{2} l_z^2 , & m = n+2 , \\ 0 & \text{otherwise} \end{cases} \end{aligned} \tag{4.15}$$

Since trap-modulation spectroscopy is a symmetric procedure, it can only excite even transitions. Here, we consider only excitations from level n to $m = n+2$; however, higher even transitions, e.g., $m = n+4$, are also possible, albeit more suppressed.

We can now calculate the energy deposited in the system via

$$i \frac{d \langle \hat{H} \rangle}{dt} = \langle \psi | U^\dagger(t) [\hat{H}, \hat{V}_\Omega(t)] U(t) | \psi \rangle \ . \tag{4.16}$$

If, again, only the $n_z = 0$ state is occupied at the beginning, after some algebra we get [19]

$$\frac{dE}{dt} \propto n_0 \, A_2(\omega) , \tag{4.17}$$

allowing us to probe the spectral function of the second excited state $A_2(\omega)$.

Furthermore, by modulating the trap frequency ω_z, the harmonic oscillator length $l_z = \sqrt{\hbar/(m\omega_z)}$ is also modulated. Since l_z also determines the 2D scattering length a_{2D} (see Eq. (3.93) in Ch. 3.4.3), trap modulation spectroscopy also couples to the amplitude mode, as we will see in Part II.

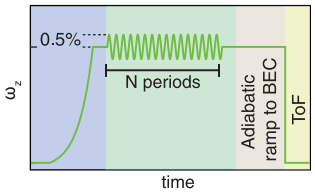


Figure 4.10: Sketch of trap modulation spectroscopy. The trap frequency ω_z is weakly modulated, after which the system is ramped to the BEC regime to allow for the extraction of the response via ToF expansion. Adapted from [10].

4.4 Upgrades over the course of this work

Three major upgrades have been implemented over the course of this work, starting with the breadboard, which provides the accordion lattice, the squeeze trap, and horizontal imaging along 4 different directions. The second upgrade increased the power of the transport trap, allowing us to transport atoms to the science cell more reliably and thereby increasing the total number of atoms in the final experiment. Finally, the laser-cooling setup for the MOT and the Zeeman slower was streamlined to achieve higher intensities and faster load times while eliminating multiple degrading components in the experiment. I will summarize these upgrades in the following sections.

4.4.1 New 2D breadboard and coils

At the beginning of this work, the 2D breadboard, including the coils for the science cell, was fully replaced. The new coils improved

two things: First, they are closer to the glass cell and therefore smaller, allowing more space for the optics on the new breadboard, providing greater flexibility. Second, the coil holder was designed to accommodate magnetic field jumps by featuring a slit on one side, eliminating eddy currents that limit the rate at which the field can change. Unfortunately, in tests we observed that higher-order eddy currents can still introduce a kick to the atoms during a field jump, as discussed in [79]. This kick can be compensated via four pairs of clover leaf coils; however, since none of the presented works in this thesis use field jumps, this feature is not further discussed here.

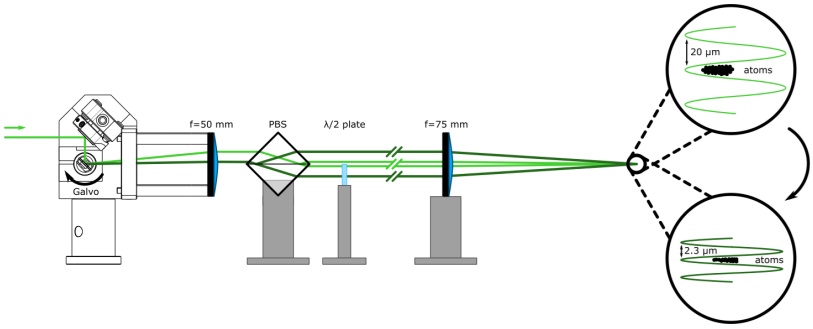


Figure 4.11: Setup of the accordion lattice. A beam with a wavelength of 532 nm is focused onto a galvo, which can be set to reflect the beam at a specific angle. This angle is then converted to an offset by another lens. The beam is split by a rotated PBS, and a last lens focuses the beams onto the atoms. This creates a vertical lattice with variable spacing. Adapted from [79].

The breadboard itself introduced multiple improvements, most notably the accordion lattice, which allows the lattice spacing to be changed from 20 to 2.3 µm. A sketch of the setup is shown in Fig. 4.11: A beam with a repulsive wavelength $\lambda = 532\,\text{nm}$ is focused onto a galvo mirror, which sets the angle of the reflected beam. A second lens, placed a focal length behind the galvo mirror, then converts the angle into a vertical displacement. The beam is then split via a 45° rotated polarizing beam splitter (PBS), with the distance between the beams given by the position of the incoming beam. A $\lambda/2$ plate then rotates the polarization of the lower beam to match that of the upper beam, before a lens focuses the beams onto the atoms, creating a vertical lattice via interference. The lattice spacing ultimately depends on the distance of the outgoing beams from the PBS.

This upgrade was developed by Markus Bohlen and Jonas Faltinath, and implemented jointly with Niclas Luick, Hauke Biss, Jonas Faltinath, and myself. For more details on the new 2D breadboard, see [79].

4.4.2 Stabilizing the transport

Another implemented upgrade is the new laser for the transport trap. Initially, the attractive light at $\lambda = 1064\,\text{nm}$ was provided via a reject port of a $\lambda = 532\,\text{nm}$ laser and was able to provide 30 W, although at a poor beam quality. Before exchange, the maximum power in the trap itself was 6 W, allowing to safely transport $\sim 1 \times 10^6$ atoms.

This laser was replaced with a $\lambda = 1070\,\text{nm}$ laser, allowing us to reach trap powers up to 8 W, even though the output power used

is 20 W. This led to a factor of 2 increase in the number of atoms in the science cell. Since the laser can reach an output power of 200 W, a future upgrade using only free-space optics could completely eliminate the optical resonator, which is generally prone to failure.

4.4.3 Streamlining laser cooling

The last upgrade was a complete redesign of the laser system used for laser cooling, jointly developed and implemented by Jannis Dammann, Moritz von Usslar, and myself.

Previously, the Zeeman slower and MOT were completely independent systems, each featuring a $\lambda = 671\,\text{nm}$ laser and tapered amplifier (TA). Since the laser diodes and the TAs degrade over time, they had to be replaced at regular intervals.

To eliminate these degrading components from the experiment, everything was replaced with a fiber laser that uses two infrared sources and sum frequency generation to create 671 nm light with an output power of up to 5 W, a factor of ~ 5 higher than what the previous setup could provide. The new setup is shown in Fig. 4.12. Since the Zeeman slower and the center frequency of the MOT are only $\sim 160\,\text{MHz}$ apart, the laser can serve both setups by using a double-pass AOM setup to bridge the frequency difference.

After implementation, we reduced the MOT loading times from 5.5 to 3 s, with roughly three times as many atoms inside the MOT by the end of loading.

More details about the setup can be found in [76].

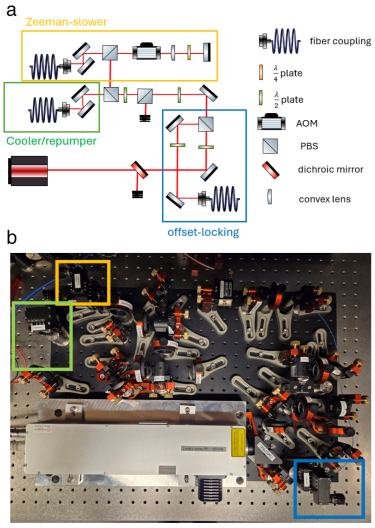


Figure 4.12: a) Sketch of the new laser system in the experiment. b) Picture of the new laser system after implementation. Adapted from [76].

Part II

Dynamics under strong confinement

5 HYBRIDIZATION OF THE AMPLITUDE MODE IN A CONFINED FERMIONIC SUPERFLUID

In this chapter, we report on the hybridization of the amplitude mode of a superfluid with a confinement-induced mode, which is published in

> *C. R. Cabrera, R. Henke, L. Broers, J. Skulte, H. P. Ojeda Collado, H. Biss, L. Mathey and H. Moritz, Physical Review Research* **7** *(3), L032018 (2025)* [10]

and reprinted here with minor modifications. The conception and conduction of all measurements presented here were jointly performed by Cesar Cabrera, Hauke Biss and me. The theoretical description was developed by Lukas Broers, Jim Skulte and Hector Pablo Ojeda Collado. The entire work was supervised by Cesar Cabrera, Ludwig Mathey and Henning Moritz.

Bardeen-Cooper-Schrieffer (BCS) theory [1] provides the framework for understanding superconductivity. It describes the formation of Cooper pairs and the emergence of a superconducting energy gap, 2Δ, corresponding to the minimum energy required to break them (see Ch. 3.2). However, as P. Anderson noted, significant deviations from this framework can occur in finite-size systems when the characteristic length or energy scale imposed by the confinement approaches the Cooper-pair size or the pairing gap energy, respectively [81]. These finite-size effects have been predicted and observed in systems such as nanowires and thin films [70–72], where confinement can modify the dimensionality, enhance the superfluid gap, or increase the critical temperature (T_c), see review [82]. Such phenomena highlight how confinement can be used to engineer superconducting properties.

A key open question we address in this work is how confinement influences the fundamental collective modes of fermionic superfluids and superconductors. As introduced in Ch. 3.3.2, these systems are characterized by an order parameter, $\Psi = |\Psi|e^{-i\theta}$, supporting fluctuations in θ and $|\Psi|$, which correspond to the Goldstone mode (gapless phononic excitation) and the amplitude mode (gapped Higgs-like excitation at energy 2Δ), respectively [25, 60]. While these collective modes are well understood in homogeneous systems, their behavior in the presence of confinement remains largely unexplored. For instance, the excitation spectrum is expected to change qualitatively [83–86], featuring a hybridization of oscillations of the amplitude and the spatial distribution of the order parameter.

In previous work, evidence for amplitude oscillations of the order parameter has been reported in both superconductors [62, 67, 87, 88], as well as in ultracold bosonic and fermionic superfluids [58, 68, 89–92]. Additionally, a mesoscopic system has been used to explore precursors of the amplitude mode and its interplay with discrete energy shells [93]. In contrast to these experiments, we study

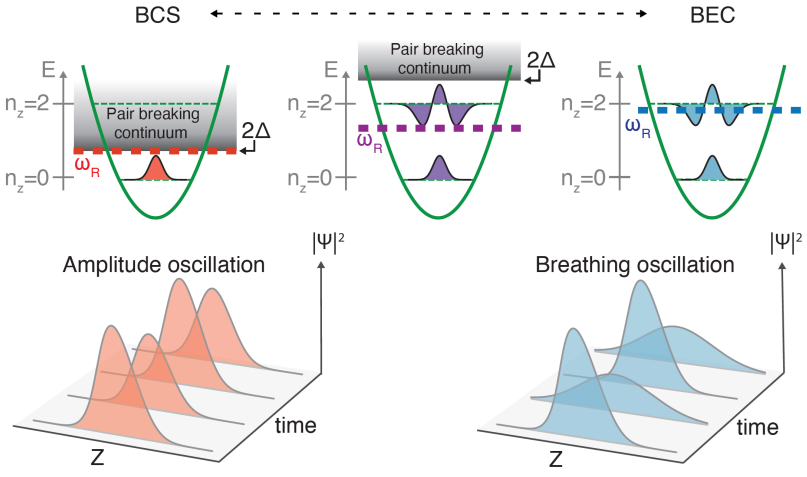


Figure 5.1: Hybridization of amplitude oscillations with spatial excitations. In our confined fermionic superfluid, a well-defined excitation of the order parameter with frequency ω_R is observed throughout the entire BEC-BCS crossover (dashed lines). In the BCS regime, this excitation corresponds to a pure amplitude oscillation of the order parameter located at the onset of the pair-breaking continuum 2Δ. This oscillation conserves the quantum number $n_z = 0$, but the superfluid density $n_s = \int |\Psi|^2 dz$ oscillates in amplitude, illustrated with red curves. In the BEC regime, the excitation at ω_R corresponds to a breathing mode with energy approaching $2\hbar\omega_z$, involving the quantum numbers $n_z = 0$ and $n_z = 2$. This oscillation is sketched with blue curves. In the strongly interacting regime, when Δ becomes comparable to $\hbar\omega_z$, the resulting excitation is a hybridized mode with both breathing and amplitude character. Here, the mode frequency drops below the pair-breaking continuum.

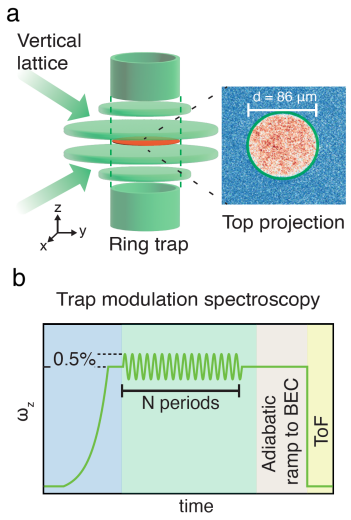


Figure 5.2: a) We prepare a homogeneous Fermi gas in a ring-shaped box potential, strongly confined along z with a repulsive lattice potential. The harmonic confinement is comparable to the Fermi energy E_F with $1.5 < E_F/\hbar\omega_z < 2$. b) The trapping frequency ω_z is weakly modulated to excite spatial oscillations of the order parameter and amplitude oscillations via the corresponding modulation of the interaction strength. The deposited heat is measured by performing ToF after an adiabatic ramp to the BEC regime.

the effect of confinement on the amplitude mode in a macroscopic fermionic superfluid and observe strong evidence of its hybridization with a collective mode of the trap. This is achieved by exploiting the BEC-BCS crossover to tune the pairing gap energy, bringing it close to the trap level spacing. The resulting hybridization is depicted in Fig. 5.1. In the BCS regime, the pairing gap energy is smaller than the trap level spacing. Here, the system exhibits a well-defined resonance with frequency ω_R located at 2Δ (Fig. 5.1, left panel), where the superfluid density $n_s = \int |\Psi|^2 dz$ oscillates in amplitude (red curves). Its frequency coincides with the onset of pair-breaking, however, it is a coherent excitation. Towards the strongly interacting regime, the pairing gap increases, and the amplitude mode hybridizes with the nearest spatial mode of the trap with equal parity, specifically the quantum number $n_z = 2$ (central panel). In this intermediate regime, the resonance energy ω_R drops below 2Δ, and the order parameter acquires a spatially oscillating component, admixing state $n_z = 2$ to the ground state $n_z = 0$. Finally, deep in the BEC regime, the resonance approaches twice the trap level spacing (right panel), resembling a pure breathing mode (blue curves). Our interpretation is based on an effective field theory, which continuously connects the Gross-Pitaevski and Klein-Gordon functionals [25, 94], showing remarkable agreement with our experimental results.

5.1 Engineering the hybridization in the BEC-BCS crossover

To engineer the mode hybridization, we prepare a homogeneous fermionic superfluid ($T^* < 0.02\,T_F$) of ^{6}Li atoms in the lowest two hyperfine states [75]. The system is subjected to strong vertical confinement $\hbar\omega_z = h \cdot 8.7\,\text{kHz}$ (Fig. 5.2a), comparable to the Fermi energy $E_F = \hbar^2 4\pi n_{2D}/2m$. Here, T_F is the Fermi temperature, T^* is the temperature measured after an adiabatic sweep into the BEC regime, m is the atom mass, $\hbar$ is the reduced Planck's constant, and n_{2D} is the fermionic density per spin state. To reach the regime where

the pairing energy is comparable to the vertical confinement energy, we tune the interaction parameter $\eta = \ln(k_F a_{2D})$ using a Feshbach resonance, where $k_F = \sqrt{4\pi n_{2D}}$ is the Fermi momentum and a_{2D} is the 2D scattering length [32, 38, 95]. To probe both spatial and amplitude oscillations of the order parameter, we vary the interaction strength [58, 68] by employing trap modulation spectroscopy [89, 90]. This modulates the harmonic oscillator length l_z and hence the scattering length a_{2D}.

Specifically, we modulate the trapping frequency with an amplitude $\alpha \leq 0.5\,\%$ at a frequency ω_m for a fixed number of periods, $N = 240$, followed by a rethermalization time of 20 ms. To obtain the deposited energy, we adiabatically ramp into the BEC regime ($\eta = -1.7$) and measure the bimodal momentum distribution after time-of-flight (ToF). Here, we extract the condensate amplitude $A(\omega_m)$. This is compared to the condensate amplitude of the unperturbed system $A(0)$, defining our response function $R(\omega_m) = A(0)/A(\omega_m) - 1$. This normalized function deviates from zero when energy is deposited in the system, revealing resonant frequencies.

In the first series of experiments, we start with a fermionic density of $n_{2D} \approx 1.5\,\text{atoms}/\mu\text{m}^2$, resulting in a ratio of $E_F/\hbar\omega_z = 1.8$. A typical response from trap modulation is shown in the inset of Fig. 5.3a. This measurement is extended throughout the entire BEC-BCS crossover in Fig. 5.3a, where the color encodes the response $R(\omega_m)$. The vertical axis is normalized to the trapping frequency ω_z, which is independently determined using a fermionic gas with negligible interactions. The system exhibits two distinct excitations. Within the BCS regime, one appears as a broad resonance located at $\omega_m \approx 2\omega_z$, corresponding to single-particle excitations of unpaired atoms to the energy level $n_z = 2$. The other manifests as a narrower resonance at lower frequency, gradually increasing from the BCS ($\eta = 3$) to the BEC ($\eta = -2$) regime, eventually approaching $2\omega_z$.

In the weakly interacting BCS regime, the well-defined resonance is located at nearly twice the pairing gap Δ. It agrees with the mean-field prediction of $\Delta = \sqrt{2E_b E_F}$ (red dotted line), where the binding energy E_b is calculated in the 2D limit. This agreement breaks down towards the strongly interacting regime for $\eta < 1.9$, where the observed mode deviates from the onset of the pair-breaking continuum, measured independently via Bragg spectroscopy (red points in Fig. 5.3a) [6, 8, 54, 56], and instead becomes an in-gap excitation. Finally, in the BEC regime, the order parameter is directly related to the total density and hence only supports spatial oscillations along the vertical confinement [25]. Here, the resonance corresponds to a breathing excitation of the condensate shifted downwards from $2\hbar\omega_z$ due to repulsive dimer-dimer interactions.

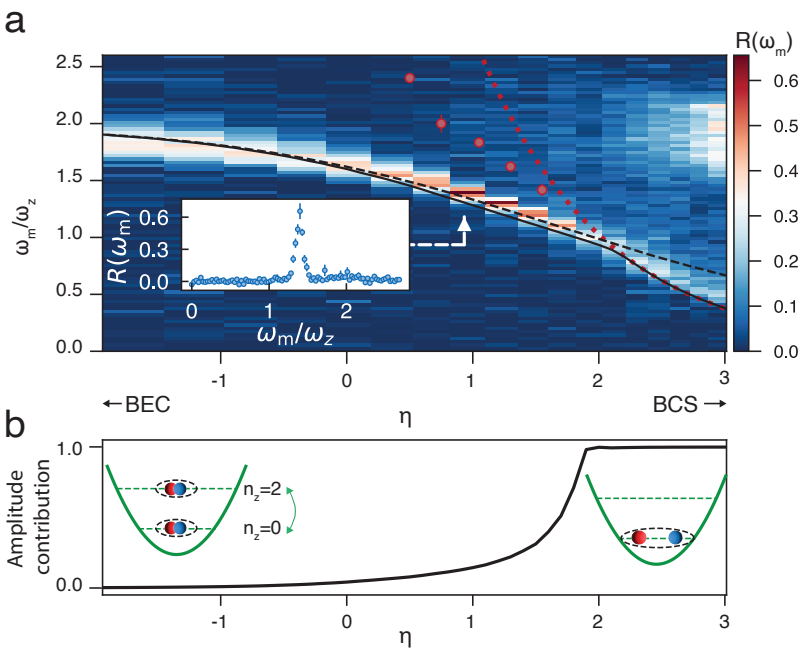


Figure 5.3: a) Spectral response $R(\omega_m)$ of a confined fermionic superfluid throughout the BEC-BCS crossover, measured via trap modulation spectroscopy. The inset shows a typical response $R(\omega_m)$ for $\eta = 0.97$, with a resonance located below the single-particle excitation energy $2\hbar\omega_z$. In the BCS limit ($\eta \gg 0$), the energy of the resonance agrees with the mean-field value 2Δ (red dotted line). At $\eta = 2$, it deviates from 2Δ, evolving into an in-gap excitation. This is supported by an experimental measurement of 2Δ using Bragg spectroscopy (red points). In the BEC regime ($\eta \ll 0$), where no amplitude mode exists, the excitation corresponds to a breathing mode along the confined direction. Here, its energy is in good agreement with an analytical calculation of the energy difference between the $n_z = 0$ and $n_z = 2$ eigenmodes (black dashed line) extracted from an effective field theory (see main text). The full numerical simulation shows excellent agreement in the entire crossover (black solid line). The error bars show the standard deviation of the mean. **b)** Hybridization of the amplitude mode. For values $\eta > 1.9$, the amplitude character is dominant, quantified by the amplitude contribution extracted from the effective field theory (black line). Here, the excitation does not conserve the total superfluid density, while conserving the quantum number $n_z = 0$. In the BEC regime, the superfluid density is conserved and oscillates spatially, involving the $n_z = 2$ eigenmode. In the crossover, the composition of the collective mode corresponds to both amplitude and spatial oscillations of the order parameter.

5.2 Theoretical model

To understand the continuous evolution and character of the resonance, we develop a theoretical model in which the dynamics of the order parameter $\Psi(z,t)$ are described by the equation of motion

$$iK_1\frac{\partial\Psi(z,t)}{\partial t} - K_2\frac{\partial^2\Psi(z,t)}{\partial t^2} = \left(-\frac{\hbar^2\partial_z^2}{2M} + V(z,t) - r_0 + u_0|\Psi(z,t)|^2\right)\Psi(z,t), \quad (5.1)$$

derived from a zero-temperature effective field theory[15]. We consider a homogeneous system along the x-y plane and decompose $\Psi(z,t)$ into the $n_z = 0$ and $n_z = 2$ eigenstates of the harmonic potential $V(z,t)$. In this model, the coefficients K_1, K_2, r_0, and u_0 parameterize the BEC-BCS crossover. These are determined from theoretical predictions for the energy gap, condensate density [96], and speed of sound [97] in the crossover. In the limit where $K_1 = 0$, Eq. 5.1 reduces to a nonlinear Klein-Gordon equation, describing the order parameter dynamics in the weakly interacting BCS regime. The resulting equation is Lorentz invariant, which is a manifestation of particle-hole symmetry. In the BEC limit, where $K_2 = 0$, Eq. 5.1 reduces to the Gross-Pitaevskii equation.

The black dashed line in Fig. 5.3a represents the eigenfrequency difference between the ground and second excited state as analytically obtained from Eq. 5.1, taking into account interactions to leading order. Towards the BEC regime, this analytical result is in excellent agreement with the experimental observation. The full numerical simulation in the presence of trap modulation (black solid line) extends

[15] This field theory is based on the time-dependent Ginzburg-Landau theory, introduced in Ch. 3.3, featuring the same K_1 and K_2 terms. It is extended to include the discrete energy levels from the strong confinement.

the agreement throughout the entire BEC-BCS crossover without any fitting parameters. Beyond capturing the mode frequencies, this numerical approach also reveals the composition of the collective excitation due to hybridization, distinguishing between its amplitude and breathing mode components. The theoretical amplitude mode contribution is shown in Fig. 5.3b, and represents the fraction of the response where the total superfluid density oscillates in time. In the BCS regime ($\eta \gtrsim 1.9$), this contribution approaches its maximum value, resembling a pure amplitude mode (see red curves in Fig. 5.1). Towards the strongly correlated regime ($\eta \sim 1$), the amplitude mode contribution gradually decreases, and the mode gains breathing character. Finally, in the BEC limit, the dominant excitation is a pure breathing mode, where the superfluid density is constant in time, and oscillates spatially between $n_z = 0$ and $n_z = 2$ (see blue curves in Fig. 5.1).

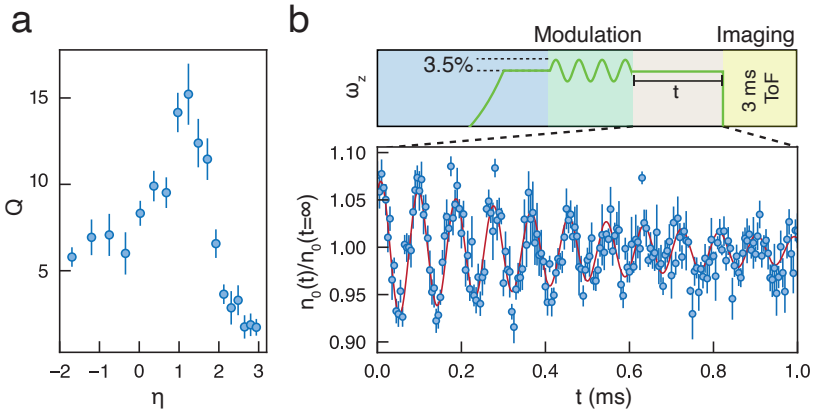


Figure 5.4: **a)** Quality factor along the BEC-BCS crossover. We quantify the spectral width via the quality factor Q, extracted from the spectral response in the BEC-BEC crossover. For all interaction strengths, we find $Q > 1$, signaling a long-lived excitation throughout the BEC-BCS crossover. The maximum value $Q = 15 \pm 2$ occurs in the strongly correlated regime. **b)** In this regime ($\eta = 1.2$), the collective mode is resonantly excited with a four-period modulation of the trapping frequency. This is followed by a free evolution for a time span t. We observe oscillations of the central density n_0 after a ToF expansion of 3 ms. The experimental data are fitted with a damped oscillation yielding a decay time $\tau = (610 \pm 60)\,\mu$s which results in $Q = 21 \pm 2$.

5.3 Lifetime and free oscillations of the condensate

One feature not captured by our theoretical model is the behavior of the spectral width throughout the crossover, particularly its narrowing in the hybridization regime, which suggests a long-lived and well-defined mode. We quantify the coherence of the mode by computing the quality factor $Q = \omega_0/\delta\omega$, where ω_0 is the resonance frequency and $\delta\omega$ is the full width at half maximum extracted from the spectrum. In the entire crossover, the mode remains underdamped with $Q > 0.5$ (Fig. 5.4a). Notably, the largest quality factors are found at $\eta < 1.9$, reaching a maximum value in the strongly interacting regime ($\eta \sim 1$). Here, the mode energy is below the onset of the pair-breaking continuum, suggesting that single-particle decay is suppressed, leading to longer lifetimes [84, 98, 99]. This contrasts with a conventional case, where the amplitude mode resides at the onset of the pair-breaking continuum, resulting in strong damping and limited visibility [100–103]. To further confirm the long-lived nature of the mode, we track the free coherent oscillations of the system at $\eta = 1.2$ after a short resonant excitation (Fig. 5.4b). We observe a long-lived oscillation at the collective mode frequency ω_0 when measuring the change in the

central density of the cloud after 3 ms of ToF. Fitting the data with an exponentially damped oscillation with a decay time τ, we obtain a quality factor $Q = \tau\omega_0/2 \approx 21 \pm 2$, comparable with our results from trap modulation spectroscopy.

5.4 Breakdown of superfluidity at T_c

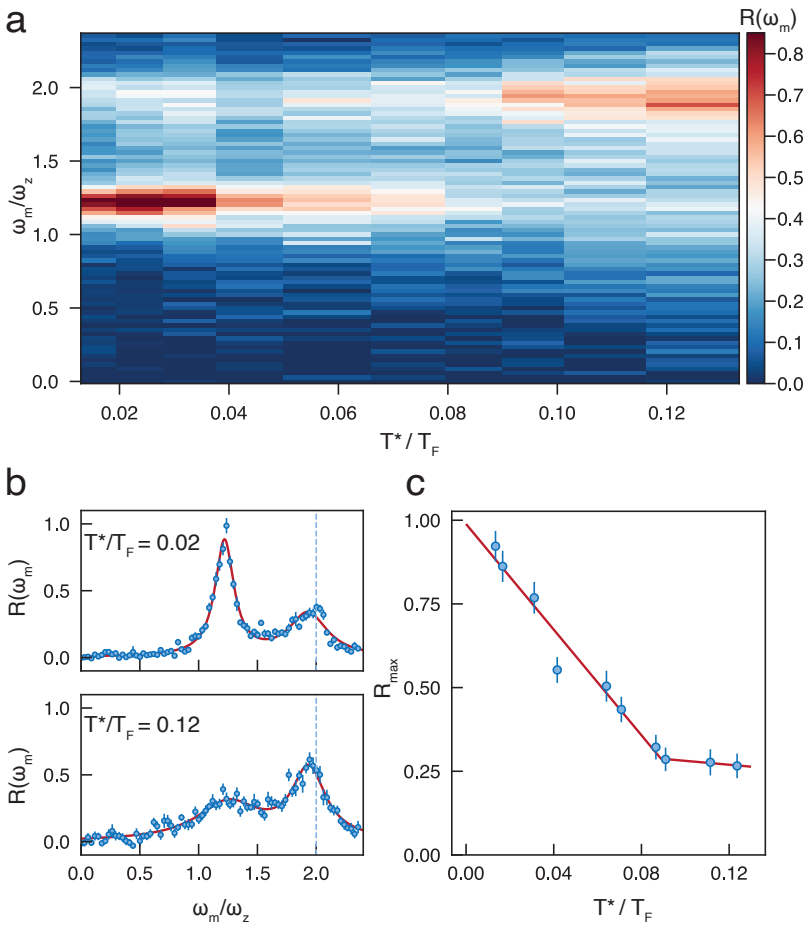


Figure 5.5: **a**) Vanishing of the collective mode above the critical temperature. We measure the spectral response $R(\omega_\mathrm{m})$ in the strongly correlated regime $(\eta = 1.2)$ as a function of temperature. The collective mode frequency remains nearly constant at $\omega_\mathrm{m}/\omega_z \sim 1.2$. As the temperature increases, the mode broadens, and its visibility diminishes, signaling the loss of coherence. Above a critical temperature, single-particle transitions at $2\hbar\omega_z$ become the dominant process due to thermally broken pairs. **b**) To extract the critical temperature, we fit the maximum response of the collective mode R_max by a double Lorentzian function (red line) shown for two vertical cuts of panel a. **c**) The temperature dependence of the maximum response shows a kink, which we identify as the critical temperature T_c^*. Employing a bilinear fit (red line), we obtain $T_\mathrm{c}^* = 0.088(4)\,T_\mathrm{F}$.

Since the observed dynamics are compatible with oscillations of the order parameter, we expect a strong temperature dependence, especially close to the superfluid critical temperature T_c. To explore this further, we prepare a strongly interacting system $(\eta = 1.2)$ at different temperatures and perform trap-modulation spectroscopy. Fig. 5.5a shows the spectral response as a function of temperature T^*/T_F. With increasing temperature, the resonance at $2\hbar\omega_z$ associated with single-particle excitations from thermally broken pairs becomes the dominant contribution to the spectrum (see Fig. 5.5b). Meanwhile, the collective mode with lower frequency broadens and its spectral weight decreases. The frequency remains constant, resembling the behavior previously observed in Refs. [58, 68, 104]. In Fig. 5.5c, the peak amplitude of the mode as a function of temperature is plotted. The observed trend is well described by a bilinear fit, featuring a

kink at a temperature of $T_c^* = 0.088(4)\,T_F$. Remarkably, our previous experiments on the critical velocity in 2D Fermi gases show a critical temperature of $T_c^* = 0.09(2)\,T_F$ [6]. This supports the interpretation that the collective mode is an excitation of the order parameter which vanishes above a critical temperature.

Summary and conclusion

This chapter focuses on a fundamental feature of strongly confined fermionic superfluids: the hybridization of collective modes. We observe a well-defined resonance in the entire BEC-BCS crossover, which we interpret as an excitation of the order parameter. This interpretation is supported by the strong suppression of the resonance above the critical temperature and the excellent agreement with the effective field theory.

Additionally, we show that trap modulation spectroscopy is a powerful tool for determining the pairing gap in the BCS regime and the superfluid-to-normal transition in the crossover. This is of interest for studying spin-imbalanced superfluids and other strongly correlated 2D systems.

Beyond ultracold atoms, these results provide insights into the hybridization of modes in confined fermionic superfluids and superconductors, such as low-dimensional materials and nano-superconducting devices. Here, the hybridization could influence fundamental properties such as the critical velocity or critical temperature. Our work paves the way to investigate more complex dynamics of the order parameter under confinement [105, 106], such as frequency beating [107], drum modes [90], exotic Higgs bound states [108, 109] or Leggett modes [110–112]. Finally, it is an exciting prospect to use confinement to control the properties of many-body systems by admixing higher harmonic oscillator states [113, 114].

Part III

Repulsive Bose polarons

6 POLARONS

An impurity interacting with a bath is a conceptually easy, yet non-trivial problem in quantum many-body physics. In this scenario, the impurity displaces particles from the bath in its vicinity, forming a dressing cloud (see Fig. 6.1). The result is the *polaron* quasiparticle, which behaves similarly to the free particle since its wavefunction $|\psi(\mathbf{k})\rangle$ has a finite overlap with that of the undressed particle $c_{\mathbf{k},\sigma}|0\rangle$. This overlap $Z(\mathbf{k}) = |\langle\psi(\mathbf{k})| c_{\mathbf{k},\sigma}|0\rangle|^2$ is also called the quasi-particle residue or weight and decreases the stronger the dressing becomes. As a result, the polaron typically behaves like a free particle but features its own energy E_P and a renormalized mass m^*, since it drags the displacement through the bath as it moves.

The initial description of the polaron was formulated by Landau and Pekar in 1948 [16], after Pekar had already recognized that a free electron in an ionic lattice can displace the ions, creating a potential well that leads to its localization [115]. They proposed many of the fundamental properties that we just established, namely the quasiparticle residue Z, energy E_P, and effective mass m^*. A rigorous theory for this system was first developed by Fröhlich [116] through electron-phonon interactions, leading to the celebrated Fröhlich Hamiltonian, which describes a broad range of phenomena.

In the following years, the polaron framework was extended beyond ion crystals and studied across a broad range of systems (see, e.g., the reviews in [17] and [117]). A few notable observations that can be described in the polaron picture include optically excited excitons in doped semiconductors [118] and color centers in perovskites [119].

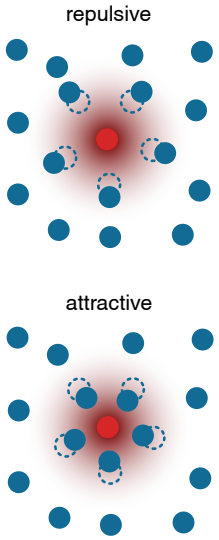


Figure 6.1: Sketch of the polaron quasiparticle. Impurity (red) immersed in a bath (blue), displayed for attractive and repulsive impurity-bath interactions. The polaron displaces the particles in the bath, forming a dressing cloud (shaded area).

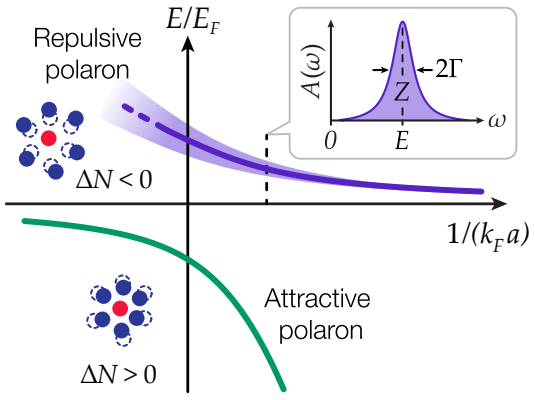


Figure 6.2: Repulsive and attractive branches of a Bose/Fermi polaron. While the attractive branch is at lower energy and stable, the repulsive branch can decay, leading to a broader mode. Adapted from [18].

Naturally, studying polarons in quantum gases is of great interest, as it provides a clean, highly controllable platform. Here, polarons can generally be divided into two classes depending on the quantum

statistics of the bath: The *Bose polaron*, for a bath that is a BEC, or the *Fermi polaron*, for a degenerate single-component Fermi gas. The statistics of the impurity itself are irrelevant to the labeling. Since the impurity-bath interactions are tuned via Feshbach resonances, there are typically two branches: One for repulsive and one for attractive interactions (see Fig. 6.2). It is important to note that the attractive branch also extends to positive scattering lengths, since it transitions into the molecular bound state that becomes energetically favorable for $1/k_{\mathrm{F}}a > 0$. This is also visible in the polaron energy E_{P} which approaches the binding energy E_{B} for increasing $1/k_{\mathrm{F}}a$. The repulsive branch, on the other hand, sits at higher energies and is therefore metastable towards decay into the attractive branch. Especially at strong interactions, the overlap with the underlying bound state increases, leading to rapid decay.

In Ch. 7, I demonstrate how we manage to eliminate this loss channel from the repulsive branch of the Bose polaron. But before that, I will first introduce the basic concepts and previous experimental studies regarding Bose polarons in the following section Ch. 6.1, while, for completeness, Ch. 6.2 briefly explains Fermi polarons and their main differences to Bose polarons, including a short overview of recent studies.

6.1 Bose polarons

As we already know, Bose polarons are impurities immersed in a BEC. These types of polarons are of particular interest because, in the weakly interacting limit, they map to the Fröhlich Hamiltonian, which is used to describe the original polaron problem of an electron in an ion lattice [117]. This makes the Bose polaron an ideal platform for quantum simulation of impurities in solid-state systems. However, because interactions can be tuned freely using Feshbach resonances, it is possible to reach the regime of strong interactions, where the system goes beyond the Fröhlich Hamiltonian, and properties change qualitatively. One example of this is the bound state that the attractive branch transitions into.

In recent years, the Bose polaron has been studied extensively in a broad range of experiments [120–125]. Notably, in [122, 123, 125], the polaron quasiparticle energies E_{P} were extracted for both the repulsive and attractive branches, including at varying temperatures in later studies [124, 126]. All of these studies extract the polaron spectrum by using radio-frequency (RF) pulses to address the impurity state $|2\rangle$ (see Fig. 6.3a). These RF pulses either address a transition from the bath state $|1\rangle$ (as in [122]) or another, third state $|3\rangle$ (as in [123]). Ideally, the bath, or the third state, are only weakly interacting, such that the polaron energy directly corresponds to the energy shift with respect to the bare RF transition ω_{bare}, leading to $E_{\mathrm{P}} = \hbar(\omega_{\mathrm{res}} - \omega_{\mathrm{bare}})$. Here, ω_{res} is the resonance frequency measured by RF spectroscopy.

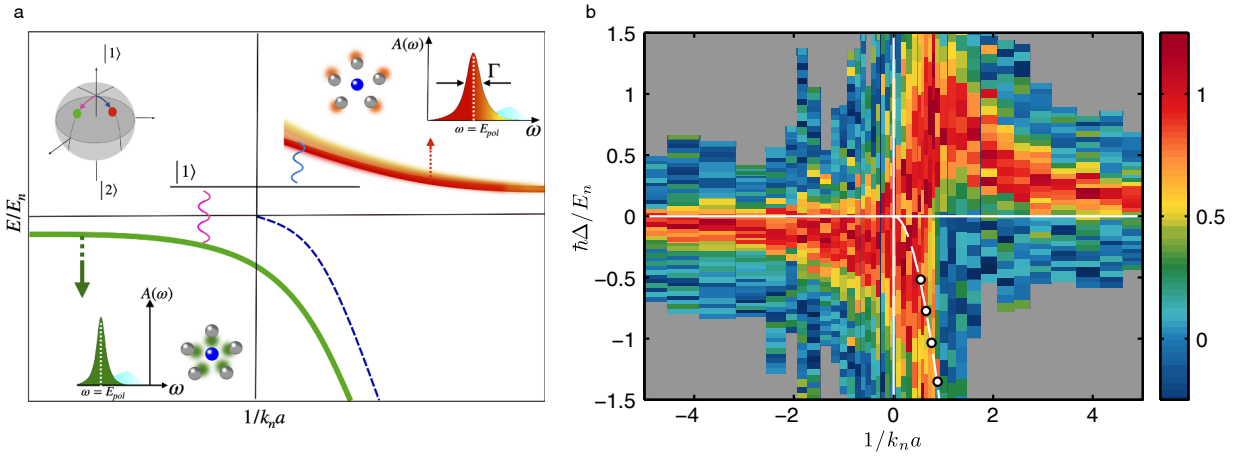


Figure 6.3: Energy spectrum of a Bose polaron. a) Schematic of the attractive and repulsive branch. The attractive branch is the ground state and approaches the molecular state at $1/k_n a > 0$. The repulsive branch is at positive energies and, under strong interactions, is unstable to decay into the attractive branch or the molecular channel. RF-injection spectroscopy allows access to the spectral function resulting from these branches by taking a small fraction of atoms into the interacting state $|2\rangle$, from an initial weakly interacting state $|1\rangle$, which can either be the bath itself or an additional non-interacting state. Adapted from [117, 122]. b) Observed polaron spectrum from RF-injection spectroscopy. The repulsive and attractive branches are well visible until they become indistinguishable in the strongly interacting regime due to broadening. Adapted from [122].

The spectrum extracted from [122] is shown in Fig. 6.3, where both branches are clearly visible. If we start in the weakly attractive regime, we find the attractive branch, with a negative polaron energy that decreases further as interactions increase. Following this branch to positive $1/k_n a$, the polaron becomes bound in the Feshbach molecule and approaches the binding energy E_B.

Furthermore, on the repulsive side, we can see the repulsive branch at positive energies. It is broader than the attractive branch because of its metastability. In the strongly interacting regime, the decay processes become dominant, leading to the repulsive branch broadening until it becomes indistinguishable from the attractive one. This issue is exacerbated by the existence of a continuum of many-body states that lie between the repulsive and attractive branches, since the system is highly compressible and higher-order collision processes occur more frequently.

Generally, more advanced techniques can be used to reduce the width of the extracted spectra somewhat. Recent studies in the Hadzibabic group [125], using a homogeneous 3D box potential, eliminated inhomogeneous broadening and were able to extract the polaron energies of the repulsive branch down to $1/k_n a_{IB} \approx 0.5$, while at the same time extracting the energies of the molecular branch. In another recent experiment [127], Ramsey interferometry was used to observe beating between the quasiparticle branches, also allowing them to extract E_P of the repulsive branch in the strongly interacting regime, down to $1/k_n a_{IB} \approx 1$.

However, numerous open questions regarding Bose polarons remain, primarily due to the rich physics in the strongly interacting regime. Here Efimov and few-body bound states with more bosons can hybridize with the polaron spectrum [128–131]. But more fundamentally, currently there is only one study measuring the effective mass of a Bose polaron in 1D [121], while the effective mass in 2D and 3D remains an open question.

In Ch. 7, I will present a scheme that allows us to eliminate the loss channel into the attractive branch by using fermions already bound

in bosonic dimers and exploiting the discrete energy levels of the confining potential to create impurities. This allowed us to extract the polaron energies, quasiparticle residue, and effective mass.

6.2 Fermi polarons

Fermi polarons were actually studied earlier than their bosonic counterparts, with the first experiments reported by the Zwierlein group in 2009 [132], followed by various further studies in a number of groups [14, 133–146]. Since there are several excellent review papers on Fermi polarons [18, 147–151], I will provide only a brief overview of the basic features and the current state of the field.

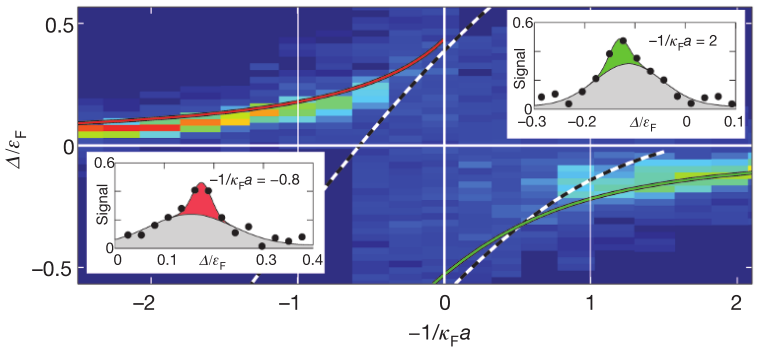


Figure 6.4: Extracted energy spectrum for the Fermi polaron, obtained by RF injection spectroscopy. The green and red lines are the theory predictions for the attractive and repulsive branch, respectively. Adapted from [140].

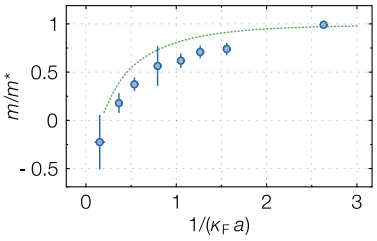


Figure 6.5: Inverse of the effective mass of a repulsive Fermi polaron. As the dressing increases for stronger interactions, the inverse effective mass moves towards o and finally turns negative. This has been interpreted as a signature of the repulsive state becoming unstable towards decay into the bound state. Adapted from [146].

The main difference between Fermi and Bose polarons lies in the statistics of the bath, which, in the fermionic case, is not a condensate but a single-component degenerate Fermi gas. As a consequence, Pauli blocking restricts scattering between the impurity and the bath, since only fermions close to the Fermi surface are allowed to scatter. Therefore, the dressing cloud is typically smaller than that of Bose polarons and the theoretical description easier. Additionally, this results in only the two-particle bound states being present in the strongly interacting regime, yielding distinct attractive and repulsive branches even at strong interactions.

Fermi polarons are generally much better understood than their bosonic counterparts. The full polaron energy spectrum was first measured in [140] (see Fig. 6.4), and due to the simpler nature of the possible excitations, theoretical descriptions fit remarkably well, even in the strongly interacting regime. Additionally, unlike for Bose polarons, the effective mass was extracted (Fig. 6.5) [133, 146]. These measurements accessed momentum-resolved energies by exploiting the occupation of low-momentum states upon injecting a variable, controlled density of fermionic impurities. Furthermore, Fermi polarons have also been studied in lower dimensions [14, 134, 141, 142], again extracting the polaron energies of the repulsive and attractive branch, as well as the effective mass. Theory predictions are generally in good agreement with the experimental observations.

However, a few open questions remain, e.g., how polaron-polaron interactions manifest, as previous experiments have reported conflicting signs for these interactions [138, 152, 153]. Furthermore, the limit of large mass imbalance between impurity and bath may be of interest, since this allows for bound states with more than two fermions [154].

7 THE SYNTHETIC SPIN POLARON

This chapter presents the first main result of this thesis: The creation and characterization of repulsive Bose polarons, using the discrete energy levels of the strong confinement as synthetic spin. Besides eliminating the dominant decay path for repulsive polarons, we measure the polaron energy, effective mass, and the quasiparticle residue well into the strongly interacting regime. The corresponding manuscript is currently under review and published as a preprint in

> *R. Henke, L. Levinsen, M. M. Parish, J. Boronat, G. E. Astrakharchik, H. Moritz, C. R. Cabrera, arXiv:2511.03569v1 (2025) [19]*

and reprinted here with minor modifications. The conception and conduct of all measurements presented here were jointly performed by Cesar Cabrera and me. The theoretical T-matrix description was developed by Jesper Levinsen and Meera Parish, while the QMC calculations were conceptualized and performed by Grigori Astrakharchik and Jordi Boronat. The entire work was supervised by Cesar Cabrera and Henning Moritz.

7.1 Polaron mapping

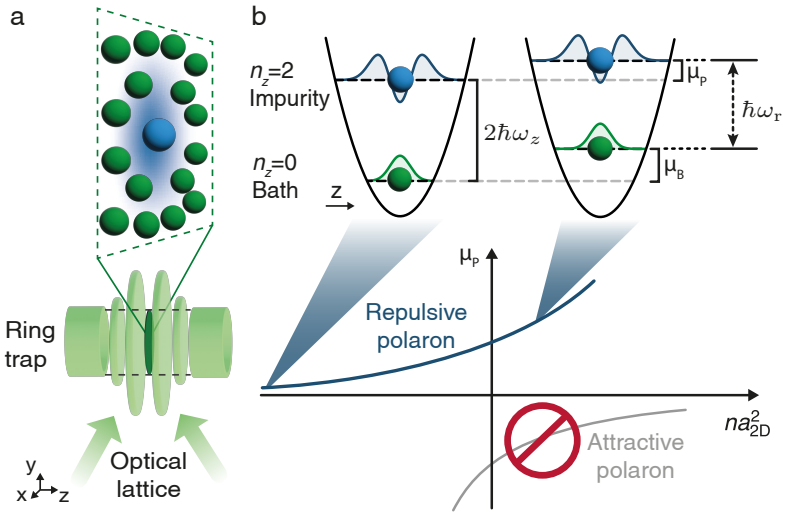


Figure 7.1: Experimental realization of repulsive synthetic-spin polarons. a) An impurity (blue) is immersed in a homogeneous 2D Bose-Einstein condensate (green). The atomic cloud is confined to a single 2D plane of a blue-detuned optical lattice in combination with a ring trap (box potential in the radial plane). b) The eigenstates of the harmonic trapping potential along the z direction play the role of synthetic spins, allowing us to realize a 2D repulsive polaron. Here, the bath corresponds to a superfluid of density n in the ground state $n_z = 0$, while the impurity is created by populating a higher level such as $n_z = 2$. Without interactions, the energy $\hbar\omega_r$ to address this transition is $2\hbar\omega_z$, the harmonic oscillator level spacing. With increasing repulsion na_{2D}^2, $\hbar\omega_r$ exhibits an interaction shift arising from the difference between the bath chemical potential μ_B and the repulsive polaron energy μ_P. In contrast to previous Bose polaron realizations, there is no underlying attractive branch.

Here, we experimentally realize a stable repulsive Bose polaron in the strongly interacting regime, overcoming the intrinsic metastability observed in previous studies [122, 123, 125, 127]. We focus on the two-dimensional (2D) geometry (Fig. 7.1a), where correlations are enhanced and striking phenomena are predicted, such as effective mass divergence and the breakdown of the quasiparticle picture [155–160]. Our approach employs bosonic Feshbach molecules consisting of pairs of fermions [3], which have strong immunity against typical

three-body decay due to the Pauli exclusion principle [161]. In addition, they feature repulsive interactions [161] with large tunability, allowing us to realize strongly repulsive superfluids. Simultaneously, the strong 2D confinement enables us to create impurities within the superfluid by exciting a small number of dimers from the ground state to an excited state of the trapping potential, with the quantum number n_z acting as a synthetic spin (Fig. 7.1b). This mapping of impurity and bath into different vibrational states gives rise to a new class of quasiparticle which we term the *synthetic-spin polaron*, characterized by purely repulsive interactions and the absence of any underlying attractive branch. We access the polaron spectral function and extract the polaron quasiparticle properties using trap modulation spectroscopy and Bragg spectroscopy. Most notably, we measure the effective mass of the Bose polaron for the first time, observing values exceeding twice the bare mass of a non-interacting impurity, a hallmark of strong many-body dressing. Comparisons with quantum Monte Carlo (QMC) and T-matrix theories reveal pronounced beyond-mean-field effects in a regime previously inaccessible.

The experiments are performed in a homogeneous gas of bosonic dimers, each composed of two ^{6}Li fermions occupying the lowest two hyperfine states. To ensure the bosonic character of the system, we stay in the regime where the dimer size is smaller than the interparticle distance. The cloud is confined in a highly anisotropic geometry with a trapping frequency $\omega_z = 2\pi \cdot 11.4\,\mathrm{kHz}$ along the vertical direction, and a uniform box potential providing horizontal confinement [6, 75], as illustrated in Fig. 7.1a. The typical temperatures measured after an adiabatic ramp to low interactions are $\widetilde{T} \leq 0.02\,T_\mathrm{F}$, where T_F is the Fermi temperature (further experimental details in Ch. 4). We tune the interaction strength via a broad Feshbach resonance [6, 75]. It is quantified using the dimensionless gas parameter $na_{2\mathrm{D}}^2$, where n is the total 2D dimer density and the scattering length $a_{2\mathrm{D}}$ is obtained by mapping the 3D interaction between composite dimers [161] to the quasi-2D geometry [38]. The gas parameter also defines the dimensionless parameter $\ln(k_n a_{2\mathrm{D}})$, which is commonly used to describe 2D systems, where $k_n = \sqrt{4\pi n}$ is the characteristic momentum scale. We note that in our scheme, the underlying microscopic interaction potential between the $n_z > 0$ impurity and the bath particles is the same as that between particles in the bath, with differences in the effective interactions being due to the transverse overlaps[16] O_{n_z}. Specifically, the impurity-bath interactions are typically reduced, with an effective 2D scattering length given by $k_n a_{2\mathrm{D},n_z} = (k_n a_{2\mathrm{D}})^{1/O_{n_z}}$. This effect is conceptually similar to the scenario of ^{3}He impurities in superfluid ^{4}He [162], where the larger volume occupied by the lighter ^{3}He atom yields different effective interactions despite the same underlying interaction potential.

[16] The overlaps are calculated from the harmonic oscillator wavefunctions $\varphi_{n_z}(z)$, leading to

$$O_{n_z} = \frac{\int dz\,|\varphi_{n_z}(z)|^2 |\varphi_0(z)|^2}{\int dz\,|\varphi_0(z)|^4} = \begin{cases} \frac{1}{2} & n_z = 1 \\ \frac{3}{8} & n_z = 2 \end{cases}.$$

7.2 Extraction of the quasiparticle properties

7.2.1 Trap modulation spectroscopy

To probe the properties of a 2D Bose polaron, we measure its spectral response using trap modulation spectroscopy [10] (see Ch. 4.3.4), which is equivalent to injection radio-frequency (RF) spectroscopy widely used in Bose polaron experiments in the case of a BEC [122, 125]. Specifically, we modulate the vertical trapping frequency as $\omega_z(t) = \omega_z(1+\alpha \sin(\omega_m t))$, with modulation frequency ω_m and a small amplitude of $\alpha \leq 0.5\,\%$. This transfers a small fraction of dimers from the superfluid ($n_z = 0$) into the $n_z = 2$ harmonic oscillator level, acting as impurities populating the repulsive polaron branch. Following the excitation, a 20 ms hold time allows for collisions between impurities and the bath, resulting in energy redistribution and measurable heating, as explained in Ch. 4.3. The heating rate of the condensate is directly linked to the zero-momentum spectral function $A_2(\omega)$ for the $n_z = 2$ impurities (see Ch. 4.3.4):

$$\frac{dE}{dt} \propto A_2(\omega_m + \mu_B)\,. \tag{7.1}$$

This mapping demonstrates that trap modulation provides the spectral information of injected $n_z = 2$ impurities (polarons) into the condensate, and consequently that eigenstates of the trap can be exploited as synthetic spin. Note that this differs from previous experiments on trapped motional states in a quantum bath, which only explored weak interactions and required a different species of atom for the impurity [163, 164].

Experimentally, we quantify the heating rate via the response function $R(\omega_m) = 1 - C(\omega_m)/C(0)$. Here, $C(\omega_m)$ corresponds to the amplitude of low-momentum atoms, determined from the bimodal momentum distribution after time-of-flight imaging. It is normalized by the unperturbed amplitude $C(0)$, such that $R(\omega_m)$ becomes nonzero when the modulation is resonant with an excitation. In the limit of small energy transfers, $R(\omega_m)$ is proportional to dE/dt, and according to Eq. (7.1), proportional to the polaron spectral function.

7.2.2 Polaron energy

In Fig. 7.2a, we show $R(\omega_m)$ as a function of the gas parameter. The excitation spectrum features a well-defined resonance across the entire interaction range, clearly below the bare transition $2\omega_z$ (dashed line). Additionally, a second mode appears at $2\hbar\omega_z$ for larger interactions, corresponding to thermal dimers and unpaired fermions that are parametrically heated. The interaction shift $\Delta = \hbar(\omega_r - 2\omega_z)$, shown in Fig. 7.2b, consists of two contributions: the chemical potential of the bath μ_B, representing the energy lost by removing a particle from the condensate, and the polaron energy μ_P, corresponding to the energy required to add an impurity into the

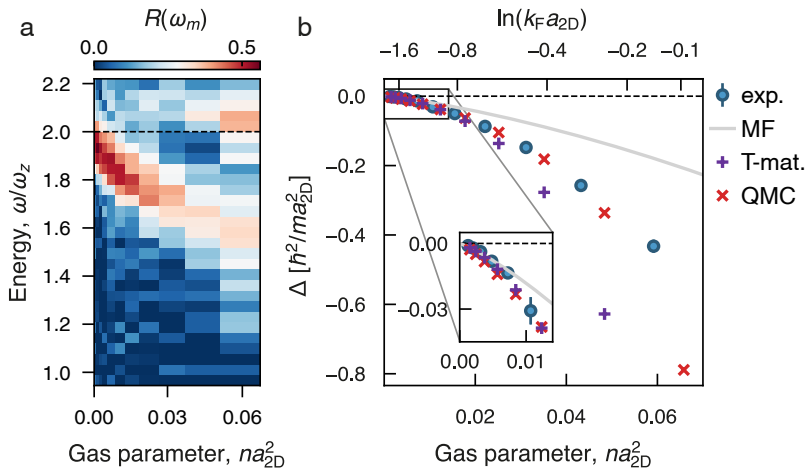


Figure 7.2: Polaron energies from trap modulation spectroscopy. a) Response $R(\omega_m)$ measured via trap modulation spectroscopy. A well-defined mode is visible, corresponding to the creation of polarons in the $n_z = 2$ state. b) Energy shift Δ, extracted from Lorentzian fits to the spectra shown in panel (a). The error bars of the experimental data are small compared to the symbol size. A comparison with QMC theory shows excellent agreement up to $na_{2D}^2 \lesssim 0.05$ in the strongly interacting regime. Both T-matrix and QMC theories deviate for large interactions, where the details of the scattering potential become relevant, while MF theory fails already for moderate interactions. For small interactions, all theories agree well with the experiment (inset).

system. Their difference yields the total energy shift: $\Delta = \mu_P - \mu_B$. Notably, due to the reduced spatial overlap between the impurity and the bath, we find that $\mu_B > \mu_P$, and hence $\Delta < 0$, even though the polaron is repulsive, $\mu_P > 0$. Since μ_B has been previously calculated in weakly interacting 2D Bose gases [43, 165, 166], our measurement of Δ provides experimental access to the polaron energy μ_P (discussed below), revealing the many-body dressing of the impurity.

To test the validity of the polaron description, we compare our experimental results with two complementary theoretical approaches—diffusion Monte Carlo simulations (denoted as QMC) and a T-matrix-based polaron theory—which highlight different aspects of the interactions (see supplementary material of [19]). Specifically, the T-matrix theory precisely captures the low-energy two-body scattering between an $n_z > 0$ impurity and an $n_z = 0$ bath particle, including the possibility of decay of the impurity, but it neglects interactions within the medium and multiple excitations of the medium, as well as the finite range of the interaction potential (set by the dimer size). Conversely, the QMC method captures finite-range effects and higher-order correlations, but it neglects decay mechanisms and treats the $n_z = 2$ impurity as distinct from the bath particles, as in the standard polaron scenario. Neither theory treats the constituent fermionic particles forming the bosons, which is reasonable since the mean interparticle distance exceeds the dimer size.

The remarkable agreement seen in Fig. 7.2b for $na_{2D}^2 \lesssim 0.02$ between both theories and the experiment indicates that the polaron picture indeed applies to excitations of the transverse degrees of freedom and that the resulting description is universal, as it does not depend on the precise details of the interaction potential. At stronger interactions, discrepancies between theories and experiment emerge, which can be attributed to missing correlations in the T-matrix theory as well as the growing importance of the microscopic details. First, the QMC description models the dimers as hard spheres, an approximation that becomes inaccurate when the dimer diameter

a_{3D} becomes comparable to the oscillator length l_z. Additionally, the gas enters the strongly correlated regime when $na_{2D}^2 \sim 0.1$, which, for reference, is near the crystallization point predicted for hard disks at $na_{2D}^2 \approx 0.18$ [167]. Finally, the composite nature of the bath particles becomes relevant when the dimer size becomes comparable to the distance between dimers. For comparison, we also include a mean-field (MF) prediction (grey line), which estimates the energy shift based only on the reduced spatial overlap between $n_z = 2$ and $n_z = 0$ harmonic oscillators. This trivial MF approach neglects many-body correlations intrinsic to polaron formation and breaks down in the intermediate to strongly interacting regime.

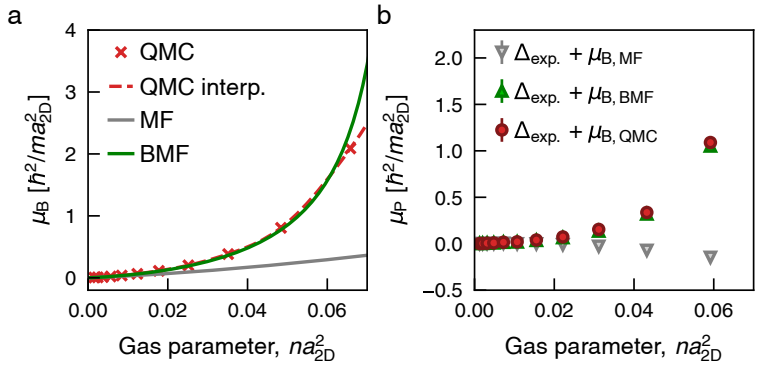


Figure 7.3: Comparison with various chemical potentials. a) Comparison of different predictions for the chemical potential μ_B of the bath (see text). b) Polaron energy $\mu_P = \Delta_{exp.} + \mu_B$, using the chemical potentials μ_B from a and $\Delta_{exp.}$ from Fig. 7.2. Since the values for $\Delta_{exp.}$ lie at different interactions than the QMC predictions, $\mu_{B,QMC}$ is taken from the cubic spline interpolation shown in a. For $na_{2D}^2 < 0.06$ the BMF and QMC predictions are expected to yield good results. In contrast, $\mu_{B,MF}$ underestimates the chemical potential, clearly visible from the negative predicted polaron energy $\mu_{P,MF}$.

If we want to access the polaron energies μ_P from this measurement, we have to make an assumption for the chemical potential of the bath μ_B, since the measured energy shift is $\Delta = \mu_P - \mu_B$. Here we compare the following predictions:

1. The chemical potential from our QMC calculations $\mu_{B,QMC}$.
2. The mean-field (MF) prediction of 2D bosons from [165] corresponding to

$$\mu_{B,MF} = \frac{4\pi\hbar^2 n/m}{|\ln na_{2D}^2|}. \tag{7.2}$$

3. A beyond-mean-field correction to $\mu_{B,MF}$ from Ref. [43], resulting in

$$\mu_{B,BMF} = \frac{4\pi\hbar^2 n/m}{|\ln na_{2D}^2| + \ln|\ln na_{2D}^2| + C_1 + \frac{\ln|\ln na_{2D}^2| + C_2}{|\ln na_{2D}^2|}}, \tag{7.3}$$

with coefficients

$$C_1 = -\ln\pi - 2\gamma - 1 = -3.3$$

$$C_2 = -\ln\pi - 2\gamma + 2 = -0.3.$$

Here, $\gamma \simeq 0.577$ is Euler's constant.

A comparison of the different chemical potentials is shown in Fig. 7.3a, and resulting polaron energies μ_P in b when adding μ_B to

the measured energy shift $\Delta_{\text{exp.}}$ from the experiment. Since our QMC theory agrees well with the results for $na_{2D}^2 < 0.06$ (see Fig. 7.2b), we expect the predicted chemical potentials to be close to the actual values for this regime. For larger interactions, the details of the scattering potential become relevant and the predictions for $\mu_{\text{B, QMC}}$ unreliable. The included BMF theory replicates these results. For completeness, we also included the 2D hard-core MF prediction $\mu_{\text{B,MF}}$, used in the main text, which clearly underestimates the chemical potential, leading to the prediction of negative polaron energies as a consequence. We therefore expect $\mu_{\text{B, QMC}}$ to be the most reliable prediction.

7.2.3 Lifetime and quasiparticle residue

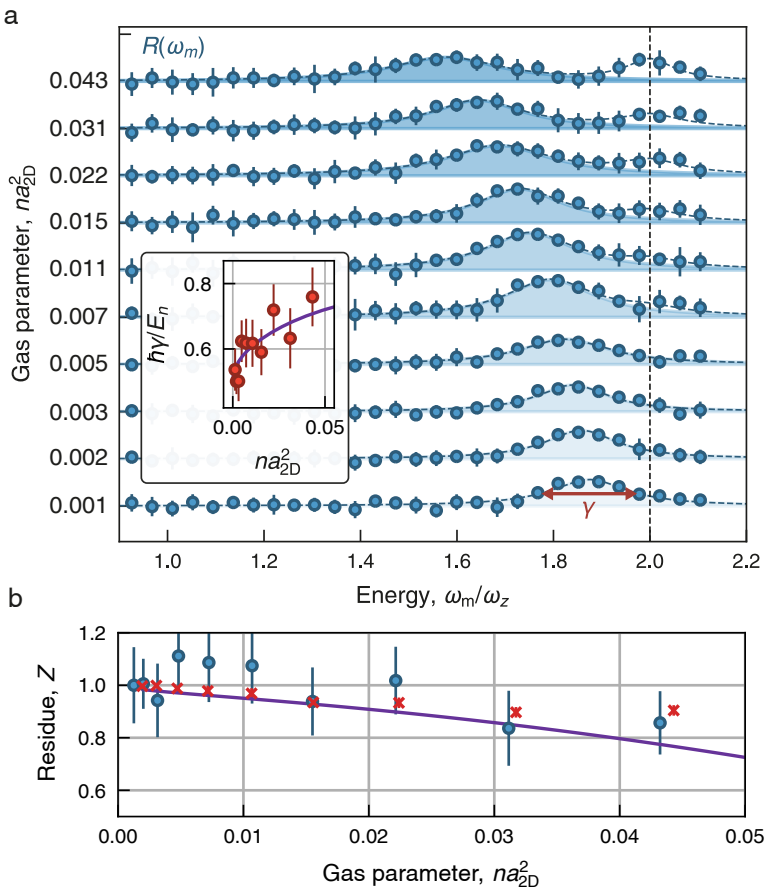


Figure 7.4: Spectral function at different interaction strengths. a) Ridge plot showing the response for different na_{2D}^2, directly connected to the spectral function $A_2(\omega_m + \mu_B)$. From Lorentzian fits (blue dashed lines), the full width at half maximum γ is extracted (inset), as well as the integral, shown as blue shaded areas, which determines the quasiparticle residue Z. As impurity-bath interactions increase, the spectral response shifts and broadens, reflecting strong correlations with the medium. A comparison of the width with T-matrix theory plus a constant offset (purple line) shows good agreement. b) Quasiparticle residue Z, quantifying the overlap between the dressed polaron and a non-interacting particle. For increasing na_{2D}^2, the extracted Z (blue circles) steadily decreases, signaling enhanced dressing by the bath, which is supported by QMC (red crosses) and T-matrix (purple line) calculations.

Having established the energy shift Δ as a proxy for the polaron energy, we now turn to two additional quasiparticle properties encoded in the spectral response: the lifetime and the quasiparticle residue, directly related to the spectral width and weight, respectively. As shown in Fig. 7.4a, the spectral response shows a well-defined resonance visible throughout the strongly interacting regime, indicating the remarkable stability of the repulsive polaron branch in our system.

The inset in Fig. 7.4a shows how the full width at half maximum (FWHM) γ (inverse lifetime) extracted from a Lorentzian fit remains narrow across the explored region, normalized by the characteristic energy scale $E_n = \hbar^2 k_n^2/(2m)$. This is in contrast to previous experiments [122, 123, 125], where the molecule-hole continuum was also observed. The difference arises from a fundamental distinction in how the repulsive branch is engineered. Unlike previous experiments, where the repulsion stems from the presence of an underlying molecular state [168], our scheme uses the residual repulsion between stable bosonic dimers [161, 169]. Therefore, the bound state responsible for the instability of the repulsive branch does not exist. This key feature not only leads to a robust, long-lived repulsive branch but also enables direct comparison with variational and quantum Monte Carlo descriptions, which typically neglect bound states [170, 171].

We additionally compare the width with the prediction from T-matrix theory. Within this theory, the width originates from collisions where the $n_z = 2$ impurity scatters into high-momentum states in the $n_z = 0$ level. We find that in order to match the experiment, we need to include a constant offset of $\hbar\gamma_{\text{Offset}}/E_n = 0.475 \pm 0.015$. Experimentally, this offset cannot be explained by the frequency resolution set by the driving duration, which only contributes to $\sim 10\,\%$ of the total width. The most plausible explanation is temperature effects. Those are not covered by our theoretical descriptions and require further investigation.

The second quantity encoded in the spectral function is the quasiparticle residue Z, which quantifies how much of the original undressed particle remains after interaction with the bath: $Z = 1$ for a free particle, while $Z < 1$ indicates many-body dressing [18]. In the spectral function, Z corresponds to the integrated weight of the resonance (shaded area in Fig. 7.4a), which we extract from the Lorentzian fits. The resulting values of Z, normalized to the weakest interaction strength ($na_{2\text{D}}^2 \sim 0.001$), are displayed in Fig. 7.4b, showing excellent agreement with our predictions. The gradual decrease for larger interactions signals the many-body dressing by the bath, while upholding the validity of the quasiparticle picture ($Z > 0$).

7.2.4 Effective mass

In addition to the energy shift Δ, spectral width γ, and quasiparticle residue Z, we measure the effective polaron mass m^*. This quantity characterizes the mobility of the impurity and follows the dispersion relation $E_{\text{P}}(q) = E_{\text{P}}(0) + \hbar^2 q^2/(2m^*)$. We measure $E_{\text{P}}(q)$ using Bragg spectroscopy, where a two-photon process transfers a precise energy $\hbar\omega_{\text{m}}$ and in-plane momentum $\hbar q$ to the impurity (see Fig. 7.5a). As described in our previous experiments [6, 8], the interference of two far-detuned laser beams creates a running-wave optical lattice with tunable spacing. It is important to note that coupling into the n_z states requires a small out-of-plane momentum component q_z (see Appendix 4.3.3), which we introduce by slightly tilting the Bragg

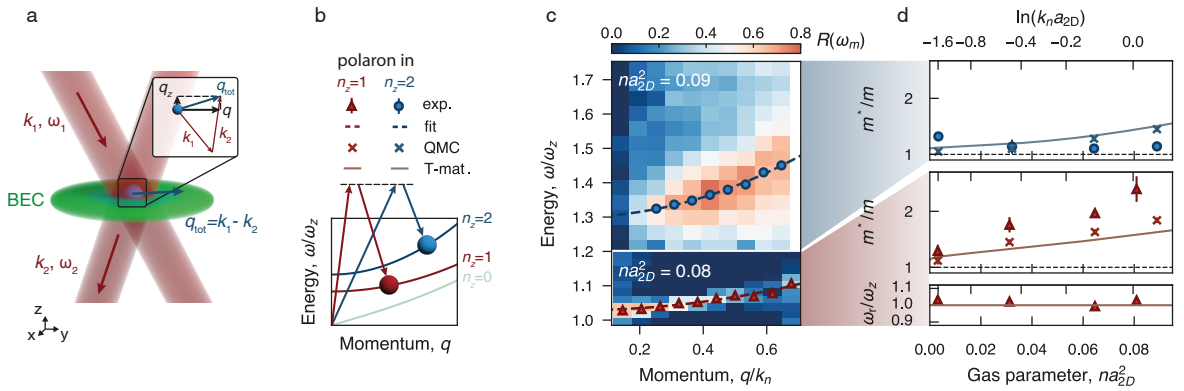


Figure 7.5: Effective mass of the $n_z = 1$ and $n_z = 2$ polaron. a) Creation of a polaron via Bragg spectroscopy: By overlapping two beams onto the atoms, a selected energy of $\omega_m = \omega_1 - \omega_2$ and momentum $\mathbf{q}_{tot} = \mathbf{k}_1 - \mathbf{k}_2$ can be transferred. Slightly tilting the beams allows for excitations into the $n_z = 1$ and $n_z = 2$ impurity states due to a small transverse momentum $q_z \ll q_{tot}$ imparted in addition to an in-plane momentum $q \approx q_{tot}$ (inset). b) Bragg spectrum of a bosonic superfluid, displaying the phonon ($n_z = 0$) and the impurity modes ($n_z = 1$ and $n_z = 2$). The inverse of the curvature of the impurity dispersion directly gives the effective mass m^*. c) Bragg spectra for the $n_z = 1$ (lower panel) and $n_z = 2$ (upper panel) in the strongly interacting regime. The energies $E_P(q)$ extracted from Lorentzian fits to the momentum slices, including the quadratic fits, are overlaid. d) Effective masses extracted from the quadratic fits to the Bragg spectra, including a comparison with QMC and T-matrix theory. The bottom panel shows the zero-momentum energies $\omega_r = E_P(q = 0)$ for $n_z = 1$ extrapolated from the fit. Remarkably, the energy shift from the bare transition remains zero for all gas parameters na_{2D}^2 due to symmetry.

beams (q_{tot}) relative to the atomic plane ($q_z \approx 0.05 q_{tot}$), see inset in Fig. 7.5a. As shown in Fig. 7.5b, this off-axis Bragg excitation allows transitions to $n_z = 1$ and $n_z = 2$, as the matrix elements between harmonic oscillator states are not constrained by parity [172]. Using the detection protocol introduced for Δ in Fig. 7.2, we measure the momentum-resolved resonance frequency.

A typical Bragg spectrum in the strongly correlated regime is shown in Fig. 7.5c. This spectrum combines two datasets for the $n_z = 1$ (bottom) and $n_z = 2$ (top) impurity. For each momentum slice, $E_P(q)$ is determined individually, allowing us to fit a quadratic dispersion [17], which gives the effective mass. For comparison, in our theory models, we extract m^* as follows: In QMC calculations, the effective mass is obtained from the imaginary-time diffusion coefficient assuming distinguishable impurities. Independently, using T-matrix theory, we extract the effective mass from the impurity self energy, which determines the momentum-resolved spectral function $A_{n_z}(q, \omega)$ (see supplementary material of [19]).

The resulting effective masses for the $n_z = 1$ and $n_z = 2$ polaron branches are shown in Fig. 7.5d for a wide range of na_{2D}^2. In the weakly interacting regime, the measured effective masses for both $n_z = 1$ and $n_z = 2$ are close to $2m_{Li}$, consistent with the picture of nearly free dimers moving through the bath. However, at strong coupling, the two branches noticeably differ. For the $n_z = 1$ impurity, we observe a pronounced increase in the effective mass, exceeding twice the bare dimer mass for our strongest bath-impurity coupling, which is much larger than the effective masses observed previously for Fermi polarons [133, 135, 141, 146]. Both T-matrix and QMC predictions qualitatively capture this increase, confirming this feature as a clear signature of many-body dressing arising from the repulsive dimer-dimer interactions and the absence of an underlying bound state [161].

By contrast, we measure a nearly constant effective mass for the $n_z = 2$ polaron. Although m^* for $n_z = 2$ is expected to be smaller than for $n_z = 1$ due to its reduced overlap with the bath, the absence of any noticeable increase with stronger bath-impurity coupling is unexpected. In both data sets, we verified that no systematic energy

[17] For extraction of the curvature, we do not include the value at $q = 0$ from trap modulation spectroscopy, since there is a small systematic energy shift between both measurements.

shifts appear when varying the driving strength, and that the effective mass from the quadratic fit does not change when removing the highest momenta from the data, ruling out non-quadratic contributions. The qualitative difference potentially stems from the fact that the $n_z = 2$ impurity can decay into the bath, whereas the $n_z = 1$ impurity is protected by parity symmetry. This is supported by their respective widths in Fig. 4c. Moreover, only the former exhibits a strong broadening at large momenta, a feature not captured by either theory, possibly because it requires decay processes involving multiple excitations of the medium.

While the effective mass reveals strong interaction effects for the $n_z = 1$ impurity, the energy shift shows a remarkably different behavior. The bottom panel of Fig. 7.5d shows the extrapolated zero-momentum energies $E_{\mathrm{P}}(0) = \Delta_{n_z=1} + \hbar\omega_z$ from Bragg spectroscopy, extracted from the quadratic fit. Surprisingly, there is no deviation from the bare transition across the full interaction range. This striking result stems from the parity symmetry of the trapping potential: since there are no odd-parity pairwise interactions, the $n_z = 1$ excitation can only go into the center-of-mass motion of the gas without changing its properties. This is in analogy with Kohn's theorem. Within the impurity picture, this property appears as a cancellation between the factor of 2 due to impurity-bath exchange *during scattering* (which is incorporated into our T-matrix approach) and the factor of 1/2 arising from the reduced spatial overlap between $n_z = 1$ and $n_z = 0$ wavefunctions. The resulting vanishing interaction energy shift thus highlights a subtle manifestation of quantum indistinguishability. Furthermore, the observed exchange process is a property of the impurity-bath interactions that exists even at $T = 0$. It is thus different from the exchange of thermal bosons that takes place in the driving transition in measurements of clock shifts in a thermal Bose gas [126, 173].

7.3 Conclusion

In conclusion, we have engineered a stable Bose polaron in 2D and measured the key properties from the weakly to the strongly interacting regime. Those include the polaron energy and the quasiparticle residue, finding excellent agreement with QMC predictions and T-matrix calculations. Furthermore, we determined the effective mass via Bragg spectroscopy, showing a significant increase in the effective polaron mass and absence of the energy shift Δ associated with the $n_z = 1$ polaron, due to bosonic statistics. Our work demonstrates how the internal states of the confining potential can be exploited as pseudospins, enabling momentum-resolved spectroscopy without relying on RF or Raman transitions. We term this long-lived quasiparticle the *synthetic-spin polaron*. Next steps include extending this approach to finite temperatures, which will enable the exploration of how thermal fluctuations affect polaron stability and mobility, thereby deepening

our understanding of quasiparticles in low-dimensional Bose systems. While this work focuses on the bosonic regime, our polaron mapping, based on internal states, can be extended to imbalanced Fermi gases [174], enabling exploration of the crossover between Bose and Fermi polarons within the same experimental platform.

Part IV

Imbalanced Fermi gases

8 IMBALANCED FERMI SUPERFLUIDS

This chapter provides a comprehensive overview of cold Fermi gases with spin imbalance. First, a brief introduction to the basic concepts underlying imbalanced Fermi gases is provided in Ch. 8.1, followed by a historical overview of previous experimental studies with neutral atoms in Ch. 8.2. Finally, in Ch. 8.3 we discuss in detail the 2D phase diagram predicted by various theories. A special focus is placed on superfluid phases that allow a local imbalance.

8.1 Imbalanced Fermi gases in a nutshell

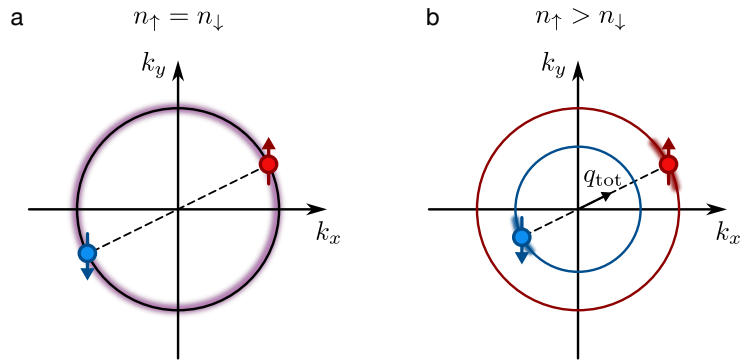


Figure 8.1: a) Matching Fermi surfaces in the balanced case ($n_\uparrow = n_\downarrow$). Pairing can happen on the entire Fermi surface (shaded region), since for particles with opposite momentum, the total pair momentum is $q_{\mathrm{tot}} = k_\uparrow - k_\downarrow = 0$ anywhere on the Fermi surface. b) In the imbalanced case, the Fermi surfaces do not match up anymore, and pairing becomes non-trivial. Scattering can only happen in a small region (shaded regions) because the non-zero pair momentum needs to be conserved.

As we have already discussed in Ch. 3, Cooper pairing is the fundamental mechanism underlying fermionic superfluidity. Due to Pauli exclusion, only fermions with opposite momenta on the Fermi surface are allowed to pair up and condense. For a balanced system, the Fermi surfaces of both components perfectly match, and pairing is straightforward (see Fig. 8.1a). It is easy to see, in contrast, that once there is a spin imbalance with $n_\uparrow > n_\downarrow$, the respective Fermi surfaces do not match anymore ($k_{\mathrm{F},\uparrow} > k_{\mathrm{F},\downarrow}$) and pairing becomes non-trivial (see Fig. 8.1b). Depending on the system, this can lead to the breakdown of superfluidity, phase separation into normal and superfluid domains, or one of various possible magnetized superfluid phases.

One of the first systems where spin imbalances were studied is conventional solid-state superconductors. Here, Cooper pairing occurs between electrons with opposite spin. One can induce a breakdown of superfluidity by applying a strong magnetic field. This happens because the field induces an energy difference between the chemical potentials of the two spin states as a result of the Zeeman shift. Once this difference exceeds the energy gained from the pairing mechanism, electrons can flip to the energetically more favorable spin state,

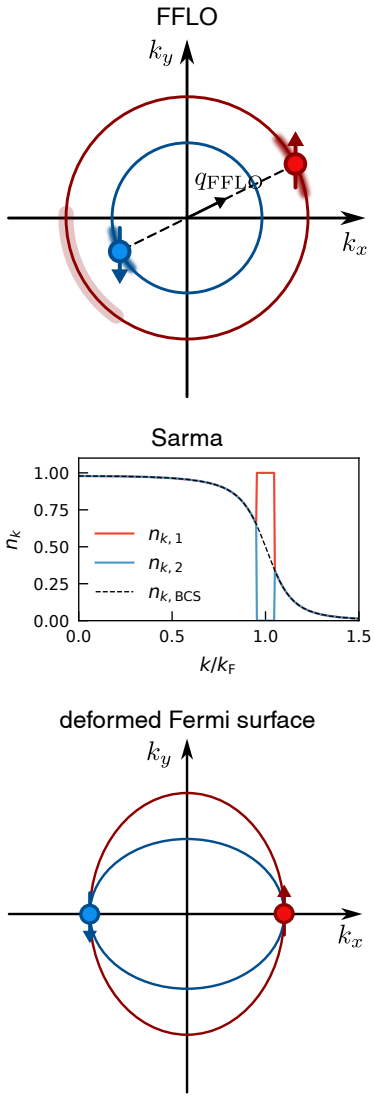


Figure 8.2: Different non-trivial phases for imbalanced superfluids. In the FFLO phase, pairing happens at finite pair momentum q_{FFLO} (dashed line and blurred regions), while part of the excess majority occupies the opposite region of momentum space (red shaded region), leading to a vanishing total momentum. In the Sarma phase, the region around k_F in momentum space is fully polarized, and pairing happens adjacent to this region. Another phase considers the deformation of Fermi surfaces, resulting in two overlapping regions on opposite sides, leading to pairing at $q = 0$.

creating an imbalance. Since the electrons can no longer pair, superfluidity breaks down. The critical magnetic field at which this occurs is called the Chandrasekhar-Clogston (CC) limit [11, 12].

Besides this transition from a balanced superfluid to a spin-imbalanced Fermi mixture in the normal phase, other phases have been predicted to support superfluidity, even in the presence of a spin imbalance, beyond the CC limit (see overview in Fig. 8.2). Most prominently, Fulde, Ferrell, Larkin, and Ovchinnikov independently predicted the FFLO phase, where fermions pair at a non-zero total momentum $\mathbf{q}_{\mathrm{FFLO}}$, leading to a spatially oscillating order parameter and local imbalance [175, 176]. Two other famous predictions are the Sarma phase [177] and a phase featuring a deformed Fermi surface [178–180]. The former features a gap in the momentum spectrum, in which the momentum states around k_F are fully polarized; it is therefore also called the "breached-pair" or "interior-gap" phase. The latter is easily understood by comparing it with the FFLO phase: Unlike pairing with a finite momentum $\mathbf{q}_{\mathrm{FFLO}}$ and keeping the two respective Fermi surfaces spherical, the Fermi surfaces deform elliptically, leading to an overlap on opposite sites that then allows pairing at zero pair-momentum. None of these phases has been observed directly in conventional superconductors so far. This is expected, since the imbalance is always created by applying a strong magnetic field, which induces orbital motion of the electrons due to their charge, further hindering superfluidity [181]. Only indirect measurements in layered superconductors have indicated the existence of an FFLO phase [182, 183], where the orbital motion is eliminated by orienting the magnetic field parallel to the layers, including specific heat [184], magnetic torque [185], and nuclear magnetic resonance measurements [186]. A direct observation, however, remains elusive as of now.

8.2 Exploring imbalanced Fermi mixtures with quantum gases

Quantum gases with neutral atoms offer an ideal framework for studying imbalanced Fermi gases, thanks to their high degree of control and the absence of the orbital limit. Not only is it possible to precisely tune the interactions from strongly attractive to repulsive via Feshbach resonances, but a specific imbalance can be fixed directly by using two different hyperfine levels or even different isotopes with mass imbalance. Additionally, absorption imaging allows direct observation of local imbalances or, when combined with time-of-flight expansion, provides access to the momentum distribution. This makes quantum gases predestined to explore the phase diagram of imbalanced Fermi mixtures in detail for varying interactions, polarizations, and temperatures.

8.2.1 3D Fermi gases

The first cold-atom experiments on spin imbalances were reported by the Ketterle group starting in 2006 [13, 132, 187–193], closely followed by the Hulet group [194, 195]. Both groups demonstrated

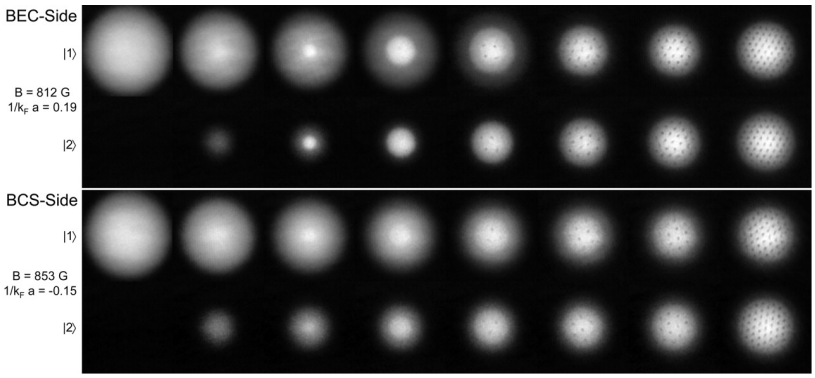


Figure 8.3: Imbalanced Fermi gases in a 3D harmonic trap on the BEC (top) and BCS (bottom) side. The polarization decreases from left to right. In the prepared samples with lower polarization, superfluid vortices can be observed arranging into an Abrikosov lattice. Adapted from [187].

that, using a harmonic trapping potential, imbalanced 3D Fermi gases phase-separate: While the core is a balanced superfluid, the excess majority is pushed out into a spin-imbalanced Fermi gas in the normal phase. Inside the balanced core, the Ketterle group observed vortices arranging themselves into the famous Abrikosov lattice after rotating the sample (see Fig. 8.3), a hallmark of superfluidity.

In follow-up studies, the polarization vs. temperature phase diagram was extracted at unitarity, as shown in Fig. 8.4 [13], demonstrating that a $T \neq 0$ superfluid can support a limited amount of excess majority as excitations on top of the superfluid. At the border between these regions, the polarization jumps, therefore making it a first-order phase transition (see Fig. 8.5). Additionally, a triple point exists at $T \approx 0.06\,T_{\mathrm{F}}$, above which the first-order phase transition changes to second order. These observations are in line with mean-field predictions [174], where a phase separation is predicted for $T = 0$, as well as a triple point at a finite T.

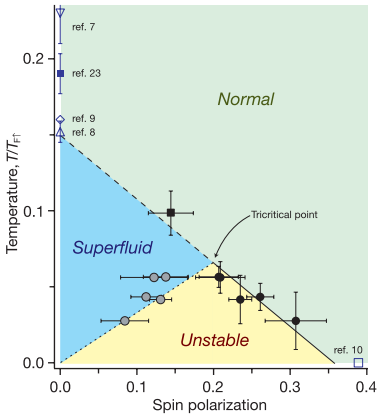


Figure 8.4: Phase diagram extracted from density profiles in a 3D harmonic trap. For $0 < T < T_c$, the superfluid is able to support a local imbalance up to $P \approx 0.2$. There exists a tricritical point at $T \approx 0.06\,T_{\mathrm{F}}$, below which the superfluid and normal gas are separated via a first-order phase transition, signaled by a jump in polarization that is also shown in Fig. 8.5. Adapted from [13]

8.2.2 2D Fermi gases

While 3D imbalanced Fermi gases have been extensively studied experimentally, the picture is much more restricted in the two-dimensional case. So far, only two experimental studies of imbalanced 2D Fermi gases have been reported. The first was performed in the group of J. Thomas [14], where the atoms are trapped in multiple 2D layers of a 1D standing-wave lattice. This system is in the intermediate 2D-regime as the Fermi energy is on the order of $\hbar\omega_z$. Their main observation was that, within this system, critical ordering into a more balanced core and imbalanced gas outside occurred, similar to the experiments on the 3D systems, but without a jump in polarization. This feature was particularly pronounced at strong interactions towards the BCS regime, where the core remained fully balanced be-

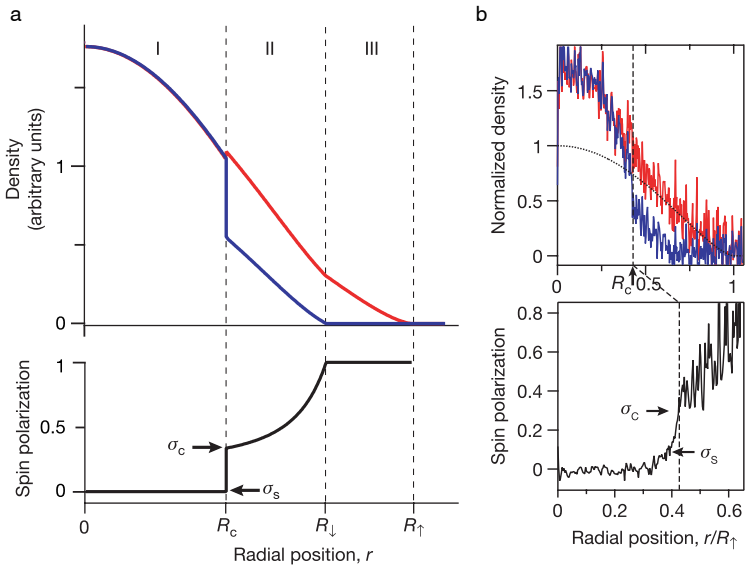


Figure 8.5: Observed phase separation in a 3D harmonic trap. a) The density profile can be divided into three regions, depending on the radial density profiles of the majority (red) and minority (blue). Going from the center outwards, we find: I) A balanced superfluid. II) An imbalanced Fermi gas in the normal phase. III) A fully polarized Fermi gas. The polarization jumps on the I–II boundary (lower panel), signaling a first-order phase transition. b) Experimental data, showing the expected behavior from a. Adapted from [13].

low a critical global polarization. The absence of a jump in polarization is unsurprising since the temperatures were at $0.2\,T_\mathrm{F}$ (with the T_F from the majority), which is above the point where phase separation is predicted to exist [196, 197] (further discussed in Ch. 8.3).

The second experiment was performed by the group of W. Bakr [15], which used a similar standing-wave lattice to trap atoms in a 2D geometry. The main difference from the previous experiment is that they load only a single layer here, and E_F is smaller than $\hbar\omega_z$, thereby entering the actual 2D regime. Additionally, they reach temperatures as low as $0.08\,T_\mathrm{F}$, which is comparable to the superfluid critical temperature in 2D [73]. The observations are similar to those of the previously discussed experiment, showing critical ordering into a balanced core at the center and an imbalanced region farther out (Fig. 8.6). Again, they observed that at strong interactions, the core remains fully balanced below a critical global polarization. Furthermore, they reported a bimodal minority distribution after a relatively short time-of-flight at finite imbalance, yet not at zero imbalance. This is consistent with, though not definitive for, condensation. Previous experiments have shown that systems above the critical temperature can also exhibit a bimodal momentum distribution up to $0.5\,T_\mathrm{F}$ [73].

As of now, numerous unanswered questions remain regarding imbalanced 2D Fermi gases, starting with whether they are indeed superfluid. Second, it is unclear whether the phase transition becomes first-order below a specific critical temperature. Current theory predictions estimate that the phase-separated region in 2D reaches up to $T \approx 0.2\,T_\mathrm{F}$ [197], yet no phase separation was observed in [15]. However, it is unclear whether the theoretical predictions are accurate due to the difficulty of incorporating quantum fluctuations, which become highly relevant in 2D. This might also be the reason why the predicted tricritical point in 2D of up to $T \approx 0.2\,T_\mathrm{F}$ [197] is much higher than the

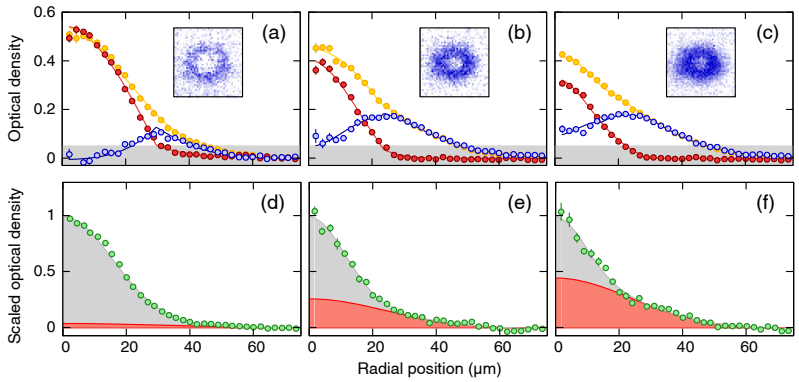


Figure 8.6: Radial density profiles of the majority (yellow) and minority (red) in the 2D harmonic trap. From a-c, the global polarizations are $P = 0.25, 0.55, 0.75$. Similar to the 3D density profiles shown in Fig. 8.5, the core is balanced for polarizations $P \leq 0.55$, pushing the excess majority outwards. However, there is no jump in local polarization (blue). The same is observed in the in situ polarizations (insets). A bimodal momentum distribution is evident in the time-of-flight density images (d-f). Adapted from [15].

observed tricritical point in 3D of $T_{\mathrm{TP}} \approx 0.06\,T_{\mathrm{F}}$. Lastly, exotic phases, such as the FFLO phase, are expected to be favored in 2D geometries, albeit at temperatures $T \lesssim 0.03\,T_{\mathrm{F}}$ [198].

Therefore, further quantum simulations are urgently needed. Ideally, they should explore lower temperatures and be sensitive to the presence of a first-order phase separation, probe superfluidity, and possibly also more exotic phases. In Ch. 9, I will present experiments where we have reduced the temperature substantially and work in box potentials for the first time. Here, a first-order transition should manifest itself as a sharp jump in polarization and the formation of phase-separated domains. The nearly homogeneous trap potential should also facilitate the study of more exotic phases, which are expected to exist only in a small parameter range and would therefore be obscured in harmonically trapped systems.

As we will see in Ch. 9, we do not observe any signs of a first-order phase separation or of a FFLO phase, most likely because, as of now, the temperatures in the experiment are too high at the required polarizations. We do, however, find indications of superfluidity, both by observing coherent oscillations of the condensate via trap-modulation spectroscopy and by creating long-lived vortices.

Before discussing our experimental observations, however, we first focus on the predicted phase diagram in the following sections.

8.3 Phase diagram of 2D imbalanced Fermi gases

There are three independent parameters that fully determine which phase the 2D imbalanced Fermi gas is in: The polarization $P = (n_\uparrow - n_\downarrow)/(n_\uparrow + n_\downarrow)$, the interactions characterized by $E_{\mathrm{B}}/E_{\mathrm{F}}$, and the temperature T/T_{F}. It is therefore instructive to fix one of the 3 axes while varying the other two to explore the phase diagram, which we will do in the following chapters. First, we consider the $T = 0$ scenario, after which we keep the interactions fixed in the BCS regime and vary the temperature instead.

An overview of this discussion is presented in the theoretically predicted phase diagrams depicted in Fig. 8.7. At zero temperature,

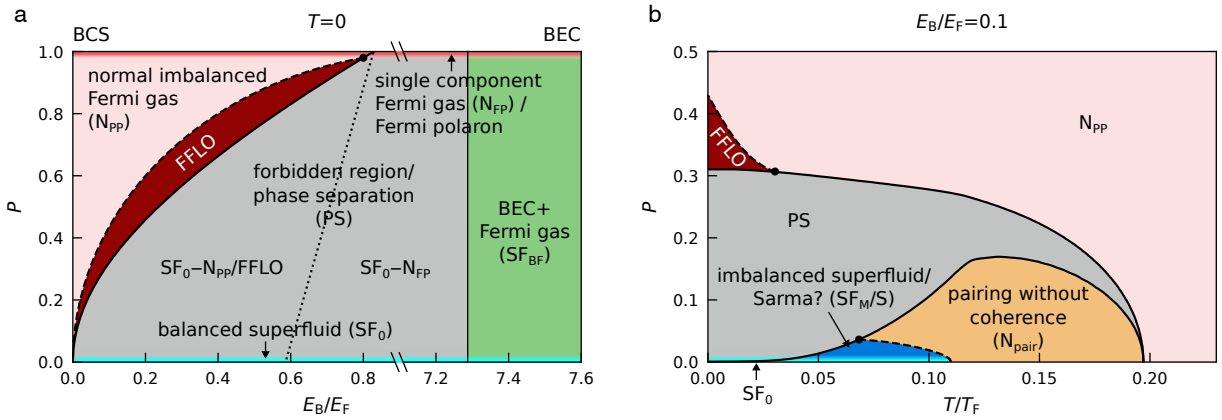


Figure 8.7: Overview of the 2D imbalanced Fermi gas phase diagram predicted by theory. First-order phase transitions are denoted with solid lines, while dashed lines are used for second or higher orders. a) Polarization vs. interaction phase diagram at zero temperature. It is dominated by a forbidden phase-separated region, in which the system splits into a balanced superfluid (SF_0) located on the x-axis and either the normal (N) or, potentially, the FFLO phase. On the BEC side, the FFLO and partially polarized normal phase (N_{PP}) disappear, leading to a SF_0–N_{FP} phase separation, where N_{FP} is the fully polarized Fermi gas, located at $P = 1$, on the upper x-axis. Far in the BEC regime, the fully polarized Fermi gas and the BEC become miscible, allowing a local imbalance on top of the superfluid (SF_{BF}). Additionally, in the almost-fully-polarized regime, we find the Fermi-polaron picture. b) Polarization vs. temperature phase diagram at fixed interactions on the BCS side. Most notably, the SF_0 superfluid allows a small imbalance in the form of thermal excitations, leading to the imbalanced superfluid (SF_M), or, potentially, the Sarma phase (S). At higher temperatures, the BKT mechanism leads to the breakdown of coherence while the fermions remain paired (N_{pair}). These phases are separated from the N_{PP} and FFLO phases by a forbidden region. Both phase diagrams are a summary of the predictions presented in [197–201]

we see that, for a broad range of interactions and polarizations $P > 0$, phase separation (PS) into a balanced superfluid (SF_0) and either a normal polarized (partially polarized N_{PP} or fully polarized N_{FP}) gas or the FFLO state manifests. This separation always constitutes a first-order transition. Generally, the only phases that allow superfluidity with an imbalance present are the FFLO state, which extends from the strongly interacting to the BCS regime, and a miscible Bose-Fermi mixture far on the BEC side (SF_{BF}), consisting of condensed bosonic dimers and non-condensed fermions from the excess majority. Additionally, the BCS regime is more susceptible to spin imbalances because it relies on pairing in momentum space, and superfluidity breaks down at lower polarizations. This $T = 0$ phase diagram is composed of a combination of different predictions [199–201], closely following the discussion in [59].

When fixing interactions in the BCS regime and varying the temperature instead (Fig. 8.7b), we see that the conventional superfluid phase, which was restricted to $P = 0$ in the $T = 0$ case, now allows a small imbalance to persist [196, 197]. This excess majority exists as thermal excitations "on top" of the superfluid. Within this SF_M region, there may be a second-order transition to the Sarma phase (S).

Another noteworthy observation is that the FFLO phase is stable only at low temperatures in the BCS regime. However, as we will discuss below, the region for the FFLO phase is an educated guess by mapping the $T = 0$ region at $E_B/E_F = 0.1$ to the y-axis of the temperature phase diagram, and placing a tricritical point at $T_{FFLO} \approx 0.03\,T_F$, where theory predicts the FFLO state to become unstable [198].

Comparing this to the phase diagram measured in 3D (Fig. 8.4), we can see that the tricritical point that borders the PS, SF_M and N_{PP} region now lies below the PS region and borders the pairing without coherence phase (N_{pair}) instead of N_{PP}. The phase-separated region extends to relatively high temperatures and then returns to $P = 0$ at temperatures just below $0.2\,T_F$, where it vanishes. Interestingly, the second experiment discussed in Ch. 8.2.2 reached $T = 0.08\,T_F$ at

various polarizations, where a phase separation is predicted, but no jump in polarization was observed.

Therefore, the predicted phase diagram is likely inaccurate, since theoretical descriptions are difficult due to the relevance of quantum fluctuations in 2D, which are not captured by mean-field theories, and are challenging to account for in beyond-mean-field calculations.

8.3.1 $T = 0$ phase diagram

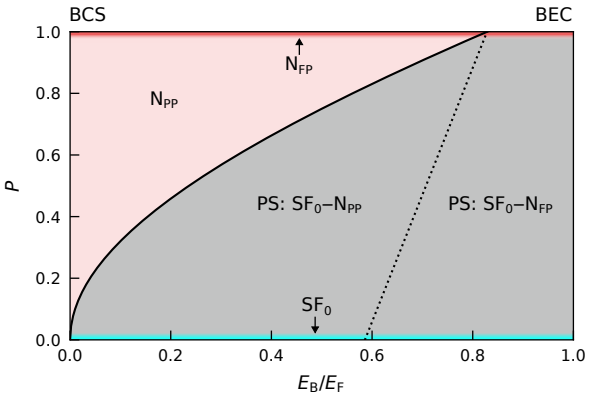


Figure 8.8: Mean-field phase diagram at $T = 0$ as predicted by [200]. The balanced superfluid (SF_0) is located at $P = 0$ on the x-axis. For polarizations between $0 < P < P_c$, the system phase separates into SF_0 and the normal phase. Depending on the interactions, the normal phase is either partially polarized (NPP) or fully polarized (NFP).

We start by first discussing the phase diagram at $T = 0$, ignoring exotic phases for now. A BCS-Leggett mean-field prediction was given by He et al. [200], which is shown in Fig. 8.8. The main observation here is that at $T = 0$, the superfluid phase (SF_0) never allows an imbalance to be present. We can see this because the SF_0 phase is restricted to the x-axis at $P = 0$. Once we introduce a finite polarization, the system phase-separates into a balanced superfluid (SF_0) and a polarized gas in the normal phase, as indicated by the phase-separated region (PS). Above a critical polarization, superfluidity fully breaks down, and the entire system enters the normal phase, as indicated by the solid line. Depending on the interactions, this polarized normal phase is either partially (N_{PP}) or fully (N_{FP}) polarized. The regions for a SF_0–N_{PP} and SF_0–N_{FP} phase separation are divided by the dotted line. In a homogeneous system, this would lead to SF_0 and N domains with constant P or superfluid bubbles. Since the phase-separated region can be interpreted as forbidden, the polarization is expected to jump at the domain boundaries, making it a first-order phase transition. More precisely, this jump would be from $P = 0$ to a point on the P_c line, with both domains being homogeneous (constant P).

However, this phase diagram is not the full story, as another phase can enter far in the BEC regime. Here, the system can be regarded as a Bose-Fermi mixture, since the paired fermions are deeply bound as dimers and effectively behave like bosons. For the unpaired fermions and the BEC to mix, the miscibility condition has to be fulfilled [199]:

$$\alpha g_{\mathrm{dd}} - g_{\mathrm{da}}^2 > 0 \,, \tag{8.1}$$

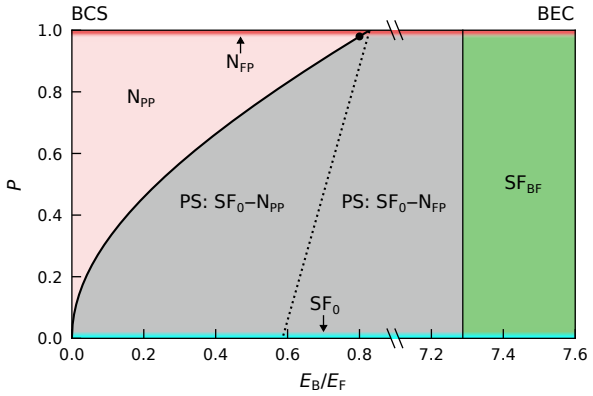


Figure 8.9: $T = 0$ phase diagram from[200], including the mixed phase SF_{BF} between a BEC of tightly bound bosonic dimers and excess majority fermions from [199]. This phase occurs very far in the weakly interacting BEC regime and does not depend on polarization.

where $\alpha = 2\pi\hbar^2/m$. The dimer-dimer and dimer-atom interaction parameters are defined as

$$g_{\mathrm{dd}} = \frac{\hbar}{m_{\mathrm{d}}} \frac{-4\pi}{\ln(k_{\mathrm{F}}^2 a_{\mathrm{dd}}^2) - \ln(4\pi)} \tag{8.2}$$

$$g_{\mathrm{ad}} = \frac{\hbar}{m_{\mu}} \frac{-2\pi}{\ln(k_{\mathrm{F}}^2 a_{\mathrm{da}}^2) - \ln(4\pi)} \,, \tag{8.3}$$

with the reduced mass $m_{\mu} = 2m/3$. Here, we use exact solutions $a_{\mathrm{dd}} = 0.55 a_{2\mathrm{D}}$ [40, 202] and $a_{\mathrm{da}} = 1.26 a_{2\mathrm{D}}$ [203] for the dimer-dimer and atom-dimer scattering lengths, respectively. Plugging everything into Eq. (8.1), we find that the miscibility condition is fulfilled for $E_{\mathrm{B}}/E_{\mathrm{F}} > 7.28$. Since this criterion is independent of the polarization, the phase transition corresponds to a vertical line in the diagram, as shown in Fig 8.9.

8.3.2 $T \neq 0$ predictions

We now introduce finite temperatures, allowing us to access the full parameter range that can be explored experimentally. We follow the description of Tempere et al., who calculated the P $(\delta n/n)$ vs. T vs. $E_{\mathrm{B}}/E_{\mathrm{F}}$ phase diagram using a functional-integral method. They included phase fluctuations via a hydrodynamic action functional [196] and, in a follow-up, expanded the theory to include amplitude fluctuations [197]. We first consider a P vs. T phase diagram at fixed interactions in the BCS regime, shown in Fig. 8.10a. Consistent with the $T = 0$ phase diagram, we see that on the y-axis, where $T = 0$, a SF_0–N_{PP} phase separation appears for any polarization $0 < P < P_c$. However, most notably, once the temperature increases, the superfluid is able to support a small imbalance up to $P \approx 0.04$ at $T \approx 0.07\, T_{\mathrm{F}}$, which we call the magnetized superfluid phase SF_{M}.

Starting from the SF_{M} phase, as the temperature increases further, we reach the BKT limit, where vortices unbind, and superfluidity breaks down. Pairing still occurs since $\Delta > 0$, but the phase fluctuations destroy the algebraic phase coherence, leaving us in the "pairing without coherence" (N_{pair}) phase. Unlike the first-order phase transi-

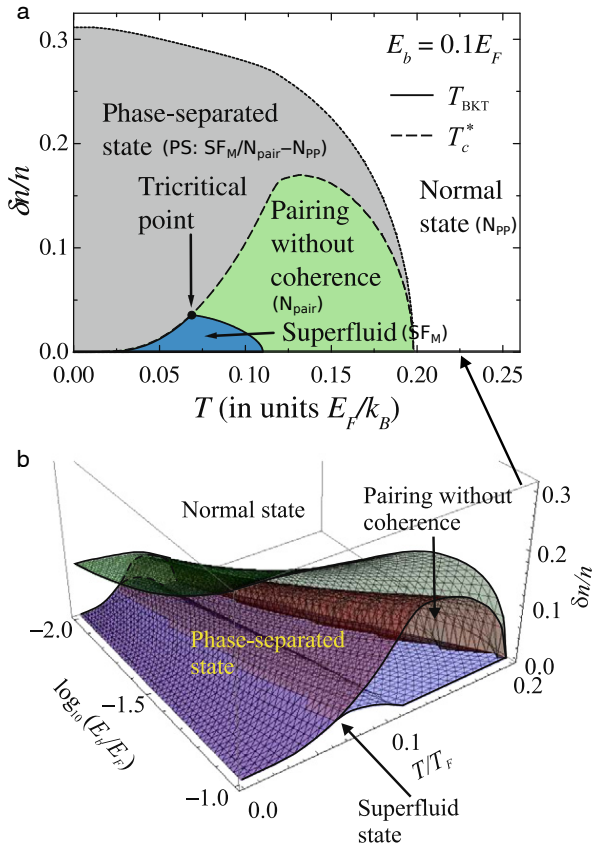


Figure 8.10: Phase diagram including the T-axis. a) At fixed interactions ($E_B/E_F = 0.1$) in the BCS regime, we see that the superfluid phase SF_M allows a local imbalance to exist for $T > 0$. Above the superfluid critical temperature, superfluidity breaks down, while fermions are still paired (N_{pair}). Both phases are phase-separated from the unpaired normal state N_{PP}. b) When changing interactions, we can see that towards the BCS regime, superfluidity is suppressed, consistent with the $T = 0$ phase diagram shown in Fig. 8.9. Adapted from [197].

tion that occurs when preparing a system with a global imbalance in the forbidden phase-separated region, the BKT transition into pairing without coherence is of infinite order, as explained in Ch. 3.4. Additionally, a tricritical point exists that, at higher temperatures, leads to an N_{PP}–N_{pair} rather than an N_{PP}–SF_M phase separation.

If we add the interaction axis again, we can see that the phase diagram shown in Fig. 8.10b does not change qualitatively for the range of interactions considered. The main observation is that, when moving from the BEC to the BCS side, all phase transitions move to lower polarizations and temperatures, increasing the size of the unpaired normal state, consistent with the $T = 0$ phase diagram in Fig. 8.9.

Comparing the P vs. T phase diagram with previous observations from 3D experiments (Fig. 8.4), we see two main differences: First, due to the BKT mechanism, the 2D system exhibits an incoherent phase where fermions are still paired. Second, the phase-separated region encloses the two paired phases (SF_M and N_{pair}), by reaching down to $P = 0$ at $T/T_F \approx 0.2$ instead of vanishing at a tricritical point. However, as mentioned before, these predictions should be taken with a grain of salt due to quantum fluctuations, which are difficult to account for.

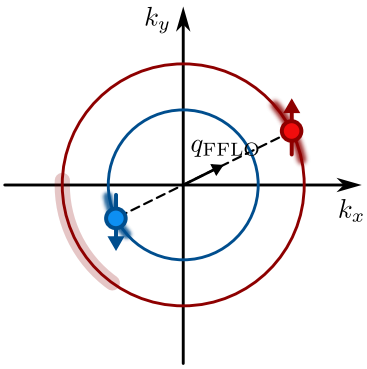


Figure 8.11: Pairing mechanism in the FFLO state. Fermions still pair on opposite sites on their Fermi surfaces as indicated by the dashed lines, although the region in which pairing occurs is much smaller (blurred regions). Due to the different sizes of the surfaces, this leads to a non-zero pair momentum q_{FFLO}. The total momentum of the system remains zero, since unpaired majority atoms occupy states on the opposite side of the Fermi surface (red shaded region).

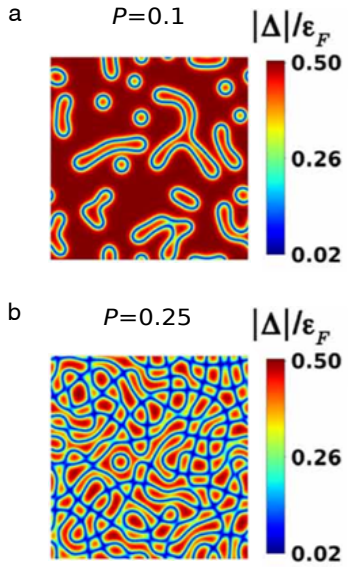


Figure 8.12: Simulated spatial variation of the superfluid order parameter in the FFLO phase. a) At low polarizations, rings of low order parameter values form. Here the system is locally imbalanced. b) At higher polarizations, a spatially modulating structure emerges, with the characteristic length scale $1/q_{\mathrm{FFLO}}$. Figures adapted from [198].

8.3.3 Exotic phases

Apart from the previously discussed phases, in which a magnetized superfluid exists only as a Bose-Fermi mixture far on the BEC side, or with the help of thermal excitations of the majority, there are less intuitive phases that allow spin-imbalanced superfluids. These phases include the FFLO, Sarma, deformed Fermi-surface, and FFLO phases, which will be discussed below. As we will see, only the Sarma and FFLO phases might exist in the 2D phase diagram, with the FFLO phase being the only stable one at $T = 0$.

FFLO

The most prominent phase that allows for a spin-imbalanced superfluid is the FFLO phase, named after Fulde, Ferrell, Larkin, and Ovchinnikov, who independently predicted it [175, 176]. Its defining feature is that the pairs carry non-zero total momentum $q_{\mathrm{FFLO}} = k_{\mathrm{F},\uparrow} - k_{\mathrm{F},\downarrow} \neq 0$. A sketch of the pairing mechanism is shown in Fig. 8.11. Here, pairing still happens on opposite sites, but the region where pairing occurs is much smaller due to energy and momentum conservation that are much more restrictive for the finite q_{FFLO}. The global momentum of the entire system is still zero, as unpaired majority atoms occupy the opposite side of the Fermi surface, as illustrated by the red-shaded region. For some parameters, unpaired minority atoms can also occupy momentum states on the side of the minority Fermi surface where no pairing is taking place.

A consequence of the non-zero momentum pairing is that the spatial symmetry is broken, and the superfluid order parameter Δ and polarization locally oscillate at a length scale given by $1/q_{\mathrm{FFLO}}$. Therefore, the FFLO state bears similarities to supersolids and is at times also referred to as such [204]. Recent numerical simulations by Tüzemen et al. have shown what the emerging patterns may look like (see Fig. 8.12). In their simulation, they find that the FFLO phase is stable for temperatures up to $T_{\mathrm{FFLO}} = 0.03\,T_{\mathrm{F}}$.

Additionally, a $T = 0$ mean-field calculation by Sheehy et al. [201] provides a region in which the FFLO phase might be stable. Adding this to the previous $T = 0$ prediction (Fig. 8.8), yields the phase diagram shown in Fig. 8.13. Here, we see that the FFLO phase exists in a narrow region along the boundary between the phase-separated region and the $\mathrm{N_{PP}}$ phase. The phase transition to the normal phase is of second order. It has to be noted, however, that the confinement-induced bound state in 2D may destabilize the FFLO phase as soon as E_{B} becomes comparable to E_{F}, and the tricritical point where the FFLO phase vanishes might be shifted further towards lower $E_{\mathrm{B}}/E_{\mathrm{F}}$.

Unfortunately, there is no comprehensive study at non-zero temperature which would allow us to place the FFLO state in the P vs. T phase diagram. However, using estimates from previous studies [198], we can speculate that the FFLO phase is present until $T_{\mathrm{FFLO}} \approx 0.03\,T_{\mathrm{F}}$. Mapping the $T = 0$ prediction at $E_{\mathrm{B}}/E_{\mathrm{F}} = 0.1$ from [201]

to the y-axis ($T = 0$) in the P vs. T phase diagram leads to the diagram at the beginning (Fig. 8.7b). One should note, however, that a reliable estimate of whether the FFLO phase is stable should go well beyond the mean-field approximation and also include a consideration of the aforementioned confinement-induced bound state. An alternative theoretical study to the ones discussed here suggests that the FFLO phase may be generally unstable for $T > 0$ in homogeneous 2D systems [205].

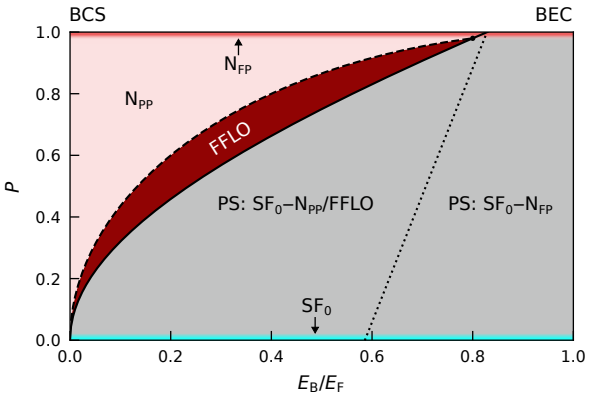


Figure 8.13: $T = 0$ phase diagram including the mean-field prediction of the FFLO state. It is located in a narrow region between the phase-separated and N_{PP} regions, extending far into the BCS side.

To date, the FFLO phase remains elusive; only indirect measurements in solid-state systems have revealed signatures [183], but a direct observation remains elusive. In the context of quantum gas experiments, this is not surprising; The FFLO phase is expected to be unstable towards phase separation in 3D systems, and, as discussed in Ch. 8.2.2, studies of 2D imbalanced systems are limited and were always performed at temperatures $T \geq 0.1\,T_F$, far above T_{FFLO}. Additionally, all previous experiments were performed in harmonic traps, where different distances from the trap center correspond to different values of the P axis in the phase diagram. Since the FFLO phase only exists in a small parameter space, it would manifest on a slim shell surrounding the superfluid core, making detection practically impossible.

As we will see in the next chapter, our experiment reaches temperatures slightly above T_{FFLO}. However, we did not observe any typical precursors (e.g., mode softening in the momentum-resolved spectrum) of the FFLO phase, most likely because those temperatures are still too high.

Sarma

The Sarma phase, predicted by Sarma et al. [177], may be understood analogously to a phase separation but in momentum space. It is a direct consequence of the single particle excitation spectrum E_k of the BCS state, introduced in Ch. 3.2. The imbalance introduces a shift h in the chemical potentials between the minority and majority, which directly carries over to the single-particle excitation spectrum E_k. As soon as $h > \Delta$, the majority energy $E_{\uparrow,k}$ has a region centered around

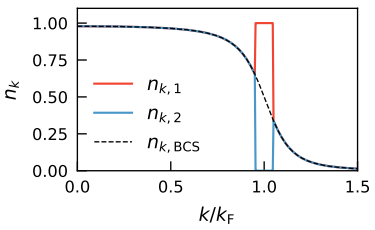


Figure 8.14: Occupation of the momentum states in the Sarma phase with majority $|1\rangle$ and minority $|2\rangle$. The momentum states centered around the Fermi momentum are fully occupied by the majority but fully vacant for the minority.

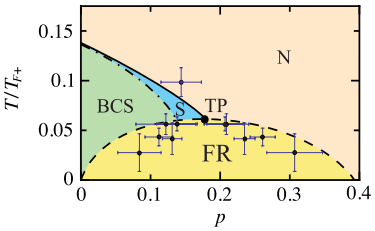


Figure 8.15: P vs. T phase diagram for a 3D imbalanced Fermi gas. It is an extension of the experimentally obtained one, previously shown in Fig. 8.4, including the experimental points. Here, the superfluid phase is divided into a BCS and Sarma (S) region. Adapted from [174].

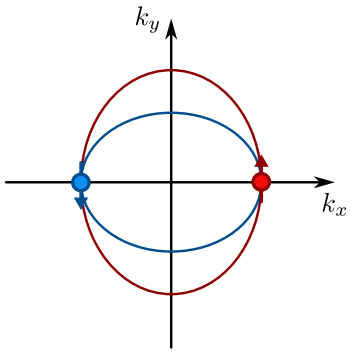


Figure 8.16: Deformed Fermi surfaces. Both Fermi surfaces get elongated along two orthogonal directions, such that two opposite sides overlap again and a pairing at zero total pair momentum becomes possible. In 3D, this example would be rotationally symmetric about the k_x-axis.

k_F, where it becomes negative. As a consequence, the momentum distribution is fully polarized for all k, where $E_{\uparrow,k} < 0$. Since pairing occurs directly above and below this region, this phase is also called the "breached pair" or, less commonly, "interior gap" phase.

In the $T = 0$ scenario, however, this phase is always unstable towards phase-separation, no matter the dimensionality. Once $T > 0$, this can change, as can be seen in predictions for the 3D phase diagram, shown in Fig. 8.15: The $\mathrm{SF_M}$ region is divided into two distinct phases that are separated via a second-order transition. For low polarizations, a gapped BCS state exists. Increasing P, however, eventually leads to $h > \Delta$ and the Sarma phase (S) becomes stable. Since no paper in 2D discusses the difference between the Sarma and BCS phase, it is unclear whether the $\mathrm{SF_M}$ region is in the BCS or Sarma phase, or whether a similar crossover as in the 3D case occurs. We note that it is experimentally challenging to distinguish between a Sarma and a BCS phase, since both are spatially homogeneous, with the main difference manifesting in the momentum distribution. As shown in Fig. 8.4, previous experiments do not specify which magnetized superfluid phase their system is in, and as of now, a signature of the Sarma phase has not been observed.

Deformed Fermi surface

Another phase that allows for an imbalanced superfluid is one in which the Fermi surfaces deviate from their usual radially symmetric shape, taking an elliptical form, and was proposed by Sedrakian et al. [178, 179]. Both Fermi surfaces elongate in orthogonal directions, as illustrated in Fig. 8.16. This allows the surfaces to overlap again in a small region where pairing can then take place.

The stability of this phase, however, is still debated. One of the original papers [179] compared the free energy under BCS and FFLO theories, concluding that the region of stability is larger than that of the FFLO state. More recent mean-field studies, however, have found lower free energies for the FFLO phase [201], and we disregard this phase for the rest of the discussion.

9 REALIZATION OF AN IMBALANCED FERMI SUPERFLUID IN A HOMOGENEOUS 2D GEOMETRY

Creating cold Fermi gases with imbalances is an experimentally challenging endeavor. This chapter discusses how we managed to reach temperatures below the superfluid critical temperature for the first time, a factor of two to three lower than in previous experiments on 2D imbalanced Fermi gases [15]. Contrary to theoretical predictions, we do not observe phase separation but find superfluid behavior well into the strongly interacting regime when probing collective excitations of the condensate via trap-modulation spectroscopy. The outline of this chapter is as follows: First, in Ch. 9.1, we focus on the preparation scheme that allows us to create imbalances with selected polarizations of up to $P = 0.2$, while staying at temperatures below $0.06\,T_{\mathrm{F}}$. The following chapters will then characterize the prepared systems by first focusing on the in-situ density distributions in Chapter 10.1. In the homogeneous case, phase separation does not occur, but critical ordering can be induced by adding a harmonic confinement at the center of the trap, replicating observations from previous experiments [14, 15]. Finally, Ch. 10.2 focuses on the order parameter dynamics, showing that the system is superfluid from the BEC to the strongly interacting regime, but breaks down on the BCS side as a result of the imbalance.

9.1 Creation of a cold imbalanced 2D Fermi gas

9.1.1 Comparison of different approaches

Key to our experiments was the ability to create imbalanced 2D gases that are a factor of two to three colder than previously achieved, allowing us to go well below the critical temperature for balanced superfluids. This has become possible by testing different preparation strategies and then carefully optimizing the most promising one. The following discussion is aimed at experimentalists with a special interest in the preparation rather than a general audience, which is referred to in Ch. 9.1.2, that explains the preparation sequence used in the experiment.

Spin selective spilling via a magnetic field gradient

A relatively straightforward way to create an imbalance is to use a magnetic field gradient, which selectively applies a force to only one spin component of the mixture. This gradient tilts the trapping potential, leading to spilling as illustrated in Fig. 9.1b. Since the atoms

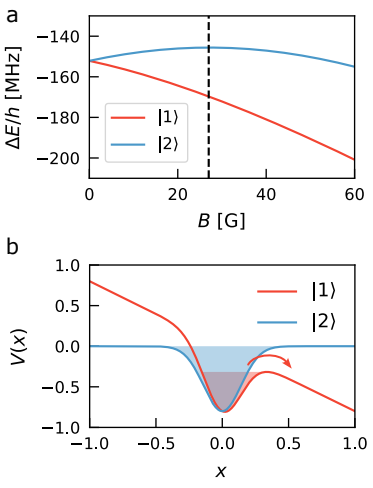


Figure 9.1: a) Zeeman shift of the lowest two hyperfine states of ^{6}Li at low magnetic fields. At 27 G (dashed line), state $|2\rangle$ has an energy maximum. b) Trapping potentials when applying a magnetic field gradient in addition to an optical dipole trap at 27 G. Only state $|1\rangle$ spills, thus creating an imbalance.

with the highest energy are removed from the system, this also has the convenient side effect of keeping the mixture cold. This technique was used in [206] to create an imbalance in a 2D Fermi-Hubbard system.

To achieve this state-dependent gradient, let us take a look at the energies vs. magnetic fields for the different hyperfine levels of ^{6}Li, calculated from the Breit-Rabi formula in Fig. 9.1a. We can see that states $|1\rangle = |F = 1/2, m_F = 1/2\rangle$ and $|2\rangle = |F = 1/2, m_F = -1/2\rangle$ perfectly fulfill the requirements for this technique at a field of 27 G: While $|2\rangle$ has an energy maximum and will therefore be unaffected by a gradient, the energy for $|1\rangle$ changes, leading to a tilted trapping potential and selective spilling.

However, there is one major caveat: 27 G is far below the Feshbach resonance at 832 G, and the atoms are not yet bound in molecules, since losses to deeper-lying molecular states would be detrimental in this regime. This means that after creating the imbalanced system, we have to ramp across the Feshbach resonance to probe superfluid properties, which leads to losses and heating as the magnetic field approaches 832 G.

To make matters worse, the initial cooling must also be performed far below the Feshbach resonance, so that atoms cannot enter the molecular state before spin-selective spilling. This means that the largest scattering length that can be reached for evaporative cooling is around $-290\,a_0$ at 320 G, which is orders of magnitude lower than the interactions that can be reached on resonance.

Partial blowout of one spin state via an optical transition

A similarly straightforward approach is to use an optical transition and partially eject one spin species to achieve the desired polarization. While this technique can create an imbalance, it has two major drawbacks: first, it raises the system temperature to above T_c; second, the number of ejected atoms varies from shot to shot. We attribute these effects to the possibility that some atoms remain in the trap after a single photon absorption. These atoms then collide with other atoms in the mixture, thereby introducing heat.

Radio frequency transfer to third spin state with consecutive blowout

A more refined approach for an optical blowout exploits a third hyperfine state $|3\rangle = |F = 3/2, m_F = -3/2\rangle$. By addressing the $|2\rangle - |3\rangle$ transition, one can transfer a desired number of atoms into this third state and subsequently blow them out. This avoids the issues of the previously introduced technique, as all atoms addressed by the blowout are removed. This is the technique that we follow in this work.

There are a few things that have to be considered to minimize the heat introduced by this preparation:

1. The time between the transfer and blowout should be as short as possible, since having three species of fermions heavily increases three-body losses, which, apart from atom losses, heats the system.
2. Since the energies of adjacent hyperfine levels are relatively close (about 80 MHz for ^{6}Li close to the Feshbach resonance), during the blowout, atoms in $|1\rangle$ and $|2\rangle$ can also scatter photons. To lower the impact, the power of the blowout should be as low as possible, while still removing all atoms in $|3\rangle$.
3. The RF transition transfers atoms from anywhere in the Fermi sea to state $|3\rangle$, effectively increasing the entropy. After rethermalization, the system is hotter and, in most cases, needs further cooling.

Additionally, there are two ways to address the RF transition. One can use a resonant RF pulse, which leads to fast transfer but larger fluctuations in the atom number in $|2\rangle$. Alternatively, one can perform a Landau-Zener sweep, which is very stable with respect to atom number but takes an order of magnitude longer for the transfer. As a result, three-body collisions through decoherence can become a problem. In the end, the approach using a Landau-Zener sweep yielded the best results for our preparation and is discussed in detail in Ch. 9.1.2.

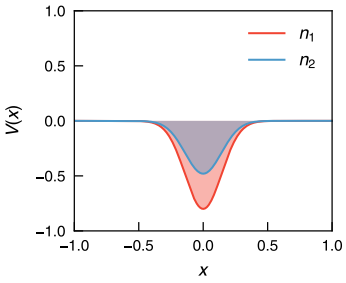


Figure 9.2: State dependent dipole potential for $|1\rangle$ and $|2\rangle$. By choosing a wavelength close to a transition, the potential of one of the spin states is shallower, leading to an imbalance (here $n_1 > n_2$). Heating is expected because the required wavelength is close to a transition.

Spin selective dipole trap

There is one more approach that is potentially suited for our experimental setup: Using a spin-selective dipole potential. In the simplest case, atoms can be loaded into an attractive dipole trap close to resonance, where both spin species experience significantly different trapping depths. When lowering the potential depth, species at shallower potentials are selectively evaporated to lower densities, creating an imbalance (see Fig. 9.2). Unfortunately, because the light needs to be near resonance, scattering processes are expected to rapidly heat the mixture to temperatures above T_c. However, in the specific trapping geometry used in the experiment, these effects might be mitigated.

One of the main features of our 2D box trap is that it uses only repulsive optical potentials, including the ring, which creates sharp walls for radial confinement. Overlapping this ring with a spin-selective beam lowers the potential barrier for one spin state (see Fig. 9.3). Spilling then creates an imbalance while preventing atoms from being directly exposed to light near resonance, thereby reducing scattering and subsequent heating. This technique has not been tested at the time of writing due to the required modifications to the experiment, but it remains a promising option for future experiments.

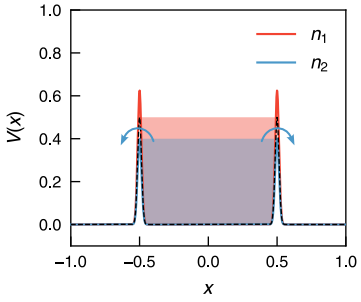


Figure 9.3: Creating an imbalance via a state-dependent ring. By overlapping the repulsive ring beam with a state-dependent beam, the potential can be selectively lowered for one spin state and raised for the other, leading to spilling. The heating from the overlapped beam is expected to be reduced because it is located in a region of negligible density, assuming a clean beam profile.

9.1.2 Creation of an imbalance via RF transitions

We now focus on the preparation technique that yielded the coldest and most consistent results for creating an imbalanced Fermi mixture of ^{6}Li in a 2D geometry. In detail, the preparation sequence of creating

an imbalance via an RF transfer and consecutive blowout looks as follows:

1. After the general preparation sequence explained in Ch. 4.2, we start with a balanced Fermi mixture of about 8×10^4 atoms in the squeeze trap at a power of 1 W. We ramp down the power exponentially in 1 s to perform evaporative cooling while ramping the magnetic field into the BEC regime (from 870 G to 750 G). The magnetic field ramp is performed to optimize the loading of atoms into the ring in the next step, as the pressure, and therefore the radius of the cloud, decreases for the BEC. The final power of the squeeze trap is set slightly below the point where the atoms start spilling from the trap, typically at around 20 mW. At the same time, a vertical magnetic field gradient is introduced to spill atoms to a desired density. This reduces the shot-to-shot fluctuations in atom numbers from $\sim$ 10 % to smaller than 5 %. Afterward, the power is ramped up to 60 mW in 200 ms to recompress the atoms for the next step.

2. We now have a cold Fermi mixture in a relatively small volume since we ramped the interactions to the BEC side. In this step, we load our atoms into the trapping geometry. This is done by first switching the ring trap to around 150 mW over 50 ms, thereby confining the atoms radially. To avoid three-body losses, which are enhanced on the BEC side, we ramp our field to the pole of the Feshbach resonance at 832 G in 200 ms, before switching on the accordion lattice for vertical confinement in 300 ms. Additionally, we keep the accordion at a large lattice spacing of $\sim$ 30 µm, ensuring consistent loading to a single layer. The transfer is completed by switching off the squeeze trap in 100 ms and consecutively ramping the accordion to its final power of 0.5 W in 50 ms.

3. In this step, the imbalance is created. The first step is to ramp the magnetic field to 1000 G far above the Feshbach resonance in 250 ms, thereby reducing interactions between the atoms. This will prevent heating later on. Now, a desired fraction of atoms is transferred from state $|2\rangle$ to state $|3\rangle$. The atoms in $|3\rangle$ are then blown out via a resonant light pulse through the microscope, leaving an imbalanced $|1\rangle - |2\rangle$ mixture.

4. Since the previous steps introduced heat into the system, re-evaporation is required. To increase interactions, we ramp the magnetic field back to 832 G in 1 s while compressing the accordion. For a more efficient evaporation, however, a different set of coils in Helmholtz configuration is used, meaning that the Feshbach coils are ramped off while the Helmholtz coils are ramped to the desired field. This leaves a weak anti-confinement stemming from the accordion trap, which is otherwise canceled out by the weak radial confinement of the Feshbach coils. Next, the ring power is exponentially reduced over 300 ms, and evaporative cooling takes place. This last ramp is crucial, as almost exclusively majority atoms are

evaporated due to the larger chemical potential, effectively rebalancing the system.

5. In a final step, the ring power is increased again, and the field is ramped back to the Feshbach coils in order to create a homogeneous system at the desired field for the final experiment, typically within a range from 750 G to 900 G.

In this preparation, the main contributor to the heat introduced into the system is the holes in the Fermi sea created during the Landau-Zener sweep in step 3. The consequence is a trade-off between polarization and temperature; however, the severity of the effect can be mitigated somewhat through meticulous optimization of key parameters.

The first one is the initial number of atoms loaded into the ring during step 1. Starting with too many atoms creates a significant number of holes in the Fermi sea, whereas starting with too few atoms means that no reevaporation can be performed in step 4. Additionally, the group of parameters surrounding the Landau-Zener sweep and reevaporation is equally important. Since the latter partially rebalances the system, a larger imbalance than the intended one must be created during the transfer. Lastly, the final ring power in which the experiment is performed is also a crucial quantity. We observed heating in our system when ramping it up to high power. We attribute this to heating, which can be induced by noise in the lasers creating repulsive potentials. We solve this problem by keeping the ring power barely above the point where the density in the ring is still constant over the full BEC-BCS crossover, such that hot atoms can escape the system.

After optimization of these parameters, we reach temperatures between 0.01 and $0.06\,T_\mathrm{F}$ for imbalances up to $P = 0.5$ (see Fig. 9.4), which, unlike in previous studies of imbalanced 2D Fermi gases, is below the critical temperature.

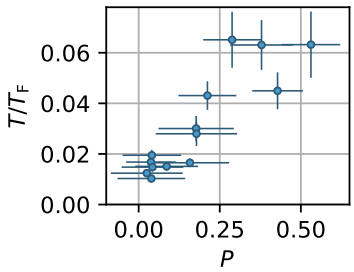


Figure 9.4: Temperatures achieved for varying polarizations by changing the sweep rate of the Landau-Zener sweep.

10 PROBING 2D IMBALANCED SUPERFLUIDS

In this chapter, I report on an investigation of imbalanced 2D Fermi gases, which is the second main result in this thesis. The procedure for preparing these gases was developed jointly by Hauke Biss, Cesar Cabrera, and me. The investigation of the in situ 2D profiles and trap-modulation spectroscopy was led by me, with strong contributions from Cesar Cabrera and Hauke Biss. The generation and observation of vortices in imbalanced gases was performed by Hans Leonard Michel, Artak Mkrtchyan, Moritz von Usslar, and Cesar Cabrera, with occasional support from me. The entire work was supervised by Cesar Cabrera and Henning Moritz.

The existence of spin-imbalanced Fermi superfluids is a central unresolved question for two-dimensional systems. These systems are of particular interest because, in contrast to three-dimensional systems where superfluidity has been observed in imbalanced Fermi gases (see Ch. 8.2.1), quantum fluctuations suppress superfluid order (see Ch. 3.4). While 3D experiments did not observe any signatures of exotic phases, theoretical predictions suggest that they may be favored in lower dimensions. This raises the question whether a spin-imbalanced 2D Fermi gas remains superfluid, exhibits first-order phase separation, or supports more exotic paired phases. Here, we study imbalanced 2D Fermi gases at unprecedentedly low temperatures ranging from 0.02 to $0.06\,T_\mathrm{F}$ and polarizations $0 \leq P \leq 0.43$ in a homogeneous box trap. We find no indication of first-order phase separation or spatially modulated superfluidity up to polarizations of $P = 0.22$ in the full BEC-BCS crossover. Applying the techniques of trap-modulation spectroscopy established for balanced gases (see Ch. 4.3.4), we observe dynamics consistent with the existence of a superfluid order parameter from the BEC regime well into the strongly interacting regime. Finally, supporting these findings, the team has observed long-lived vortices up to $P \sim 0.15$.

10.1 In situ density profiles

The ability to generate 2D gases featuring spin imbalance in a box potential is novel, since all previous work was performed in harmonic traps [14, 15]. Furthermore, we reach temperatures below $0.06\,T_\mathrm{F}$ up to polarizations of $P = 0.43$, allowing us to probe deeply within the region where theory predicts phase separation (see Ch. 8.3). Therefore, the first set of experiments focuses on in situ density profiles. This is done for two scenarios: first, within a homogeneous trapping geometry, where balanced superfluid regions are expected to form inside the phase-separated region of the phase diagram, and second, with an additional harmonic confinement that is gradually switched on. As we will see, the former surprisingly shows a (near) homogeneous

local polarization and therefore the lack of a phase separation for any investigated polarization and interaction. Introducing the harmonic confinement instead leads to a balanced core surrounded by an imbalanced region, connecting the results to previous observations [14, 15]. No jump in polarization is observed.

10.1.1 Homogeneous box

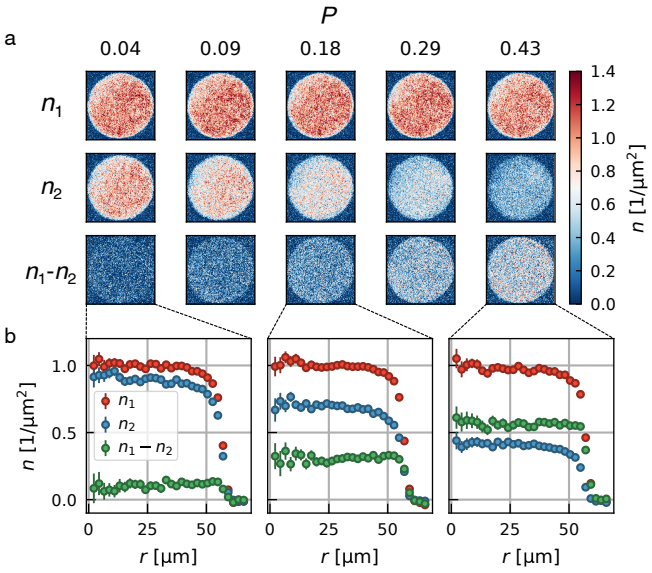


Figure 10.1: a) Averaged in situ images for an imbalanced system with varying polarization P, fixed at large interactions $\ln(k_F a_{2D}) = 1$. The local polarization is homogeneous throughout the system and equals P. b) Radial averages of the density profiles. The error bars represent twice the standard deviation. Due to the corresponding division by the square root of the number of pixels at a given radius, the slight azimuthal inhomogeneity does not manifest itself strongly.

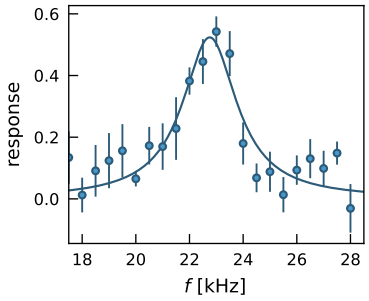


Figure 10.2: Calibration of the trap frequency ω_z via parametric heating into the second excited state of the transverse confinement. Via a Lorentzian fit, we extract f_2 to get $\omega_z = \pi f_2$.

For the homogeneous in situ density profiles, we use the same trapping geometry as in the experiments for the balanced system, explained in Ch. 4.2. During the experiments, the accordion lattice had a trap frequency of $\omega_z = 2\pi(11.38 \pm 0.13)$ kHz, as shown in Fig. 10.2, while we keep the density of the majority low enough that $E_F \leq 0.9\hbar\omega_z$ to stay in the 2D regime. The phase diagram can be explored by scanning two parameters: The interactions $\ln(k_F a_{2D})$ and the imbalance P.

First, we keep the interactions fixed at strong interactions ($\ln(k_F a_{2D}) = 1$) and scan the polarization by varying the density of the minority. The corresponding density profiles averaged over 10 shots are shown in Fig. 10.1. Surprisingly, we do not observe a phase separation for any set polarization P, even though some of the points are deep within the phase-separated region from the prediction[18] (see Fig. 8.7). Instead, the local polarization remains relatively homogeneous over the entire system, which is further underlined by the radial density profiles (Fig. 10.1b). This observation differs from previous studies on imbalanced Fermi gases in 2D [14, 15] that use harmonic trapping, where, at strong interactions, the center remains balanced.

When fixing the polarization at $P = 0.18$ and instead scanning the interactions, we see, in Fig. 10.3a, that in the entire crossover, there still is no phase separation. As a side note, far on the BEC side,

[18] The single-shot images look identical to the averaged images but feature more noise, also not showing any signs of phase separation, density modulation, or ordering.

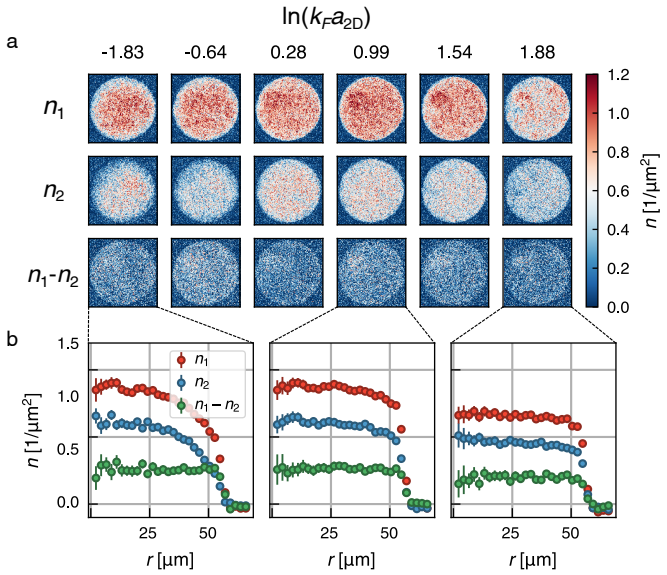


Figure 10.3: a) Averaged in situ images over 10 realizations for an imbalanced system at $P = 0.18$ at different interactions. At any interaction, the local polarization is homogeneous, and no phase separation is visible. b) Radial density profiles extracted from the same images underline this observation. On the BEC side, the weak confinement introduced by the magnetic field becomes visible because of the small chemical potential.

the system is not perfectly homogeneous, as the chemical potential becomes small and minor imperfections in the trapping potential become visible. The main contribution to the density deformations is the weak confinement introduced by the coils. This results in a higher density resting at the center of the trap, as shown in the first radial average in Fig. 10.3b. Even though this confinement should, in theory, provide a nucleation point for a balanced region to form, the radial average shows constant local imbalance over the entire system.

The previously discussed theoretical predictions, as well as the experiments performed, show that phase separation is expected, especially on the BEC side, where condensation is more robust. There are two possible explanations for this observation:

1. The system is not superfluid either throughout the crossover or only in the BCS regime.
2. The excess majority lives on top of the superfluid as thermal excitation. When considering the P vs. T phase diagram in Ch. 8.3, this is plausible, since the highest allowed polarizations for a superfluid state are expected to lie at the temperatures of the experiment ($T \approx 0.06\,T_\mathrm{F}$). Additionally, previous observations in 3D Fermi gases [13] have observed imbalances of up to $P = 0.14$ in the superfluid core at identical temperatures.

Before investigating superfluidity in Ch. 10.2 by measuring the superfluid order parameter dynamics, we examine the density profiles in the presence of an attractive potential.

10.1.2 Adding a tunable harmonic confinement

Since previous experiments on imbalanced Fermi gases were performed in harmonic traps, in which, contrary to our findings, ordering

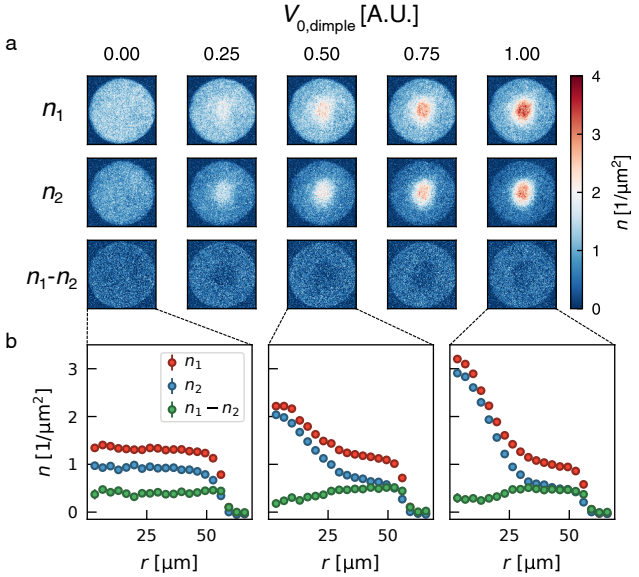


Figure 10.4: a) Averaged in situ images over 10 realizations of a system with a global imbalance of $P = 0.22 \pm 0.02$ versus increasing depths of an attractive potential in the center of the box trap. At low power, the system is locally imbalanced, whereas a balanced core forms at larger trapping depths. In the center, densities become so large that the system is no longer in the strict 2D limit. b) Radial averages show that for the largest depth, the core stays balanced within a region of radius $r = 16\,\mu\mathrm{m}$.

into balanced and imbalanced regions was observed [14, 15], we perform a complementary measurement to reproduce these findings and bridge the gap between homogeneous and harmonically confined systems. To achieve this, we place a Gaussian beam with a waist of 20 µm in the center of the ring, using an attractive wavelength of $\lambda = 780\,\mathrm{nm}$. We can continuously move from a homogeneous to a harmonic confinement by changing the power of this beam, resulting in the density profiles shown in Fig. 10.4a, at fixed interaction $\ln(k_\mathrm{F} a_\mathrm{2D}) = 0.5$ and polarization $P = (0.21 \pm 0.02)$. Starting from the homogeneous system, in which the local polarization remains nearly constant within the box, we see that the higher-density region at the center of the overlapping trap gradually becomes balanced as the power increases.

Additionally, for larger trap powers, the transition from the balanced core to the imbalanced gas is continuous, which can be seen in the radial averages in Fig. 10.4b. We note that for large dimple powers the densities increase beyond the 2D limit, such that $E_\mathrm{F}/\hbar\omega_z \approx 3$ at $V_{0,\mathrm{dimple}} = 1$. The conclusion from this measurement, assuming that the core is superfluid, is that, at least at $T = 0.05\,T_\mathrm{F}$, no first-order phase transition for imbalanced 2D Fermi gases exists. If a tricritical point exists, below which a first-order phase transition occurs, and the polarization jumps, it has to lie below the temperatures of the experiment. As previously discussed, in 3D systems, such a triple point exists at $T \approx 0.06\,T_\mathrm{F}$ [13], and theoretical predictions for 2D estimate a first-order transition up to $T = 0.2\,T_\mathrm{F}$ [197], which is above the temperatures in our experiment.

10.2 Observing superfluidity via order parameter dynamics

Up to this point, we have only examined the in situ density profiles, without probing any superfluid properties. However, as we have established in Ch. 5, trap modulation spectroscopy enables us to probe the dynamics of the superfluid order parameter and therefore test whether the system is indeed superfluid[19].

A trap modulation spectrum for a fixed polarization of $P = 0.13$ is shown in Fig. 10.5, where we scan the interactions from the BEC to the BCS side. On the BEC side, the coherent oscillations of the condensate are clearly visible, showing that the system is superfluid. This mode persists into the strongly correlated regime up until $\ln(k_\mathrm{F} a_\mathrm{2D}) = 0.9$, where, further towards the BCS regime, it vanishes and superfluidity appears to break down.

We excluded temperature-related effects by extracting the same trap modulation spectrum for a balanced system. Here we set the density for both spin states to that of the minority and controllably heat the experiment to $T = 0.06\,T_\mathrm{F}$, slightly above the temperature of the imbalanced system. The heating is performed by addressing the $2\hbar\omega_z$ excitation directly after the ring evaporation. The system then rethermalizes during a 250 ms ramp to the final magnetic field that sets the interactions for the spectrum.

In the balanced spectrum, the mode is visible throughout the entire BEC-BCS crossover, verifying that, indeed, the breakdown of superfluidity observed in the imbalanced system is induced by the imbalance itself.

[19] In earlier experiments, we initially tried to extract a critical velocity, similar to [6] via Bragg spectroscopy. However, as already presented in [59], this experimental technique is not suited to test whether an imbalanced Fermi gas is superfluid because the excess majority will exhibit the excitation spectrum of a single-component Fermi gas, overlapping with the excitation spectrum of the superfluid. This leads to excitations at low energies for non-zero momenta, resulting in a critical velocity $v_\mathrm{crit} = 0$, even in the presence of a superfluid.

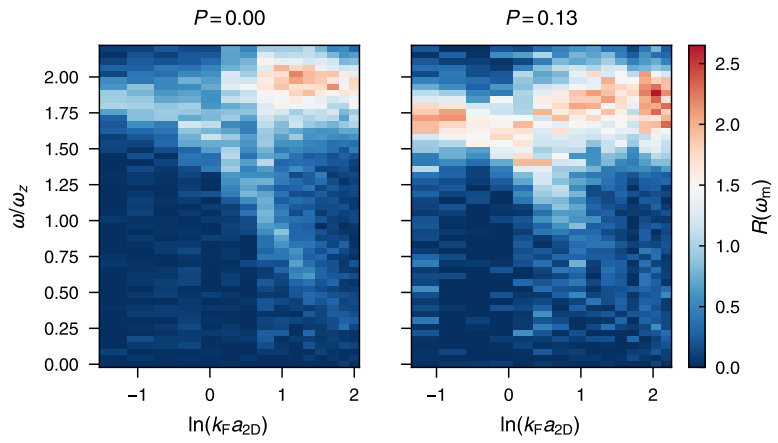


Figure 10.5: Trap modulation spectra for a balanced system (left) and a system with an imbalance of $P = 0.13$. The order-parameter mode of the balanced system is visible throughout the crossover. In contrast, it vanishes for $\ln(k_\mathrm{F} a_\mathrm{2D}) > 1$ in the imbalanced case.

10.3 Observing persistent vortices

In the latest experiments, we probe superfluid behavior by observing stable vortices. To deterministically create and pin the vortices, we use the technique pioneered by the Anderson group [207], in which two repulsive stirrers are dragged through the sample (see Fig. 10.6).

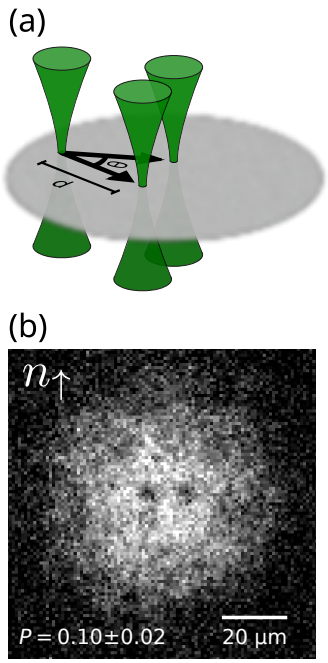


Figure 10.6: a) Deterministic creation of vortices by dragging two stirrers through the sample. b) Single-shot image of two pinned vortices at $P = 0.1$. Figures adapted from [208].

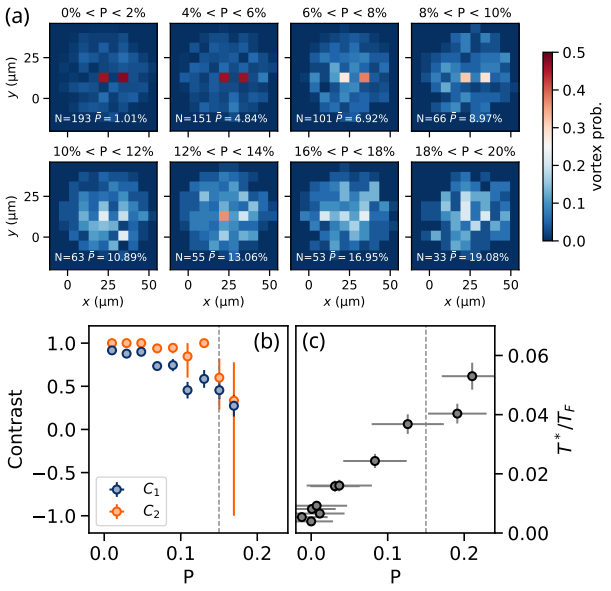
Using a digital mirror device (DMD), we project the stirrers onto the sample, starting from the same position and moving them apart at a set angle and velocity. Holding the stirrers in place after movement then allows us to pin the vortices created during the procedure.

Lastly, we slightly open the accordion lattice before imaging to increase the vortex core size. This ramp to 3D geometry is required because the size of the 2D vortex core is comparable to the mean interparticle distance, making it experimentally undetectable. To ensure the vortices have not been created during the ramp, we verify that none are observed in identical experimental cycles conducted at lower stirrer velocities.

For the main experiment, we choose a velocity fast enough to deterministically create vortices in the balanced case and use this configuration to probe systems with varying polarizations in the strongly interacting regime at $\ln(k_F a_{2D}) = 1$. As shown in Fig. 10.7a, we observe pinned vortices at low polarizations. Plotting the contrast in Fig. 10.7b, we can quantify that vortices can be created up to polarizations of at least $P = 0.15$. The two contrasts C_1 and C_2 correspond to a single vortex and a vortex pair at the pinned location, respectively. This is consistent with the trap-modulation measurements that also observed signs of superfluidity well into the strongly interacting regime at a polarization of $P = 0.13$.

We note that the temperatures T/T_F in this dataset are slightly lower than those in the studies presented in the previous sections due to higher densities and therefore T_F. This was possible due to an upgrade that increased the accordion trap frequency to 20 kHz from the previous 12 kHz, allowing us to remain in the 2D regime at higher densities.

Figure 10.7: a) Probabilities of finding a vortex at a specific location in a real-space binned image. The probability is computed from N repetitions, specified in the individual image. At low polarizations, the vortices are clearly visible at the pinning location but disappear as P increases. b) Contrast between the peaks and the background in the images in a. While C_1 shows the contrast between a single vortex and the surrounding background, C_2 considers the vortex pair. We can see that for both cases the contrast stays well above zero for polarizations up to $P = 0.15$. c) Temperatures at the given polarizations from the images in a. Adapted from [208].



10.4 Interpretation of the results

In the previous sections, we made two key observations for spin-imbalanced Fermi mixtures in 2D:

1. For any interaction and polarization examined in the experiment, there is no phase separation in a homogeneous trapping geometry, and the local polarization stays constant over the entire system.

2. A coherent oscillation of the condensate at $P = 0.13$ is visible well into the strongly interacting regime and vanishes on the BCS side.

3. Additionally, vortices can be observed up to $P = 0.15$ at strong interactions ($\ln(k_F a_{2D}) = 1$).

We can therefore conclude that, from the BEC to the strongly interacting regime, the system is a locally imbalanced superfluid. However, as established in Ch. 8.3, theory predicts multiple different phases that allow spin-imbalanced superfluids.

At $T = 0$ in a homogeneous 2D system, the most likely phase for an imbalanced superfluid is the FFLO phase, as the Sarma phase has a larger free energy. In situ images can theoretically resolve the spatially modulating order parameter, which is tied to local polarization, as previously discussed and shown in [198]. However, the size of those structures is on the order of the healing length, which in our system is $\xi \approx 2\,\mu$m. Since our mean interparticle distance is comparable ($1/\sqrt{n} \approx 1$), this means that on average, only a handful of atoms are missing along the line where the order parameter drops and the system is locally imbalanced. Additionally, since the microscope objective has a resolution[20] of 1.5 μm, we are currently unable to resolve features of this size. Alternatively, Bragg spectroscopy allows for the extraction of momentum-resolved spectra. When probing along the direction of the non-zero momentum of the superfluid pairs, there should be an energy dip in this spectrum, located at q_{FFLO}. In previous Bragg measurements, we have not observed this feature [59], therefore making it unlikely that an FFLO phase exists in our experiment. This is unsurprising, since the FFLO phase is predicted to be unstable at our current experimental temperatures [198].

[20] The current resolution is limited due to alignment. Theoretically, resolutions of 0.7 μm should be achievable in our setup.

Furthermore, we can rule out a Bose-Fermi mixture, as the largest E_B/E_F in our measurement is 6.3, which is lower than the miscibility criterion ($E_B/E_F > 7.28$) requires.

A much more likely scenario is that the excess majority resides atop the superfluid as thermal excitations. Looking at related experiments, in a 3D spin mixture at temperatures similar to those in our experiments, imbalanced superfluids up to $P \approx 0.2$ are supported by thermal excitations [13]. Additionally, the observed tricritical point for a first-order phase transition in 3D occurs at temperatures similar to those in our experiment. Therefore, such a point might exist at lower temperatures than in our experiments, but we can ultimately exclude its existence for temperatures larger than $0.05\,T_F$. This is also consis-

tent with our observations in harmonic confinement, which suggest a higher-order phase transition.

10.5 Outlook

While the results in this chapter demonstrated the existence of a locally imbalanced superfluid phase, without a first-order phase transition, many questions regarding the phase diagram still remain.

The two major ones concern what happens at temperatures lower than those reached in the experiment. Is there a tricritical point below which phase separation occurs? And when the temperature is lowered below $0.03\,T_\mathrm{F}$, will the FFLO phase become stable?

While the former is easy to verify by directly observing balanced and imbalanced domains, detecting the FFLO phase is less straightforward. While it might be impossible to observe the spatial structures in situ, it is possible to use interference with a reference superfluid that is in an SF_0 or SF_M phase, as proposed by [209]. Conceptually, this is easily achievable in the experiment, either by loading two layers in the accordion or by splitting the ring into two reservoirs. If one of the reservoirs is in the FFLO phase, a checkerboard pattern would emerge after interference during time-of-flight expansion [209]. Additionally, Bragg spectroscopy should be able to observe mode softening at q_FFLO, even slightly above T_FFLO.

Of course, these measurements require lower temperatures in the experiment. To our current knowledge, there are two ways that could potentially achieve this. The first one is the state-dependent ring potential previously explained in Ch. 9.1.1, in which one spin state is selectively spilled by overlapping a state-dependent potential with the repulsive ring. It is unclear, however, whether the near-resonant light in the vicinity of the trapped atoms might still introduce significant heat to the system. Another promising path is "meniscus cooling", an improved ring evaporation sequence that was tested towards the end of the imbalance project. It is explained in Appendix B, but in short, instead of creating a balanced core in the center of the trap by adding an attractive dimple, we do the opposite. Projecting a repulsive potential in the center leads to a balanced region forming on the outside of the ring, while the excess majority moves to the center of the trap. Performing ring evaporation in this configuration enabled us to achieve higher polarizations at constant temperatures. However, to date, we have not been able to reach temperatures below $0.03\,T_\mathrm{F}$ at polarizations $P \geq 0.15$ with this technique, and further optimization is required.

A further improvement that was implemented toward the end of this work is double-shot imaging, as explained in Appendix A. With this technique, it is possible to image both spin states in the same cycle, enabling polarization-based post-selection. This eliminates uncertainty in the polarization due to shot-to-shot fluctuations, and since the FFLO phase is predicted only in a small region of the phase

diagram, one could choose a precise P at which it is expected to be stable.

Part V

Conclusion

11 CONCLUSION AND OUTLOOK

In this thesis, I have presented experiments that use the strong confinement of a 2D Fermi gas to probe a variety of many-body phenomena.

The first results, presented in Part II, showed how the amplitude mode can hybridize with a confinement-induced mode. Typically, the amplitude mode is challenging to excite, since the interactions have to be modulated. Previous experiments achieved this by either modulating or quenching the magnetic field, or using RF dressing to modulate the interactions at the Rabi rate due to an oscillating occupation of a third state. In our experiment, we exploited the fact that the 2D scattering length depends on the trap frequency ω_z, and therefore, by periodically modulating ω_z, we also modulate the interactions.

We find that in the BCS regime, the excitation frequency follows the mean-field prediction for the amplitude mode. Towards the strongly interacting regime, it hybridizes with a confinement-induced mode from the multibranch Bogoliubov spectrum as their energies become comparable. This is also evident when extracting the gap from the pair-breaking continuum via Bragg spectroscopy: the energies disagree towards strong interactions. Far in the BEC regime, the confinement-induced mode finally approaches twice the trap frequency, as expected for a non-interacting BEC.

Finally, we observed that the confinement-induced mode vanishes at around $0.09\,T_\mathrm{F}$, consistent with previous measurements of the superfluid critical temperature in 2D, making it a probe for superfluidity.

The first main result of this thesis, presented in the following Part III, was the observation of repulsive Bose polarons well into the strongly interacting regime. We were able to eliminate the typical decay paths into the attractive branch by using Feshbach dimers comprised of fermions. These dimers behave as bosons and feature residual repulsion, while being protected from decay into larger bound states via Pauli blocking. To create an impurity in this system, we exploited the discrete energy levels of strong confinement as a synthetic spin. The bath resides in the ground state, while impurities were created by exciting a small fraction of the dimers into the first or second excited impurity states.

In this study, we were able to extract all key quantities of the quasiparticle: The polaron energies, as well as the quasiparticle residue, were measured using trap modulation spectroscopy. Furthermore, we used Bragg spectroscopy to obtain a momentum-resolved spectrum and, for the first time, extract the effective mass of the repulsive Bose polaron. We observed a growing energy shift and effective mass, as

well as a reduction in the quasiparticle residue towards strong interactions, signaling the enhanced dressing by the medium.

While we see great agreement with T-matrix and QMC theory for the energies and quasiparticle residues, the behavior of the effective mass differs, especially for the $n_z = 2$ impurity. This disagreement is unsurprising, as calculating the effective mass requires higher-order corrections and is therefore computationally challenging.

In the second main result in Part IV, we explored the phase diagram of 2D imbalanced Fermi gases. Generally, imbalanced systems are of great interest due to the broad range of phases that can occur. Most notable is the elusive FFLO phase, where pairing happens at a nonzero pair momentum, and the order parameter oscillates spatially. But even without considering exotic phases, many questions remain, as theory predicts phase separation as the result of a first-order phase transition, which has not yet been observed experimentally.

Our experiment reached temperatures lower than $0.04\,T_\mathrm{F}$ at a polarization of up to $P = 0.2\,\%$, well within the regime where theory predicts phase separation. However, in our homogeneous box potential, we did not observe any domain formation but rather a constant local polarization spanning the entire system. Performing trap-modulation spectroscopy then showed that the multibranch Bogoliubov mode, previously identified as a probe of superfluidity, persists well into the strongly interacting regime. This observation is further supported by experiments where vortices were deterministically created and pinned in the 2D system.

The most likely interpretation of these observations is that our system is in a locally imbalanced superfluid phase, in which the excess majority lives as thermal excitations on top of the superfluid. This superfluid behavior breaks down in the BCS regime due to the imbalance, since both the confinement-induced mode and the vortices vanish. A first-order phase transition, as predicted by theory, can therefore be ruled out for temperatures $T \geq 0.04\,T_\mathrm{F}$. Furthermore, we can exclude the possibility that our experiment is in the FFLO phase, since a previously extracted momentum spectrum of our system does not show mode softening at the expected finite pair momentum q_FFLO.

Outlook

Generally, the experimental apparatus is a versatile platform that opens many avenues for future experiments. In the following, I will discuss a few possibilities that became available after recent upgrades and innovations in the experiment, with a specific focus on options that extend on the work presented in this thesis.

Most notably, in recent experiments spearheaded by Artak Mkrtchyan and Hans Leonard Michel, it became possible to deterministically create vortices in our system, similar to experiments in the Anderson and Scazza groups [207, 210]. These can be created anywhere in the 2D–3D crossover regime accessible through the accordion lattice setup.

Further investigating vortices in imbalanced Fermi gases may reveal states akin to Andreev-bound states, where particles of the excess majority are bound inside the vortex core [211]. Since our imbalanced systems feature a homogeneous local imbalance, as demonstrated in Ch. 10.1, we can precisely control the polarizations in which the vortices are immersed. Together with the newly implemented double-shot imaging (see Appendix A), it might be possible to observe a locally increased imbalance, where a vortex core is located.

Another potential avenue in imbalanced Fermi gases is the search for FFLO phases. As discussed in Ch. 10.5, further improvements to the cooling sequence, such as meniscus cooling (see Appendix B), can achieve even lower temperatures than those reported here. Using Bragg spectroscopy, one might see a mode softening at q_{FFLO}, a precursor of the FFLO phase. Additionally, during meniscus cooling, the system may be split into a more balanced outer part and an imbalanced center by projecting a second repulsive ring via a DMD. Optimizing the polarizations between the two reservoirs may lead to the FFLO phase appearing at the center, with the outer region being a homogeneous superfluid. In this scenario, removing the trapping potentials and letting the clouds interfere would reveal a checkerboard density pattern, as suggested in [209].

Another possibility is to probe the second sound, a clear sign of superfluidity that provides a way to determine the superfluid density. It is a direct consequence of the two-fluid model, where a superfluid and a fluid in the normal phase occupy the same space. While a regular sound wave manifests as an in-phase density wave of both fluids, leading to a global density deformation, second sound is an out-of-phase density modulation. This suppresses global density deformation, even though a density wave is propagating through both components. Since only the normal fluid carries entropy, second sound can be understood as an entropy wave.

Second sound was previously observed in 3D quantum gas experiments [212–216] and 2D Bose gases [217]; however, it remains unobserved in 2D Fermi gases. To probe second sound in our experiment, we would need to locally increase the entropy in the system by introducing heat in a small area on short timescales. Since second sound does not couple strongly to density modulations, we can use Bragg spectroscopy locally to address the pair-breaking continuum. Alternatively, we could use a state-dependent Bragg setup that employs near-resonant light to create potentials of opposite sign for the two hyperfine states. This setup eliminates coupling to density modes in general and allows stronger coupling to the pair-breaking continuum. Additionally, we need a way to probe the temperature locally, which may be possible using RF thermometry, as demonstrated in [216]. These studies could also be extended to probe imbalanced systems and extract the superfluid fraction for varying polarizations and interactions.

Lastly, because of the variable lattice spacing of the accordion, we can probe the 2D–3D crossover. Specifically, it would be interesting to investigate the phenomenon of shape resonances that have been observed in thin film superconductors [71, 72]. These resonances appear whenever the energy from a confinement-induced excitation crosses that of the Fermi energy (or chemical potential) [70], and can lead to an enhancement of the superfluid gap. A priori, these resonances should also occur in strongly confined Fermi gases, and it would be exciting to probe the superfluid gap, e.g., via Bragg spectroscopy, when tuning the level spacing of the harmonic oscillator close to the chemical potential.

A DOUBLE-SHOT IMAGING

A technique that has been implemented during the course of this work is double shot imaging. Since it was only running reliably towards the end of this work, it is not used in any of the results presented here and therefore not explained in the main text.

Usually only one spin state can be imaged per experimental cycle. The goal of double-shot imaging is an improved imaging scheme that allows for imaging both spin states within the same sequence. This brings multiple advantages, most importantly the ability to post-select data by imbalance P. As shown in Ch. 9.1.2, the uncertainty for P in our experiment is considerable, which makes it practically impossible to investigate exotic superfluid phases, as they live in small parameter ranges.

Implementing such a double-shot sequence, which extracts two density images, is technically challenging. The main reason is that ^{6}Li atoms are very light and therefore move at high velocities after switching off the optical traps. As a consequence, the images have to be taken in quick succession. In our setup, the limiting factor for the time between shots is determined by the time it takes the camera to shift an image out of the active region of the CCD. The usual imaging process in our experiment involves four images to create a density image: an image with atoms, one without atoms, and two images without any imaging light present, to subtract the background counts. For future reference, we label these images as *Atoms*, *Bright*, *AtomsDark*, *BrightDark*. In the double-shot sequence, each of the four images must be taken twice, once for each spin state. Already in the single-shot case, the Atoms and Bright images are acquired in quick succession to reduce noise primarily caused by fluctuations in the imaging beam power. The essential feature of the camera that enables these pictures to be taken in quick succession is the "fast kinetics" mode, which is illustrated in Fig. A.1. Here, an inactive region of the CCD chip is used as storage, into which multiple images can be shifted quickly without requiring a slow readout that typically takes on the order of 1 s. Instead, the readout happens at the end of this predefined

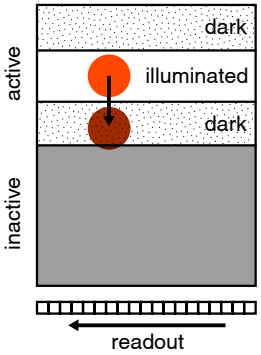


Figure A.1: CCD chip of the camera in fast kinetics mode. The chip features an active (white area) and an inactive region (grey area). Only the active region can be illuminated. In fast-kinetics mode, the inactive region is used as storage, so no slow readout is required across multiple images. The inactive region can be artificially enlarged by blocking light from selected regions of the chip (dotted area), e.g., using razor blades.

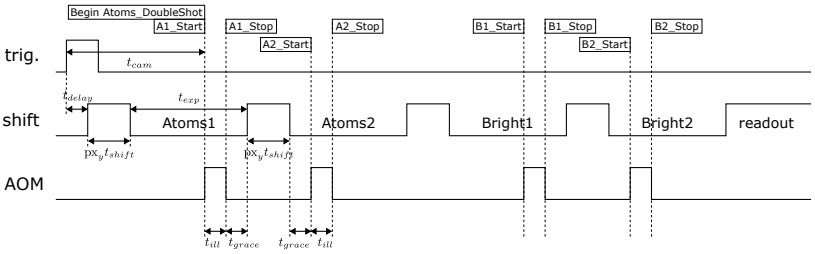


Figure A.2: Timing edges for the double-shot sequence. The camera trigger (trig.) initiates the entire imaging sequence of the camera. In between the exposures, the images are shifted (shift). The imaging pulses (AOM) for the two Atoms images are adjusted to occur as close together as possible to reduce blur due to atom motion in Atoms2.

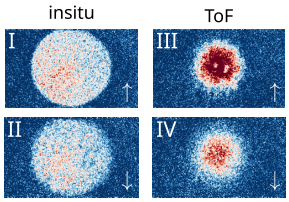


Figure A.3: Double shot images in situ and after ToF. The second shot is always blurry due to atomic expansion, making it impossible to observe vortices in the second ToF image. However, a polarization can be extracted for each experimental cycle. Adapted from [208].

sequence of images. The inactive region is the same size as the active region; however, it can be artificially extended by covering part of the CCD, e.g., by placing razor blades in the beam path.

For the double-shot image, blocking part of the CCD is required for two reasons: First, the vertical size of the image determines the time required to shift it out of the active region. Therefore, if we want to take multiple images as quickly as possible, the image should be smaller. Secondly, we want to take more than two pictures: two Atoms and two Bright images. If the entire active area were used instead, there would be space for only two pictures. By reducing the size of the active area and therefore the image size, there is enough space for all four images.

By precisely adjusting the timing as shown in Fig. A.2, and quickly changing the wavelength of the imaging light by using an AOM, two independent density images can be acquired, one for each spin state. This technique is used in current studies of our experiment, and a reference image is shown in Fig. A.3. We can see that the second shot is always blurrier than the first, since the atoms already expand during the first shot. In our ToF images, this means that we cannot image vortices in the second shot; however, we can still extract the polarizations after performing the corrections detailed in [208].

B MENISCUS COOLING

Here, I will describe a newly developed cooling procedure that can be used in tandem with the preparation sequence used in previous experiments, namely a Landau-Zener sweep to a third hyperfine state, followed by a blowout. In general, this cooling technique is also applicable to other preparation strategies that introduce heat into the system and require subsequent cooling.

The fundamental idea is to exploit the local balancing that occurs at the minimum of potential gradients, as presented in Ch. 10.1, or in the work of J. Thomas [14] and W. Bakr [15]. However, instead of creating an attractive potential in the center, it is repulsive and, in our experiment, introduced via a DMD using repulsive 532 nm light. In this scenario, the balanced region forms in the outer region, and the imbalance is pushed to the center (see Fig. B.1). Therefore, the balancing effect is suppressed because evaporation occurs at the point where the system is balanced. Due to the radial density change, we coined this procedure *meniscus cooling*, reminiscent of the meniscus observed in surface-tensioned liquids.

Initial experiments have shown that we can achieve higher polarizations at constant temperature; however, this procedure is currently fairly unoptimized and does not allow us to reach temperatures well below the predicted critical temperature for FFLO. This procedure can be further augmented by removing the more balanced region on the outside while keeping the imbalanced center. This can be achieved, e.g., by using a second DMD to project a smaller ring into the sample and then turning off the outer ring. In principle, this should lead to a system at a similar T/T_F but with larger P.

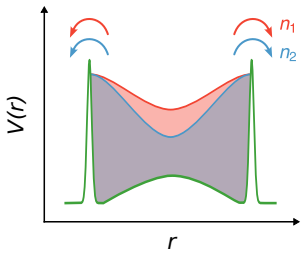


Figure B.1: Meniscus cooling scheme. A repulsive potential $V(r)$ is placed in the center of the trap, leading to the formation of a balanced region on the outside. Lowering the ring power then leads to evaporation of both species.

BIBLIOGRAPHY

[1] J. Bardeen, L. N. Cooper, and J. R. Schrieffer: *Theory of superconductivity*, "Phys. Rev." vol. 108, no. 5, 1175–1204 (1957) (cited on pages 7, 17, 19, 55).

[2] L. D. Landau and V. L. Ginzburg: *On the theory of superconductivity*, "Zh. Eksp. Teor. Fiz." vol. 20, 1064 (1950) (cited on page 7).

[3] W. Zwerger: *The BCS-BEC crossover and the unitary Fermi gas, Vol. 836* (*Springer Science & Business Media, 2011*) (cited on pages 7, 32, 71).

[4] M. Greiner, O. Mandel, T. Esslinger, T. W. Hänsch, and I. Bloch: *Quantum phase transition from a superfluid to a Mott insulator in a gas of ultracold atoms*, "Nature" vol. 415, no. 6867, 39–44 (2002) (cited on page 7).

[5] M. Holten, L. Bayha, K. Subramanian, S. Brandstetter, C. Heintze, P. Lunt, P. M. Preiss, and S. Jochim: *Observation of Cooper pairs in a mesoscopic two-dimensional Fermi gas*, "Nature" vol. 606, no. 7913, 287–291 (2022) (cited on page 7).

[6] L. Sobirey, N. Luick, M. Bohlen, H. Biss, H. Moritz, and T. Lompe: *Observation of superfluidity in a strongly correlated two-dimensional Fermi gas*, "Science" vol. 372, no. 6544, 844–846 (2021) (cited on pages 7, 36, 39, 46, 57, 61, 72, 77, 105).

[7] N. Luick, L. Sobirey, M. Bohlen, V. P. Singh, L. Mathey, T. Lompe, and H. Moritz: *An ideal Josephson junction in an ultracold two-dimensional Fermi gas*, "Science" vol. 369, no. 6499, 89–91 (2020) (cited on page 7).

[8] H. Biss, L. Sobirey, N. Luick, M. Bohlen, J. J. Kinnunen, G. M. Bruun, T. Lompe, and H. Moritz: *Excitation Spectrum and Superfluid Gap of an Ultracold Fermi Gas*, "Phys. Rev. Lett." vol. 128, no. 10, 100401 (2022) (cited on pages 7, 36, 37, 57, 77).

[9] L. Sobirey, H. Biss, N. Luick, M. Bohlen, H. Moritz, and T. Lompe: *Observing the Influence of Reduced Dimensionality on Fermionic Superfluids*, "Phys. Rev. Lett." vol. 129, no. 8, 083601 (2022) (cited on pages 7, 36, 37).

[10] C. R. Cabrera, R. Henke, L. Broers, J. Skulte, H. P. O. Collado, H. Biss, L. Mathey, and H. Moritz: *Hybridization of the amplitude mode in a confined fermionic superfluid*, "Phys. Rev. Res." vol. 7, no. 3, L032018 (2025) (cited on pages 7, 11, 49, 55, 73).

[11] B. S. Chandrasekhar: *A note on the maximum critical fiels of high-field superconductors*, "Appl. Phys. Lett." vol. 1, no. 1, 7–8 (1962) (cited on pages 8, 84).

[12] A. M. Clogston: *Upper Limit for the Critical Field in Hard Superconductors*, "Phys. Rev. Lett." vol. 9, no. 6, 266–267 (1962) (cited on pages 8, 84).

[13] Y.-i. Shin, C. H. Schunck, A. Schirotzek, and W. Ketterle: *Phase diagram of a two-component Fermi gas with resonant interactions*, "Nature" vol. 451, no. 7179, 689–693 (2008) (cited on pages 8, 85, 86, 103, 104, 107).

[14] W. Ong, C. Cheng, I. Arakelyan, and J. E. Thomas: *Spin-Imbalanced Quasi-Two-Dimensional Fermi Gases*, "Phys. Rev. Lett." vol. 114, no. 11, 110403 (2015) (cited on pages 8, 68, 85, 95, 101, 102, 104, 119).

[15] D. Mitra, P. T. Brown, P. Schauß, S. S. Kondov, and W. S. Bakr: *Phase Separation and Pair Condensation in a Spin-Imbalanced 2D Fermi Gas*, "Phys. Rev. Lett." vol. 117, no. 9, 093601 (2016) (cited on pages 8, 86, 87, 95, 101, 102, 104, 119).

[16]L. D. Landau and S. I. Pekar: *Effective mass of a polaron*, "Zh. Eksp. Teor. Fiz." vol. 18, 419 (1948) (cited on pages 8, 65).

[17]C. Franchini, M. Reticcioli, M. Setvin, and U. Diebold: *Polarons in materials*, "Nat Rev Mater" vol. 6, no. 7, 560–586 (2021) (cited on pages 9, 65).

[18]F. Scazza, M. Zaccanti, P. Massignan, M. M. Parish, and J. Levinsen: *Repulsive Fermi and Bose Polarons in Quantum Gases*, "Atoms" vol. 10, no. 2, 55 (2022) (cited on pages 9, 65, 68, 77).

[19]R. Henke, J. Levinsen, M. M. Parish, J. Boronat, G. E. Astrakharchik, H. Moritz, and C. R. Cabrera: *Realization of repulsive polarons in the strongly correlated regime*, 2025 (cited on pages 11, 44, 46, 47, 49, 71, 74, 78).

[20]M. H. Anderson, J. R. Ensher, M. R. Matthews, C. E. Wieman, and E. A. Cornell: *Observation of Bose-Einstein Condensation in a Dilute Atomic Vapor*, "Science" vol. 269, no. 5221, 198–201 (1995) (cited on page 18).

[21]K. B. Davis, M. O. Mewes, M. R. Andrews, N. J. van Druten, D. S. Durfee, D. M. Kurn, and W. Ketterle: *Bose-Einstein Condensation in a Gas of Sodium Atoms*, "Phys. Rev. Lett." vol. 75, no. 22, 3969–3973 (1995) (cited on page 18).

[22]C. J. Pethick and H. Smith: *Bose–Einstein Condensation in Dilute Gases*, 2nd ed., Cambridge: Cambridge University Press 2008 (cited on page 18).

[23]M. W. Zwierlein: *High-temperature superfluidity in an ultracold Fermi gas*, PhD thesis, Massachusetts Institute of Technology 2006 (cited on pages 18, 19).

[24]M. Marini, F. Pistolesi, and G. Strinati: *Evolution from BCS superconductivity to Bose condensation: analytic results for the crossover in three dimensions*, "Eur. Phys. J. B" vol. 1, no. 2, 151–159 (1998) (cited on page 21).

[25]D. Pekker and C. Varma: *Amplitude/Higgs Modes in Condensed Matter Physics*, "Annu. Rev. Condens. Matter Phys." vol. 6, no. 1, 269–297 (2015) (cited on pages 26, 55–57).

[26]L. P. Gor'Kov: *Microscopic derivation of the Ginzburg-Landau equations in the theory of superconductivity*, "Sov. Phys. JETP" vol. 36, 1364–1367 (1959) (cited on page 30).

[27]A. Deuchert, C. Hainzl, and M. O. Maier: *Microscopic derivation of Ginzburg–Landau theory and the BCS critical temperature shift in general external fields*, "Calc. Var." vol. 62, no. 7, 203 (2023) (cited on page 30).

[28]A. Altland and B. D. Simons: *Condensed Matter Field Theory*, Cambridge University Press Mar. 2010 (cited on page 30).

[29]Y. Nambu: *Quasi-Particles and Gauge Invariance in the Theory of Superconductivity*, "Phys. Rev." vol. 117, no. 3, 648–663 (1960) (cited on page 31).

[30]C. M. Varma: *Higgs Boson in Superconductors*, "J. Low Temp. Phys." vol. 126, no. 3, 901–909 (2002) (cited on page 31).

[31]G. C. Strinati, P. Pieri, G. Röpke, P. Schuck, and M. Urban: *The BCS–BEC crossover: From ultra-cold Fermi gases to nuclear systems*, "Phys. Rep." vol. 738, 1–76 (2018) (cited on page 31).

[32]J. Levinsen and M. M. Parish: *Strongly interacting two-dimensional Fermi gases*, in *Annual Review of Cold Atoms and Molecules*, Vol. 3, Annual Review of Cold Atoms and Molecules, World Scientific Feb. 2015, pp. 1–75 (cited on pages 32, 57).

[33]M. Randeria, J.-M. Duan, and L.-Y. Shieh: *Bound states, Cooper pairing, and Bose condensation in two dimensions*, "Phys. Rev. Lett." vol. 62, no. 9, 981–984 (1989) (cited on page 33).

[34]N. D. Mermin and H. Wagner: *Absence of Ferromagnetism or Antiferromagnetism in One- or Two-Dimensional Isotropic Heisenberg Models*, "Phys. Rev. Lett." vol. 17, no. 22, 1133–1136 (1966) (cited on page 33).

[35]P. C. Hohenberg: *Existence of Long-Range Order in One and Two Dimensions*, "Phys. Rev." vol. 158, no. 2, 383–386 (1967) (cited on page 33).

[36]V. Berezinskii: *Destruction of long-range order in one-dimensional and two-dimensional systems having a continuous symmetry group I. Classical systems*, "Sov. Phys. JETP" vol. 32, no. 3, 493–500 (1971) (cited on page 33).

[37]J. M. Kosterlitz and D. J. Thouless: *Ordering, metastability and phase transitions in two-dimensional systems*, "J. Phys. C: Solid State Phys." vol. 6, no. 7, 1181 (1973) (cited on page 33).

[38]D. S. Petrov and G. V. Shlyapnikov: *Interatomic collisions in a tightly confined Bose gas*, "Phys. Rev. A" vol. 64, no. 1, 012706 (2001) (cited on pages 34, 57, 72).

[39]I. Bloch, J. Dalibard, and W. Zwerger: *Many-body physics with ultracold gases*, "Rev. Mod. Phys." vol. 80, no. 3, 885–964 (2008) (cited on page 34).

[40]G. Bertaina and S. Giorgini: *BCS-BEC Crossover in a Two-Dimensional Fermi Gas*, "Phys. Rev. Lett." vol. 106, no. 11, 110403 (2011) (cited on pages 34, 90).

[41]L. Pricoupenko: *Variational approach for the two-dimensional trapped Bose-Einstein condensate*, "Phys. Rev. A" vol. 70, no. 1, 013601 (2004) (cited on page 34).

[42]C. Mora and Y. Castin: *Ground State Energy of the Two-Dimensional Weakly Interacting Bose Gas: First Correction Beyond Bogoliubov Theory*, "Phys. Rev. Lett." vol. 102, no. 18, 180404 (2009) (cited on page 34).

[43]G. E. Astrakharchik, J. Boronat, J. Casulleras, I. L. Kurbakov, and Y. E. Lozovik: *Equation of state of a weakly interacting two-dimensional Bose gas studied at zero temperature by means of quantum Monte Carlo methods*, "Phys. Rev. A" vol. 79, no. 5, 051602 (2009) (cited on pages 34, 74, 75).

[44]F. Qin and J.-s. Chen: *Sound Velocity and Eigenfrequencies of a Disk-Shaped Harmonically Trapped Superfluid Fermi Gas in the BCS-BEC Crossover*, "J Low Temp Phys" vol. 169, no. 1, 25–39 (2012) (cited on pages 35, 38).

[45]E. Zaremba: *Sound propagation in a cylindrical Bose-condensed gas*, "Phys. Rev. A" vol. 57, no. 1, 518–521 (1998) (cited on pages 35, 38).

[46]T. K. Ghosh and K. Machida: *Sound velocity and multibranch Bogoliubov spectrum of an elongated Fermi superfluid in the BEC-BCS crossover*, "Phys. Rev. A" vol. 73, no. 1, 013613 (2006) (cited on pages 35, 38).

[47]L. Sobirey: *Superfluidity in two-dimensional Fermi gases*, PhD thesis, Universität Hamburg Sept. 2021 (cited on pages 36, 37, 47).

[48]C. Raman, M. Köhl, R. Onofrio, D. S. Durfee, C. E. Kuklewicz, Z. Hadzibabic, and W. Ketterle: *Evidence for a Critical Velocity in a Bose-Einstein Condensed Gas*, "Phys. Rev. Lett." vol. 83, no. 13, 2502–2505 (1999) (cited on page 36).

[49]R. Desbuquois, L. Chomaz, T. Yefsah, J. Léonard, J. Beugnon, C. Weitenberg, and J. Dalibard: *Superfluid behaviour of a two-dimensional Bose gas*, "Nature Phys" vol. 8, no. 9, 645–648 (2012) (cited on page 36).

[50]W. Weimer, K. Morgener, V. P. Singh, J. Siegl, K. Hueck, N. Luick, L. Mathey, and H. Moritz: *Critical Velocity in the BEC-BCS Crossover*, "Phys. Rev. Lett." vol. 114, no. 9, 095301 (2015) (cited on page 36).

[51]D. E. Miller, J. K. Chin, C. A. Stan, Y. Liu, W. Setiawan, C. Sanner, and W. Ketterle: *Critical Velocity for Superfluid Flow across the BEC-BCS Crossover*, "Phys. Rev. Lett." vol. 99, no. 7, 070402 (2007) (cited on page 36).

[52]L.-C. Ha, L. W. Clark, C. V. Parker, B. M. Anderson, and C. Chin: *Roton-Maxon Excitation Spectrum of Bose Condensates in a Shaken Optical Lattice*, "Phys. Rev. Lett." vol. 114, no. 5, 055301 (2015) (cited on page 36).

[53]M. Bohlen, L. Sobirey, N. Luick, H. Biss, T. Enss, T. Lompe, and H. Moritz: *Sound Propagation and Quantum-Limited Damping in a Two-Dimensional Fermi Gas*, "Phys. Rev. Lett." vol. 124, no. 24, 240403 (2020) (cited on page 36).

[54]G. Veeravalli, E. Kuhnle, P. Dyke, and C. J. Vale: *Bragg spectroscopy of a strongly interacting Fermi gas*, "Phys. Rev. Lett." vol. 101, no. 25, 250403 (2008) (cited on pages 36, 57).

[55]M. G. Lingham, K. Fenech, T. Peppler, S. Hoinka, P. Dyke, P. Hannaford, and C. J. Vale: *Bragg spectroscopy of strongly interacting Fermi gases*, "J. Mod. Opt." vol. 63, no. 18, 1783–1794 (2016) (cited on page 36).

[56]S. Hoinka, P. Dyke, M. G. Lingham, J. J. Kinnunen, G. M. Bruun, and C. J. Vale: *Goldstone mode and pair-breaking excitations in atomic Fermi superfluids*, "Nat. Phys." vol. 13, no. 10, 943–946 (2017) (cited on pages 36, 57).

[57]C. C. N. Kuhn, S. Hoinka, I. Herrera, P. Dyke, J. J. Kinnunen, G. M. Bruun, and C. J. Vale: *High-Frequency Sound in a Unitary Fermi Gas*, "Phys. Rev. Lett." vol. 124, no. 15, 150401 (2020) (cited on page 36).

[58]P. Dyke, S. Musolino, H. Kurkjian, D. J. M. Ahmed-Braun, A. Pennings, I. Herrera, S. Hoinka, S. J. J. M. F. Kokkelmans, V. E. Colussi, and C. J. Vale: *Higgs Oscillations in a Unitary Fermi Superfluid*, "Phys. Rev. Lett." vol. 132, no. 22, 223402 (2024) (cited on pages 36–38, 55, 57, 60).

[59]H. Biss: *Probing excitation spectra of ultracold 2D and 3D fermionic superfluids*, PhD thesis, Universität Hamburg Aug. 2023 (cited on pages 37, 46, 47, 88, 105, 107).

[60]R. Shimano and N. Tsuji: *Higgs Mode in Superconductors*, "Annu. Rev. Condens. Matter Phys." vol. 11, no. 1, 103–124 (2020) (cited on pages 37, 55).

[61]R. Matsunaga, Y. I. Hamada, K. Makise, Y. Uzawa, H. Terai, Z. Wang, and R. Shimano: *Higgs Amplitude Mode in the BCS Superconductors Nb1-xTix**N** Induced by Terahertz Pulse Excitation*, "Phys. Rev. Lett." vol. 111, no. 5, 057002 (2013) (cited on page 37).

[62]R. Sooryakumar and M. V. Klein: *Raman scattering by superconducting-gap excitations and their coupling to charge-density waves*, "Phys. Rev. Lett." vol. 45, no. 8, 660–662 (1980) (cited on pages 37, 55).

[63]R. Sooryakumar and M. V. Klein: *Raman scattering from superconducting gap excitations in the presence of a magnetic field*, "Phys. Rev. B" vol. 23, no. 7, 3213–3221 (1981) (cited on page 37).

[64]P. B. Littlewood and C. M. Varma: *Gauge-Invariant Theory of the Dynamical Interaction of Charge Density Waves and Superconductivity*, "Phys. Rev. Lett." vol. 47, no. 11, 811–814 (1981) (cited on page 37).

[65]P. B. Littlewood and C. M. Varma: *Amplitude collective modes in superconductors and their coupling to charge-density waves*, "Phys. Rev. B" vol. 26, no. 9, 4883–4893 (1982) (cited on page 37).

[66]T. Cea and L. Benfatto: *Nature and Raman signatures of the Higgs amplitude mode in the coexisting superconducting and charge-density-wave state*, "Phys. Rev. B" vol. 90, no. 22, 224515 (2014) (cited on page 37).

[67] R. Matsunaga, N. Tsuji, H. Fujita, A. Sugioka, K. Makise, Y. Uzawa, H. Terai, Z. Wang, H. Aoki, and R. Shimano: *Light-induced collective pseudospin precession resonating with Higgs mode in a superconductor*, "Science" vol. 345, no. 6201, 1145–1149 (2014) (cited on pages 37, 55).

[68] A. Kell, M. Breyer, D. Eberz, and M. Köhl: *Exciting the Higgs mode in a strongly interacting Fermi gas by interaction modulation*, "Phys. Rev. Lett." vol. 133, no. 15, 150403 (2024) (cited on pages 37, 55, 57, 60).

[69] J. Steinhauer, N. Katz, R. Ozeri, N. Davidson, C. Tozzo, and F. Dalfovo: *Bragg Spectroscopy of the Multibranch Bogoliubov Spectrum of Elongated Bose-Einstein Condensates*, "Phys. Rev. Lett." vol. 90, no. 6, 060404 (2003) (cited on page 38).

[70] J. M. Blatt and C. J. Thompson: *Shape resonances in superconducting thin films*, "Phys. Rev. Lett." vol. 10, no. 8, 332–334 (1963) (cited on pages 38, 55, 116).

[71] A. A. Shanenko, M. D. Croitoru, M. Zgirski, F. M. Peeters, and K. Arutyunov: *Size-dependent enhancement of superconductivity in Al and Sn nanowires: Shape-resonance effect*, "Phys. Rev. B" vol. 74, no. 5, 052502 (2006) (cited on pages 38, 55, 116).

[72] B. Abeles, R. W. Cohen, and G. W. Cullen: *Enhancement of superconductivity in metal films*, "Phys. Rev. Lett." vol. 17, no. 12, 632–634 (1966) (cited on pages 38, 55, 116).

[73] M. G. Ries, A. N. Wenz, G. Zürn, L. Bayha, I. Boettcher, D. Kedar, P. A. Murthy, M. Neidig, T. Lompe, and S. Jochim: *Observation of Pair Condensation in the Quasi-2D BEC-BCS Crossover*, "Phys. Rev. Lett." vol. 114, no. 23, 230401 (2015) (cited on pages 39, 86).

[74] K. H. Morgener: *Microscopy of 2D Fermi Gases: exploring excitations and thermodynamics*, PhD thesis, Universität Hamburg 2015 (cited on pages 40, 41).

[75] K. Hueck, N. Luick, L. Sobirey, J. Siegl, T. Lompe, and H. Moritz: *Two-Dimensional Homogeneous Fermi Gases*, "Phys. Rev. Lett." vol. 120, no. 6, 060402 (2018) (cited on pages 40, 43, 45, 56, 72).

[76] J. Dammann: *A compact laser setup for the cooling of 6Li atoms*, BSc Thesis, Hamburg: Universität Hamburg 2025 (cited on pages 41, 51).

[77] N. C. Luick: *An ideal Josephson junction in an ultracold two-dimensional Fermi gas*, PhD thesis, Universität Hamburg 2020 (cited on pages 42, 44).

[78] K. Hueck: *A homogeneous, two-dimensional Fermi gas*, PhD thesis, Universität Hamburg 2017 (cited on pages 43, 44).

[79] J. Faltinath: *Strongly correlated Fermi gases in two and three Dimensions*, MSc Thesis, Hamburg 2022 (cited on pages 44, 50).

[80] K. Hueck, N. Luick, L. Sobirey, J. Siegl, T. Lompe, H. Moritz, L. W. Clark, and C. Chin: *Calibrating high intensity absorption imaging of ultracold atoms*, "Opt. Express" vol. 25, no. 8, 8670–8679 (2017) (cited on page 44).

[81] P. W. Anderson: *Theory of dirty superconductors*, "J. Phys. Chem. Solids" vol. 11, no. 1, 26–30 (1959) (cited on page 55).

[82] S. Bose and P. Ayyub: *A review of finite size effects in quasi-zero dimensional superconductors*, "Rep. Prog. Phys." vol. 77, no. 11, 116503 (2014) (cited on page 55).

[83] A. Korolyuk, J. J. Kinnunen, and P. Törmä: *Density response of a trapped Fermi gas: A crossover from the pair vibration mode to the Goldstone mode*, "Phys. Rev. A" vol. 84, no. 3, 033623 (2011) (cited on page 55).

[84] A. Korolyuk, J. J. Kinnunen, and P. Törmä: *Collective excitations of a trapped Fermi gas at finite temperature*, "Phys. Rev. A" vol. 89, no. 1, 013602 (2014) (cited on pages 55, 59).

[85]J. Hertkorn, F. Böttcher, M. Guo, J. N. Schmidt, T. Langen, H. P. Büchler, and T. Pfau: *Fate of the amplitude mode in a trapped dipolar supersolid*, "Phys. Rev. Lett." vol. 123, no. 19, 193002 (2019) (cited on page 55).

[86]J. Bjerlin, S. M. Reimann, and G. M. Bruun: *Few-Body Precursor of the Higgs Mode in a Fermi Gas*, "Phys. Rev. Lett." vol. 116, no. 15, 155302 (2016) (cited on page 55).

[87]M.-A. Méasson, Y. Gallais, M. Cazayous, B. Clair, P. Rodière, L. Cario, and A. Sacuto: *Amplitude Higgs mode in the 2H-$NbSe_2$ superconductor*, "Phys. Rev. B" vol. 89, no. 6, 060503 (2014) (cited on page 55).

[88]D. Sherman, U. S. Pracht, B. Gorshunov, S. Poran, J. Jesudasan, M. Chand, P. Raychaudhuri, M. Swanson, N. Trivedi, A. Auerbach, M. Scheffler, A. Frydman, and M. Dressel: *The Higgs mode in disordered superconductors close to a quantum phase transition*, "Nat. Phys." vol. 11, no. 2, 188–192 (2015) (cited on page 55).

[89]U. Bissbort, S. Götze, Y. Li, J. Heinze, J. S. Krauser, M. Weinberg, C. Becker, K. Sengstock, and W. Hofstetter: *Detecting the amplitude mode of strongly interacting lattice bosons by Bragg scattering*, "Phys. Rev. Lett." vol. 106, no. 20, 205303 (2011) (cited on pages 55, 57).

[90]M. Endres, T. Fukuhara, D. Pekker, M. Cheneau, P. Schauss, C. Gross, E. Demler, S. Kuhr, and I. Bloch: *The 'Higgs' amplitude mode at the two-dimensional superfluid/Mott insulator transition*, "Nature" vol. 487, no. 7408, 454–458 (2012) (cited on pages 55, 57, 61).

[91]J. Léonard, A. Morales, P. Zupancic, T. Donner, and T. Esslinger: *Monitoring and manipulating Higgs and Goldstone modes in a supersolid quantum gas*, "Science" vol. 358, no. 6369, 1415–1418 (2017) (cited on page 55).

[92]A. Behrle, T. Harrison, J. Kombe, K. Gao, M. Link, J.-S. Bernier, C. Kollath, and M. Köhl: *Higgs mode in a strongly interacting fermionic superfluid*, "Nat. Phys." vol. 14, no. 8, 781–785 (2018) (cited on page 55).

[93]L. Bayha, M. Holten, R. Klemt, K. Subramanian, J. Bjerlin, S. M. Reimann, G. M. Bruun, P. M. Preiss, and S. Jochim: *Observing the emergence of a quantum phase transition shell by shell*, "Nature" vol. 587, no. 7835, 583–587 (2020) (cited on page 55).

[94]J. Skulte, L. Broers, J. G. Cosme, and L. Mathey: *Vortex and soliton dynamics in particle-hole-symmetric superfluids*, "Phys. Rev. Res." vol. 3, no. 4, 043109 (2021) (cited on page 56).

[95]A. V. Turlapov and M. Yu Kagan: *Fermi-to-Bose crossover in a trapped quasi-2D gas of fermionic atoms*, "J. Phys. Condens. Matter" vol. 29, no. 38, 383004 (2017) (cited on page 57).

[96]L. Salasnich: *Condensate fraction of a two-dimensional attractive Fermi gas*, "Phys. Rev. A" vol. 76, no. 1, 015601 (2007) (cited on page 58).

[97]H. Shi, S. Chiesa, and S. Zhang: *Ground-state properties of strongly interacting Fermi gases in two dimensions*, "Phys. Rev. A" vol. 92, no. 3, 033603 (2015) (cited on page 58).

[98]R. Verresen, R. Moessner, and F. Pollmann: *Avoided quasiparticle decay from strong quantum interactions*, "Nat. Phys." vol. 15, no. 8, 750–753 (2019) (cited on page 59).

[99]J. Lorenzana and G. Seibold: *Long-lived Higgs modes in strongly correlated condensates*, "Phys. Rev. Lett." vol. 132, no. 2, 026501 (2024) (cited on page 59).

[100]T. Cea, C. Castellani, G. Seibold, and L. Benfatto: *Nonrelativistic dynamics of the amplitude (Higgs) mode in superconductors*, "Phys. Rev. Lett." vol. 115, no. 15, 157002 (2015) (cited on page 59).

[101]T. Cea, C. Castellani, and L. Benfatto: *Nonlinear optical effects and third-harmonic generation in superconductors: Cooper pairs versus Higgs mode contribution*, "Phys. Rev. B" vol. 93, no. 18, 180507 (2016) (cited on page 59).

[102]H. Kurkjian, S. N. Klimin, J. Tempere, and Y. Castin: *Pair-breaking collective branch in BCS superconductors and superfluid Fermi gases*, "Phys. Rev. Lett." vol. 122, no. 9, 093403 (2019) (cited on page 59).

[103]H. Kurkjian, J. Tempere, and S. N. Klimin: *Linear response of a superfluid Fermi gas inside its pair-breaking continuum*, "Sci. Rep." vol. 10, no. 1, 11591 (2020) (cited on page 59).

[104]C. Vaswani, J. H. Kang, M. Mootz, L. Luo, X. Yang, C. Sundahl, D. Cheng, C. Huang, R. H. J. Kim, Z. Liu, Y. G. Collantes, E. E. Hellstrom, I. E. Perakis, C. B. Eom, and J. Wang: *Light quantum control of persisting Higgs modes in iron-based superconductors*, "Nat. Commun." vol. 12, no. 1, 258 (2021) (cited on page 60).

[105]S. Hannibal, P. Kettmann, M. D. Croitoru, A. Vagov, V. M. Axt, and T. Kuhn: *Quench dynamics of an ultracold Fermi gas in the BCS regime: Spectral properties and confinement-induced breakdown of the Higgs mode*, "Phys. Rev. A" vol. 91, no. 4, 043630 (2015) (cited on page 61).

[106]S. Hannibal, P. Kettmann, M. D. Croitoru, V. M. Axt, and T. Kuhn: *Dynamical vanishing of the order parameter in a confined Bardeen-Cooper-Schrieffer Fermi gas after an interaction quench*, "Phys. Rev. A" vol. 97, no. 1, 013619 (2018) (cited on page 61).

[107]H. P. O. Collado, N. Defenu, and J. Lorenzana: *Engineering Higgs dynamics by spectral singularities*, "Phys. Rev. Res." vol. 5, no. 2, 023011 (2023) (cited on page 61).

[108]T. Nakayama, I. Danshita, T. Nikuni, and S. Tsuchiya: *Fano resonance through Higgs bound states in tunneling of Nambu-Goldstone modes*, "Phys. Rev. A" vol. 92, no. 4, 043610 (2015) (cited on page 61).

[109]T. Nakayama and S. Tsuchiya: *Perfect transmission of Higgs modes via antibound states*, "Phys. Rev. A" vol. 100, no. 6, 063612 (2019) (cited on page 61).

[110]A. J. Leggett: *Number-phase fluctuations in two-band superconductors*, "Prog. Theor. Phys." vol. 36, no. 5, 901 (1966) (cited on page 61).

[111]H. Krull, N. Bittner, G. S. Uhrig, D. Manske, and A. P. Schnyder: *Coupling of Higgs and Leggett modes in non-equilibrium superconductors*, "Nat. Commun." vol. 7, no. 1, 11921 (2016) (cited on page 61).

[112]F. Giorgianni, T. Cea, C. Vicario, C. P. Hauri, W. K. Withanage, X. Xi, and L. Benfatto: *Leggett mode controlled by light pulses*, "Nat. Phys." vol. 15, no. 4, 341 (2019) (cited on page 61).

[113]K. G. Jackson, C. J. Dale, J. Maki, K. G. S. Xie, B. A. Olsen, D. J. M. Ahmed-Braun, S. Zhang, and J. H. Thywissen: *Emergent s-wave interactions between identical fermions in quasi-one-dimensional geometries*, "Phys. Rev. X" vol. 13, no. 2, 021013 (2023) (cited on page 61).

[114]C. J. Dale, K. G. S. Xie, K. Pond Grehan, S. Zhang, J. Maki, and J. H. Thywissen: *Emergent s-wave interactions in orbitally active quasi-two-dimensional Fermi gases*, "Phys. Rev. A" vol. 110, no. 5, L051302 (2024) (cited on page 61).

[115]S. Pekar: *Local quantum states of electrons in an ideal ion crystal*, "Zh. Eksp. Teor. Fiz." vol. 16, no. 4, 341–348 (1946) (cited on page 65).

[116]H. Fröhlich: *Electrons in lattice fields*, "Adv. Phys." vol. 3, no. 11, 325–361 (1954) (cited on page 65).

[117]F. Grusdt, N. Mostaan, E. Demler, and L. A. P. Ardila: *Impurities and polarons in bosonic quantum gases: a review on recent progress*, "Rep. Prog. Phys." vol. 88, no. 6, 066401 (2025) (cited on pages 65–67).

[118]M. Sidler, P. Back, O. Cotlet, A. Srivastava, T. Fink, M. Kroner, E. Demler, and A. Imamoglu: *Fermi polaron-polaritons in charge-tunable atomically thin semiconductors*, "Nat. Phys." vol. 13, no. 3, 255–261 (2017) (cited on page 65).

[119]D. Cortecchia, J. Yin, A. Bruno, S.-Z. Alencious Lo, G. G. Gurzadyan, S. Mhaisalkar, J.-L. Brédas, and C. Soci: *Polaron self-localization in white-light emitting hybrid perovskites*, "J. Mater. Chem. C" vol. 5, no. 11, 2771–2780 (2017) (cited on page 65).

[120]C.-H. Wu, I. Santiago, J. W. Park, P. Ahmadi, and M. W. Zwierlein: *Strongly interacting isotopic Bose-Fermi mixture immersed in a Fermi sea*, "Phys. Rev. A" vol. 84, no. 1, 011601 (2011) (cited on page 66).

[121]J. Catani, G. Lamporesi, D. Naik, M. Gring, M. Inguscio, F. Minardi, A. Kantian, and T. Giamarchi: *Quantum dynamics of impurities in a one-dimensional Bose gas*, "Phys. Rev. A" vol. 85, no. 2, 023623 (2012) (cited on pages 66, 67).

[122]N. B. Jørgensen, L. Wacker, K. T. Skalmstang, M. M. Parish, J. Levinsen, R. S. Christensen, G. M. Bruun, and J. J. Arlt: *Observation of Attractive and Repulsive Polarons in a Bose-Einstein Condensate*, "Phys. Rev. Lett." vol. 117, no. 5, 055302 (2016) (cited on pages 66, 67, 71, 73, 77).

[123]M.-G. Hu, M. J. Van de Graaff, D. Kedar, J. P. Corson, E. A. Cornell, and D. S. Jin: *Bose Polarons in the Strongly Interacting Regime*, "Phys. Rev. Lett." vol. 117, no. 5, 055301 (2016) (cited on pages 66, 71, 77).

[124]Z. Z. Yan, Y. Ni, C. Robens, and M. W. Zwierlein: *Bose polarons near quantum criticality*, "Science" vol. 368, no. 6487, 190–194 (2020) (cited on page 66).

[125]J. Etrych, G. Martirosyan, A. Cao, C. J. Ho, Z. Hadzibabic, and C. Eigen: *Universal Quantum Dynamics of Bose Polarons*, "Phys. Rev. X" vol. 15, no. 2, 021070 (2025) (cited on pages 66, 67, 71, 73, 77).

[126]J. Etrych, S. J. Morris, S. M. Fischer, G. Martirosyan, C. J. Ho, M. Drescher, M. Salmhofer, Z. Hadzibabic, T. Enss, and C. Eigen: *Fate of an impurity strongly interacting with a thermal Bose gas*, Aug. 2025 (cited on pages 66, 79).

[127]A. M. Morgen, S. S. Balling, K. K. Nielsen, T. Pohl, G. M. Bruun, and J. J. Arlt: *Quantum beat spectroscopy of repulsive Bose polarons*, "Phys. Rev. Res." vol. 7, no. 2, L022002 (2025) (cited on pages 67, 71).

[128]J. Levinsen, M. M. Parish, and G. M. Bruun: *Impurity in a Bose-Einstein condensate and the Efimov effect*, "Phys. Rev. Lett." vol. 115, no. 12, 125302 (2015) (cited on page 67).

[129]S. M. Yoshida, S. Endo, J. Levinsen, and M. M. Parish: *Universality of an Impurity in a Bose-Einstein Condensate*, "Phys. Rev. X" vol. 8, no. 1, 011024 (2018) (cited on page 67).

[130]M. Drescher, M. Salmhofer, and T. Enss: *Quench Dynamics of the Ideal Bose Polaron at Zero and Nonzero Temperatures*, "Phys. Rev. A" vol. 103, no. 3, 033317 (2021) (cited on page 67).

[131]M. Drescher, M. Salmhofer, and T. Enss: *Bosonic functional determinant approach and its application to polaron spectra*, "Phys. Rev. A" vol. 110, no. 6, 063303 (2024) (cited on page 67).

[132]A. Schirotzek, C.-H. Wu, A. Sommer, and M. W. Zwierlein: *Observation of Fermi Polarons in a Tunable Fermi Liquid of Ultracold Atoms*, "Phys. Rev. Lett." vol. 102, no. 23, 230402 (2009) (cited on pages 68, 85).

[133]S. Nascimbène, N. Navon, K. J. Jiang, L. Tarruell, M. Teichmann, J. McKeever, F. Chevy, and C. Salomon: *Collective oscillations of an imbalanced Fermi gas: Axial compression modes and polaron effective mass*, "Phys. Rev. Lett." vol. 103, no. 17, 170402 (2009) (cited on pages 68, 78).

[134]N. Darkwah Oppong, L. Riegger, O. Bettermann, M. Höfer, J. Levinsen, M. M. Parish, I. Bloch, and S. Fölling: *Observation of coherent multiorbital polarons in a two-dimensional Fermi gas*, "Phys. Rev. Lett." vol. 122, no. 19, 193604 (2019) (cited on page 68).

[135]Z. Yan, P. B. Patel, B. Mukherjee, R. J. Fletcher, J. Struck, and M. W. Zwierlein: *Boiling a Unitary Fermi Liquid*, "Phys. Rev. Lett." vol. 122, no. 9, 093401 (2019) (cited on pages 68, 78).

[136]H. S. Adlong, W. E. Liu, F. Scazza, M. Zaccanti, N. D. Oppong, S. Fölling, M. M. Parish, and J. Levinsen: *Quasiparticle Lifetime of the Repulsive Fermi Polaron*, "Phys. Rev. Lett." vol. 125, no. 13, 133401 (2020) (cited on page 68).

[137]G. Ness, C. Shkedrov, Y. Florshaim, O. K. Diessel, J. von Milczewski, R. Schmidt, and Y. Sagi: *Observation of a Smooth Polaron-Molecule Transition in a Degenerate Fermi Gas*, "Phys. Rev. X" vol. 10, no. 4, 041019 (2020) (cited on page 68).

[138]I. Fritsche, C. Baroni, E. Dobler, E. Kirilov, B. Huang, R. Grimm, G. M. Bruun, and P. Massignan: *Stability and breakdown of Fermi polarons in a strongly interacting Fermi-Bose mixture*, "Phys. Rev. A" vol. 103, no. 5, 053314 (2021) (cited on pages 68, 69).

[139]F. J. Vivanco, A. Schuckert, S. Huang, G. L. Schumacher, G. G. T. Assumpção, Y. Ji, J. Chen, M. Knap, and N. Navon: *The strongly driven Fermi polaron*, Aug. 2023 (cited on page 68).

[140]C. Kohstall, M. Zaccanti, M. Jag, A. Trenkwalder, P. Massignan, G. M. Bruun, F. Schreck, and R. Grimm: *Metastability and coherence of repulsive polarons in a strongly interacting Fermi mixture*, "Nature" vol. 485, 615–618 (2012) (cited on page 68).

[141]M. Koschorreck, D. Pertot, E. Vogt, B. Fröhlich, M. Feld, and M. Köhl: *Attractive and repulsive Fermi polarons in two dimensions*, "Nature" vol. 485, 619–622 (2012) (cited on pages 68, 78).

[142]Y. Zhang, W. Ong, I. Arakelyan, and J. E. Thomas: *Polaron-to-Polaron Transitions in the Radio-Frequency Spectrum of a Quasi-Two-Dimensional Fermi Gas*, "Phys. Rev. Lett." vol. 108, no. 23, 235302 (2012) (cited on page 68).

[143]A. N. Wenz, G. Zürn, S. Murmann, I. Brouzos, T. Lompe, and S. Jochim: *From Few to Many: Observing the Formation of a Fermi Sea One Atom at a Time*, "Science" vol. 342, no. 6157, 457–460 (2013) (cited on page 68).

[144]M. Cetina, M. Jag, R. S. Lous, J. T. M. Walraven, R. Grimm, R. S. Christensen, and G. M. Bruun: *Decoherence of Impurities in a Fermi Sea of Ultracold Atoms*, "Phys. Rev. Lett." vol. 115, no. 13, 135302 (2015) (cited on page 68).

[145]M. Cetina, M. Jag, R. S. Lous, I. Fritsche, J. T. M. Walraven, R. Grimm, J. Levinsen, M. M. Parish, R. Schmidt, M. Knap, and E. Demler: *Ultrafast many-body interferometry of impurities coupled to a Fermi sea*, "Science" vol. 354, no. 6308, 96–99 (2016) (cited on page 68).

[146]F. Scazza, G. Valtolina, P. Massignan, A. Recati, A. Amico, A. Burchianti, C. Fort, M. Inguscio, M. Zaccanti, and G. Roati: *Repulsive Fermi polarons in a resonant mixture of ultracold ^{6}Li atoms*, "Phys. Rev. Lett." vol. 118, no. 8, 083602 (2017) (cited on pages 68, 78).

[147]P. Massignan, M. Zaccanti, and G. M. Bruun: *Polarons, dressed molecules and itinerant ferromagnetism in ultracold Fermi gases*, "Rep. Prog. Phys." vol. 77, no. 3, 034401 (2014) (cited on page 68).

[148]F. Chevy and C. Mora: *Ultra-cold polarized Fermi gases*, "Rep. Prog. Phys." vol. 73, no. 11, 112401 (2010) (cited on page 68).

[149]P. Massignan, S. Richard, G. E. Astrakharchik, A. İmamoglu, Z. Martin, J. J. Arlt, and G. M. Bruun: *Polarons in atomic gases and two-dimensional semiconductors*, "Rev. Mod. Phys.", 10.1103/4nng-bb9z (2026) (cited on page 68).

[150]C. Baroni, G. Lamporesi, and M. Zaccanti: *Quantum mixtures of ultracold gases of neutral atoms*, "Nat Rev Phys" vol. 6, no. 12, 736–752 (2024) (cited on page 68).

[151]R. Schmidt, M. Knap, D. A. Ivanov, J.-S. You, M. Cetina, and E. Demler: *Universal many-body response of heavy impurities coupled to a Fermi sea: a review of recent progress*, "Rep. Prog. Phys." vol. 81, no. 2, 024401 (2018) (cited on page 68).

[152]L. B. Tan, O. Cotlet, A. Bergschneider, R. Schmidt, P. Back, Y. Shimazaki, M. Kroner, and A. İmamoğlu: *Interacting Polaron-Polaritons*, "Phys. Rev. X" vol. 10, no. 2, 021011 (2020) (cited on page 69).

[153]J. B. Muir, J. Levinsen, S. K. Earl, M. A. Conway, J. H. Cole, M. Wurdack, R. Mishra, D. J. Ing, E. Estrecho, Y. Lu, D. K. Efimkin, J. O. Tollerud, E. A. Ostrovskaya, M. M. Parish, and J. A. Davis: *Interactions between Fermi polarons in monolayer WS2*, "Nat. Commun." vol. 13, no. 1, 6164 (2022) (cited on page 69).

[154]O. I. Kartavtsev and A. V. Malykh: *Low-energy three-body dynamics in binary quantum gases*, "J. Phys. B: At. Mol. Opt. Phys." vol. 40, no. 7, 1429 (2007) (cited on page 69).

[155]F. Grusdt and M. Fleischhauer: *Tunable polarons of slow-light polaritons in a two-dimensional Bose-Einstein condensate*, "Phys. Rev. Lett." vol. 116, no. 5, 053602 (2016) (cited on page 71).

[156]V. Pastukhov: *Polaron in dilute 2D Bose gas at low temperatures*, "J. Phys. B: At. Mol. Opt. Phys." vol. 51, no. 15, 155203 (2018) (cited on page 71).

[157]L. A. Peña Ardila, G. E. Astrakharchik, and S. Giorgini: *Strong coupling Bose polarons in a two-dimensional gas*, "Phys. Rev. Res." vol. 2, no. 2, 023405 (2020) (cited on page 71).

[158]H. Tajima, J. Takahashi, S. I. Mistakidis, E. Nakano, and K. Iida: *Polaron problems in ultracold atoms: Role of a Fermi sea across different spatial dimensions and quantum fluctuations of a Bose medium*, "Atoms" vol. 9, no. 1, 18 (2021) (cited on page 71).

[159]L. F. Cárdenas-Castillo and A. Camacho-Guardian: *Strongly interacting Bose polarons in two-dimensional atomic gases and quantum fluids of polaritons*, "Atoms" vol. 11, no. 1, 3 (2023) (cited on page 71).

[160]Y. Nakano, M. M. Parish, and J. Levinsen: *Variational approach to the two-dimensional Bose polaron*, "Phys. Rev. A" vol. 109, no. 1, 013325 (2024) (cited on page 71).

[161]D. S. Petrov, C. Salomon, and G. V. Shlyapnikov: *Weakly bound dimers of fermionic atoms*, "Phys. Rev. Lett." vol. 93, no. 9, 090404 (2004) (cited on pages 72, 77, 78).

[162]J. Bardeen, G. Baym, and D. Pines: *Effective interaction of ^{3}He atoms in dilute solutions of ^{3}He in ^{4}He at low temperatures*, "Phys. Rev." vol. 156, no. 1, 207–221 (1967) (cited on page 72).

[163]R. Scelle, T. Rentrop, A. Trautmann, T. Schuster, and M. K. Oberthaler: *Motional coherence of fermions immersed in a Bose gas*, "Phys. Rev. Lett." vol. 111, no. 7, 070401 (2013) (cited on page 73).

[164]T. Rentrop, A. Trautmann, F. A. Olivares, F. Jendrzejewski, A. Komnik, and M. K. Oberthaler: *Observation of the phononic Lamb shift with a synthetic vacuum*, "Phys. Rev. X" vol. 6, no. 4, 041041 (2016) (cited on page 73).

[165]M. Schick: *Two-dimensional system of hard-core bosons*, "Phys. Rev. A" vol. 3, no. 3, 1067–1073 (1971) (cited on pages 74, 75).

[166]Z. Hadzibabic and J. Dalibard: *Two-dimensional Bose fluids: An atomic physics perspective*, "Riv. Nuovo Cimento" vol. 34, no. 6, 389–434 (2011) (cited on page 74).

[167]E. P. Bernard and W. Krauth: *Two-step melting in two dimensions: First-order liquid-hexatic transition*, "Phys. Rev. Lett." vol. 107, no. 15, 155704 (2011) (cited on page 75).

[168]F. Scazza, G. Valtolina, A. Amico, P. E. S. Tavares, M. Inguscio, W. Ketterle, G. Roati, and M. Zaccanti: *Exploring emergent heterogeneous phases in strongly repulsive Fermi gases*, "Phys. Rev. A" vol. 101, no. 1, 013603 (2020) (cited on page 77).

[169]D. S. Petrov, C. Salomon, and G. V. Shlyapnikov: *Scattering properties of weakly bound dimers of fermionic atoms*, "Phys. Rev. A" vol. 71, no. 1, 012708 (2005) (cited on page 77).

[170] L. A. P. Ardila and S. Giorgini: *Impurity in a Bose-Einstein condensate: Study of the attractive and repulsive branch using quantum Monte Carlo methods*, "Phys. Rev. A" vol. 92, no. 3, 033612 (2015) (cited on page 77).

[171] R. Schmidt and T. Enss: *Self-stabilized Bose polarons*, "SciPost Phys." vol. 13, no. 3, 054 (2022) (cited on page 77).

[172] D. J. Wineland and W. M. Itano: *Laser cooling of atoms*, "Phys. Rev. A" vol. 20, no. 4, 1521–1540 (1979) (cited on page 78).

[173] D. M. Harber, H. J. Lewandowski, J. M. McGuirk, and E. A. Cornell: *Effect of cold collisions on spin coherence and resonance shifts in a magnetically trapped ultracold gas*, "Phys. Rev. A" vol. 66, no. 5, 053616 (2002) (cited on page 79).

[174] K. B. Gubbels and H. T. C. Stoof: *Imbalanced Fermi gases at unitarity*, "Phys. Rep.", Imbalanced Fermi Gases at Unitarity vol. 525, no. 4, 255–313 (2013) (cited on pages 80, 85, 94).

[175] A. I. Larkin and Y. N. Ovchinnikov: *Inhomogeneous state of superconductors*, "Sov. Phys. JETP" vol. 20, no. 3, 762 (1965) (cited on pages 84, 92).

[176] P. Fulde and R. A. Ferrell: *Superconductivity in a Strong Spin-Exchange Field*, "Phys. Rev." vol. 135, no. 3A, A550–A563 (1964) (cited on pages 84, 92).

[177] G. Sarma: *On the influence of a uniform exchange field acting on the spins of the conduction electrons in a superconductor*, "J. Phys. Chem. Solids" vol. 24, no. 8, 1029–1032 (1963) (cited on pages 84, 93).

[178] H. Müther and A. Sedrakian: *Spontaneous Breaking of Rotational Symmetry in Superconductors*, "Phys. Rev. Lett." vol. 88, no. 25, 252503 (2002) (cited on pages 84, 94).

[179] A. Sedrakian, J. Mur-Petit, A. Polls, and H. Müther: *Pairing in a two-component ultracold Fermi gas: Phases with broken-space symmetries*, "Phys. Rev. A" vol. 72, no. 1, 013613 (2005) (cited on pages 84, 94).

[180] A. Sedrakian, J. Mur-Petit, A. Polls, and H. Müther: *Deformed Fermi surfaces in ultracold Fermi gases*, Apr. 2006 (cited on page 84).

[181] L. P. Gor'Kov: *The critical supercooling field in superconductivity theory*, "Sov. Phys. JETP" vol. 10, 593–599 (1960) (cited on page 84).

[182] R. Beyer and J. Wosnitza: *Emerging evidence for FFLO states in layered organic superconductors (Review Article)*, "Low Temp. Phys." vol. 39, no. 3, 225–231 (2013) (cited on page 84).

[183] J. Wosnitza: *FFLO States in Layered Organic Superconductors*, "Ann. Phys." vol. 530, no. 2, 1700282 (2018) (cited on pages 84, 93).

[184] R. Lortz, Y. Wang, A. Demuer, P. H. M. Böttger, B. Bergk, G. Zwicknagl, Y. Nakazawa, and J. Wosnitza: *Calorimetric Evidence for a Fulde-Ferrell-Larkin-Ovchinnikov Superconducting State in the Layered Organic Superconductor $K-(BEDT\text{-}TTF)_2Cu(NCS)_2$*, "Phys. Rev. Lett." vol. 99, no. 18, 187002 (2007) (cited on page 84).

[185] B. Bergk, A. Demuer, I. Sheikin, Y. Wang, J. Wosnitza, Y. Nakazawa, and R. Lortz: *Magnetic torque evidence for the Fulde-Ferrell-Larkin-Ovchinnikov state in the layered organic superconductor $K-(BEDT\text{-}TTF)_2Cu(NCS)_2$*, "Phys. Rev. B" vol. 83, no. 6, 064506 (2011) (cited on page 84).

[186] H. Mayaffre, S. Krämer, M. Horvatić, C. Berthier, K. Miyagawa, K. Kanoda, and V. F. Mitrović: *Evidence of Andreev bound states as a hallmark of the FFLO phase in κ-$(BEDT\text{-}TTF)_2Cu(NCS)_2$*, "Nature Phys" vol. 10, no. 12, 928–932 (2014) (cited on page 84).

[187] M. W. Zwierlein, A. Schirotzek, C. H. Schunck, and W. Ketterle: *Fermionic Superfluidity with Imbalanced Spin Populations*, "Science" vol. 311, no. 5760, 492–496 (2006) (cited on page 85).

[188]M. W. Zwierlein, C. H. Schunck, A. Schirotzek, and W. Ketterle: *Direct observation of the superfluid phase transition in ultracold Fermi gases*, "Nature" vol. 442, no. 7098, 54–58 (2006) (cited on page 85).

[189]Y. Shin, M. W. Zwierlein, C. H. Schunck, A. Schirotzek, and W. Ketterle: *Observation of Phase Separation in a Strongly Interacting Imbalanced Fermi Gas*, "Phys. Rev. Lett." vol. 97, no. 3, 030401 (2006) (cited on page 85).

[190]Y. Shin, C. H. Schunck, A. Schirotzek, and W. Ketterle: *Tomographic rf Spectroscopy of a Trapped Fermi Gas at Unitarity*, "Phys. Rev. Lett." vol. 99, no. 9, 090403 (2007) (cited on page 85).

[191]C. H. Schunck, Y. Shin, A. Schirotzek, M. W. Zwierlein, and W. Ketterle: *Pairing Without Superfluidity: The Ground State of an Imbalanced Fermi Mixture*, "Science" vol. 316, no. 5826, 867–870 (2007) (cited on page 85).

[192]Y.-i. Shin, A. Schirotzek, C. H. Schunck, and W. Ketterle: *Realization of a Strongly Interacting Bose-Fermi Mixture from a Two-Component Fermi Gas*, "Phys. Rev. Lett." vol. 101, no. 7, 070404 (2008) (cited on page 85).

[193]Y.-i. Shin: *Determination of the equation of state of a polarized Fermi gas at unitarity*, "Phys. Rev. A" vol. 77, no. 4, 041603 (2008) (cited on page 85).

[194]G. B. Partridge, W. Li, R. I. Kamar, Y.-a. Liao, and R. G. Hulet: *Pairing and Phase Separation in a Polarized Fermi Gas*, "Science" vol. 311, no. 5760, 503–505 (2006) (cited on page 85).

[195]G. B. Partridge, W. Li, Y. A. Liao, R. G. Hulet, M. Haque, and H. T. C. Stoof: *Deformation of a Trapped Fermi Gas with Unequal Spin Populations*, "Phys. Rev. Lett." vol. 97, no. 19, 190407 (2006) (cited on page 85).

[196]J. Tempere, S. N. Klimin, and J. T. Devreese: *Effect of population imbalance on the Berezinskii-Kosterlitz-Thouless phase transition in a superfluid Fermi gas*, "Phys. Rev. A" vol. 79, no. 5, 053637 (2009) (cited on pages 86, 88, 90).

[197]J. Tempere, S. N. Klimin, and J. T. Devreese: *The Berezinskii–Kosterlitz–Thouless transition in imbalanced 2D Fermi gases: The role of fluctuations*, "Physica C: Superconductivity", Vortex Matter in Nanostructured Superconductors vol. 470, no. 19, 809–813 (2010) (cited on pages 86, 88, 90, 91, 104).

[198]B. Tüzemen, T. Zawiślak, G. Wlazłowski, and P. Magierski: *Disordered structures in ultracold spin-imbalanced Fermi gas*, "New J. Phys." vol. 25, no. 3, 033013 (2023) (cited on pages 87, 88, 92, 107).

[199]J. Tempere, M. Wouters, and J. T. Devreese: *Imbalanced Fermi superfluid in a one-dimensional optical potential*, "Phys. Rev. B" vol. 75, no. 18, 184526 (2007) (cited on pages 88–90).

[200]L. He and P. Zhuang: *Phase diagram of a cold polarized Fermi gas in two dimensions*, "Phys. Rev. A" vol. 78, no. 3, 033613 (2008) (cited on pages 88–90).

[201]D. E. Sheehy: *Fulde-Ferrell-Larkin-Ovchinnikov state of two-dimensional imbalanced Fermi gases*, "Phys. Rev. A" vol. 92, no. 5, 053631 (2015) (cited on pages 88, 92, 94).

[202]D. S. Petrov, M. A. Baranov, and G. V. Shlyapnikov: *Superfluid transition in quasi-two-dimensional Fermi gases*, "Phys. Rev. A" vol. 67, no. 3, 031601 (2003) (cited on page 90).

[203]V. Ngampruetikorn, M. M. Parish, and J. Levinsen: *Three-body problem in a two-dimensional Fermi gas*, "EPL" vol. 102, no. 1, 13001 (2013) (cited on page 90).

[204]A. Bulgac and M. M. Forbes: *Unitary Fermi Supersolid: The Larkin-Ovchinnikov Phase*, "Phys. Rev. Lett." vol. 101, no. 21, 215301 (2008) (cited on page 92).

[205]S. Yin, J.-P. Martikainen, and P. Törmä: *Fulde-Ferrell states and Berezinskii-Kosterlitz-Thouless phase transition in two-dimensional imbalanced Fermi gases*, "Phys. Rev. B" vol. 89, no. 1, 014507 (2014) (cited on page 93).

[206]P. T. Brown, D. Mitra, E. Guardado-Sanchez, P. Schauß, S. S. Kondov, E. Khatami, T. Paiva, N. Trivedi, D. A. Huse, and W. S. Bakr: *Spin-imbalance in a 2D Fermi-Hubbard system*, "Science" vol. 357, no. 6358, 1385–1388 (2017) (cited on page 96).

[207]E. C. Samson, K. E. Wilson, Z. L. Newman, and B. P. Anderson: *Deterministic creation, pinning, and manipulation of quantized vortices in a Bose-Einstein condensate*, "Phys. Rev. A" vol. 93, no. 2, 023603 (2016) (cited on pages 105, 114).

[208]H. L. Michel: *Vortices in homogenous two-dimensional spin-imbalanced and balanced Fermi gases*, MSc Thesis, Hamburg: Universität Hamburg 2026 (cited on pages 106, 118).

[209]J. J. Kinnunen, J. E. Baarsma, J.-P. Martikainen, and P. Törmä: *The Fulde–Ferrell–Larkin–Ovchinnikov state for ultracold fermions in lattice and harmonic potentials: a review*, "Rep. Prog. Phys." vol. 81, no. 4, 046401 (2018) (cited on pages 108, 115).

[210]W. J. Kwon, G. Del Pace, K. Xhani, L. Galantucci, A. Muzi Falconi, M. Inguscio, F. Scazza, and G. Roati: *Sound emission and annihilations in a programmable quantum vortex collider*, "Nature" vol. 600, no. 7887, 64–69 (2021) (cited on page 114).

[211]M. Takahashi, T. Mizushima, M. Ichioka, and K. Machida: *Vortex-Core Structure in Neutral Fermion Superfluids with Population Imbalance*, "Phys. Rev. Lett." vol. 97, no. 18, 180407 (2006) (cited on page 115).

[212]L. A. Sidorenkov, M. K. Tey, R. Grimm, Y.-H. Hou, L. Pitaevskii, and S. Stringari: *Second sound and the superfluid fraction in a Fermi gas with resonant interactions*, "Nature" vol. 498, no. 7452, 78–81 (2013) (cited on page 115).

[213]D. K. Hoffmann, V. P. Singh, T. Paintner, M. Jäger, W. Limmer, L. Mathey, and J. Hecker Denschlag: *Second sound in the crossover from the Bose-Einstein condensate to the Bardeen-Cooper-Schrieffer superfluid*, "Nat. Commun." vol. 12, no. 1, 7074 (2021) (cited on page 115).

[214]X. Li, X. Luo, S. Wang, K. Xie, X.-P. Liu, H. Hu, Y.-A. Chen, X.-C. Yao, and J.-W. Pan: *Second sound attenuation near quantum criticality*, "Science" vol. 375, no. 6580, 528–533 (2022) (cited on page 115).

[215]T. A. Hilker, L. H. Dogra, C. Eigen, J. A. P. Glidden, R. P. Smith, and Z. Hadzibabic: *First and Second Sound in a Compressible 3D Bose Fluid*, "Phys. Rev. Lett." vol. 128, no. 22, 223601 (2022) (cited on page 115).

[216]Z. Yan, P. B. Patel, B. Mukherjee, C. J. Vale, R. J. Fletcher, and M. W. Zwierlein: *Thermography of the superfluid transition in a strongly interacting Fermi gas*, "Science" vol. 383, no. 6683, 629–633 (2024) (cited on page 115).

[217]P. Christodoulou, M. Gałka, N. Dogra, R. Lopes, J. Schmitt, and Z. Hadzibabic: *Observation of first and second sound in a BKT superfluid*, "Nature" vol. 594, no. 7862, 191–194 (2021) (cited on page 115).

DANKSAGUNG

Zum Abschluss möchte ich mich bei der Vielzahl toller Menschen bedanken, die mich während der Jahre meiner Promotion begleitet haben.

Als Erstes möchte ich mich bei Henning für die exzellente Betreuung und die Möglichkeit, an einem spannenden Experiment zu forschen, bedanken. Von Anfang an habe ich mich sehr wohl in deiner Gruppe gefühlt, da du stets auf ein gesundes Arbeitsklima achtest, nicht nur auf professioneller, sondern auch auf zwischenmenschlicher Ebene. Deine Begeisterung für Physik und deine Fähigkeit, komplexe Sachverhalte in einfachen Worten zu erklären, sind bewundernswert, und ich konnte mich stets mit Fragen an dich wenden.

Des Weiteren möchte ich mich bei meinem Team bedanken, zunächst bei Niclas und Hauke, die mich während einer großen Umbauphase an das Experiment herangeführt haben. Furthermore, I want to thank Cesar, who joined the team shortly after I did. Your unparalleled energy and enthusiasm for physics are infectious, and really pushed the experiment forward.

I also want to thank Artak, Moritz, Leo, Jonas, and all other members of the Lithium team I have shared the lab with over the past years, as well as the entire research group. The pasta Mondays (which were rarely on Mondays), outings at Landgang, and other group activities really brightened my time at the institute.

Zuletzt möchte ich mich bei meiner Familie, meinen Freund:innen, meiner WG und meiner Partnerin bedanken. In den letzten Jahren habt ihr mich stets geerdet und unterstützt, und ich bin dankbar, so wundervolle Menschen in meinem Leben zu haben.

EIDESSTATTLICHE VERSICHERUNG

Hiermit versichere ich an Eides statt, die vorliegende Dissertationsschrift selbst verfasst und keine anderen als die angegebenen Hilfsmittel und Quellen benutzt zu haben.

Sofern im Zuge der Erstellung der vorliegenden Dissertationsschrift generative Künstliche Intelligenz (gKI) basierte elektronische Hilfsmittel verwendet wurden, versichere ich, dass meine eigene Leistung im Vordergrund stand und dass eine vollständige Dokumentation aller verwendeten Hilfsmittel gemäß der Guten wissenschaftlichen Praxis vorliegt. Ich trage die Verantwortung für eventuell durch die gKI generierte fehlerhafte oder verzerrte Inhalte, fehlerhafte Referenzen, Verstöße gegen das Datenschutz- und Urheberrecht oder Plagiate.

Hamburg, den 28.10.2026

Unterschrift der Doktorandin / des Doktoranden